Université de Lille

École Doctorale Sciences Pour l'Ingénieur

THÈSE

Pour obtenir le grade de

Docteur en Science de l'Université de Lille

Spécialité: Électronique, microélectronique, nanoélectronique et micro-ondes

présenté par

Natalia TUREK

Imagerie à haute résolution des assemblages moléculaires par nc-AFM et KPFM à basse température

High resolution nc-AFM and KPFM imaging of molecular assemblies at low temperature

soutenue le 26 novembre 2019

Membres du jury:

Benjamin Grévin	Directeur de Recherche CNRS, Laboratoire SyMMES Grenoble	Rapporteur
Mariusz Zdrojek	Professeur de l'Université de Varsovie, Faculté de Physique	Rapporteur
Laurent Nony	Maître de Conférences, Aix-Marseille Université, IM2NP	Examinateur
Jérôme Lagoute	Chargé de Recherche CNRS, Université Paris Diderot, Laboratoire MPQ	Examinateur
Frank Palmino	Professeur, Université de Franche Comté, FEMTO-ST Montbéliard	Président du jury
Xiaonan Sun	Ingénieur de Recherche CNRS, Université Paris Diderot, Laboratoire ITODYS	Examinateur
Thierry Mélin	Directeur de Recherche CNRS, IEMN Villeneuve-d'Ascq	Directeur de thèse
Sylvie Godey	Ingénieur de Recherche CNRS, IEMN Villeneuve-d'Ascq	Co-encadrant de thèse

Abstract

The progress of non-contact Atomic Force Microscopy (nc-AFM) in the last decade enabled studying the structural and electronic properties of molecules at the submolecular scale. The process of tip functionalization relying in attaching single atoms or molecules to the tip apex demonstrated an enhanced resolution in both STM and AFM images, such that the chemical structures of many different molecules deposited on metallic surfaces have been resolved. However, few studies have been presented on a semiconductor surface so far.

In this work, we study the formation of molecular self-assemblies on the passivated surface of boron doped silicon Si(111)-($\sqrt{3}\times\sqrt{3}$)$R°$30-B by combined STM/nc-AFM with Kelvin Probe Force Microscopy (KPFM). The experiments have been performed on the Joule-Thomson Scanning Probe Microscope (SPECS), working in ultra high vacuum at temperature of 4 K, using a high stiffness sensor (Kolibri, k=540 kN/m, f_0=1 MHz). The investigated molecules are: 1-(4'cyanophenyl)-2,5-bis(decyloxy)-4-(4'-iodophenyl)benzene (CDB-I), which possess two aliphatic chains attached to a triphenyl core ended with two different terminations (either iodine or cyano group) and non-polar 1,4 bis(4'cyanophenyl)-2,5bis(decyloxy)benzene (CDB) molecule, with two identical cyano group terminations.

The first main objective of this work was to verify the sensitivity of the Kolibri sensor in the charge detection. KPFM measurements of boron doped silicon defects are presented, showing different charge states for dangling bond (DB), silicon vacancy and buried boron dopant defects. A positive charge state is found for the DB, in accordance with previous STM studies. The surface potential of this defect constitutes a reference value of a single charge on the surface. The second objective of this thesis was to obtain submolecular resolution in topography and electrical imaging on molecules, without intentional tip functionalization. A submolecular contrast is observed in the frequency shift images of single molecules with identification of the three-phenyl core and details of the aliphatic chains. Moreover, a high resolution is obtained in the surface potential images from KPFM measurements as well. Depending on type of the adsorption of molecule on the surface, two different KPFM contrasts are distinguished. Lastly, the comparison of organization in the assemblies is done for both CDB and CDB-I molecules. A similar organization is found for both molecules in nc-AFM images. The asymmetry of the nc-AFM topography and KPFM map of CDB-I molecules indicates the dipolar organization along a given assembly row.

Résumé

Le progrès important de la microscopie à force atomique sans contact (nc-AFM) au cours de la dernière décennie a permis d'étudier les propriétés structurelles et électroniques des molécules à l'échelle sub-moléculaire. Le processus de fonctionnalisation de la pointe, qui consiste à attacher des atomes ou des molécules uniques à l'apex de la pointe, a démontré une résolution exaltée des images STM et AFM, de sorte que les structures chimiques de nombreuses molécules différentes déposées sur des surfaces métalliques ont été résolues. Cependant, peu d'études ont été présentées jusqu'à présent sur des surfaces de semiconducteurs.

Dans cette thèse, nous étudions la formation d'auto-assemblages moléculaires sur la surface passivée du silicium dopée au bore Si(111)-$(\sqrt{3} \times \sqrt{3})R°$30-B par STM/nc-AFM combiné avec Kelvin Probe Force Microscopy (KPFM). Les expériences ont été réalisées sur un microscope AFM/STM Joule-Thomson (SPECS), travaillant sous ultra-vide à une température de 4 K, en utilisant un capteur de force à haute rigidité (Kolibri, k=540 kN/m, f_0=1 MHz). Les molécules étudiées sont : 1-(4'cyanophényl)-2,5-bis(décyloxy)-2,5-bis(décyloxy)-4-(4'-iodophényl)benzène (CDB-I), qui possèdent deux chaînes aliphatiques fixées à un noyau triphényle avec deux terminaisons différentes (soit iode, soit cyano) et la molécule nonpolaire 1,4 bis(4'cyanophényle)-2,5bis(décyloxy)benzène (CDB), avec deux terminaisons cyano identiques.

Le premier objectif principal de ce travail était de vérifier la sensibilité de la sonde Kolibri dans la détection de charge. Les mesures KPFM portent sur les défauts du substrat dopé au bore, montrant les différents états de charge pour la liaison pendante (DB), la lacune de silicium et le dopant de bore enterré. L'état de charge positif est trouvé pour la DB, conformément aux études antérieures de la STM. Le potentiel de surface du défaut constitue la valeur de référence d'une seule charge sur la surface. Le deuxième objectif de cette thèse était d'obtenir une résolution sub-moléculaire en topographie et en imagerie KPFM sur les molécules, sans fonctionnalisation intentionnelle de la pointe. Un contraste sub-moléculaire est observé dans les images de décalage de fréquence de molécules individuelles, permettant l'identification du noyau triphényle et des détails des chaînes aliphatiques. De plus, la haute résolution est également obtenue dans les images de potentiel de surface des mesures KPFM. Selon le type d'adsorption de la molécule en surface, on distingue deux contrastes KPFM différents. Enfin, la comparaison de l'organisation dans les assemblages est faite pour les molécules CDB et CDB-I. Malgré l'organisation similaire des deux molécules dans les images nc-AFM, une différence de potentiel de surface est observée pour les deux terminaisons de la molécule CDB-I, indiquant l'organisation dipolaire le long des rangées de molécules des auto-assemblages.

Acknowledgements

First of all, I would like to express my sincere gratitude to my supervisor Thierry Mélin for his support, patience and understanding not only research related but also personally, especially during the last year which was not easy for me. Despite all the problems we have encountered during my thesis his optimism kept me motivated and helped me to valorize the work I have done. Secondly, I would like to thank my co-supervisor Sylvie Godey, for her help in the technical part of the work, her availability and all the hours spent together in the lab until late evenings (so many bake-outs!).

Moreover, I am very grateful to the members of my thesis defence committee: Benjamin Grévin, Mariusz Zdrojek, Laurent Nony, Jérôme Lagoute, Frank Palmino and Xiaonan Sun for evaluation of my work and valuable discussion.

My special thanks goes to personnel from the Near-Field platform :Dominique Deresmes and Maxime Berthe who I could always count on and address the technical issues related to this complicated equipment. Thank you Maxime for your patience and many discussions about Si-B and the dangling bond of course! Besides, I would like to thank the engineers from the clean room, especially David Troadec for his preciseness and express preparation of Kolibri tips with FIB and Christophe Boyaval for SEM imaging.

I would also like to thank the group of Frank Palmino from FEMTO-ST in Montbeliard for providing me the molecule samples and hosting me in their laboratory where I could learn about the correct preparation of the samples. Special thanks to Younes Makoudi for his warm welcoming during my stay in Montbeliard and his help on the subject of molecules.

During five years spent in IEMN, starting from my master internship until the end of my thesis, I was fortunate to meet many people who I would like to thank for helping me with my work. Especially I would like to thank Gabriel, Silvio, Khaoula, Dave and Natahali for all the moments spent together in and outside the lab. I am also very thankful to my polish friend Ola for supporting me on the distance and Ewa without whom (and a strange coincidence) I would not have found myself here.

Finally, I would like to thank my family for their understanding and support, mainly during the writing period, which helped me in completing my thesis successfully.

Contents

Motivation

Single atoms manipulation, switching the charge state of molecules or following the chemical reactions on the surface - these are only few tremendous achievements, accomplished by the researchers, thanks to progress of scanning probe microscopy techniques in the recent years [1, 2, 3, 4, 5]. The invention of STM in 1981 by Binnig *et al.* [6] and AFM few years after [7], initiated the revolution in materials characterization, where the single atoms of surfaces could be observed. The non-contact mode of AFM enabled to obtain true atomic resolution using force sensing [8] and imaging nanostructures on the submolecular scale [9]. Thanks to functionalization of tips and development of high stiffness probes, resolving chemical structures of molecules became possible [9]. On the other hand, imaging molecular assemblies remains a great challenge and the origin and contrast formation above the intermolecular bonds is still under discussion [10, 11, 12].

A combined STM with non contact AFM constitutes a complementary technique to study electronic and structural properties of molecular assemblies. In the STM, the topographic image based on local density of states (LDOS) is obtained, which gives the first, coarse information about the organisation of molecules in assemblies. The real topology of the sample is achieved through nc-AFM imaging, where the tip-sample force gradient is the quantity measured within the experiment. Owing to the high advancement of nc-AFM in the last decade, imaging molecules with submolecular resolution became possible due to the tip functionalization with single atoms or molecules [13, 14, 15]. Although the most of studies have been realised with tip terminated with single carbon monoxide (CO) molecule, many different functionalizations led to acquiring enhanced resolution as well, including xenon (Xe) [16, 15], copper oxide (CuO) [17], nitrogenous oxide (NO) [18] or methane (CH_4) [11, 16] collected from metallic surfaces with thin insulating films. Despite the fact that most studies concerning molecules are presented on metallic (or thin film insulated) surfaces, submolecular resolution was also obtained on highly reactive silicon surface, without intentional tip functionalization but only by conditioning the tip on the silicon substrate [19]. Moreover, the increased resolution in STM and nc-AFM images has been shown by attaching a single silicon atom extracted from the passivated surface of boron doped silicon [20], which will constitute the substrate

for molecular assemblies presented in this thesis.

In addition to topography, information about charge distribution can be provided in the spectroscopy method derived from AFM, based on measurement of the frequency shift signal in the function of sample bias, often refereed as Kelvin Probe Force Microscopy (KPFM). Spectroscopy measurements with single charge sensitivity have been presented for gold atoms deposited on NaCl film, using qPlus sensor [13]. Furthermore, it was possible to manipulate the charge state of Au atoms through frequency shift versus voltage spectroscopy, where the single charge events were revealed in the jumps in the frequency shift [21]. The experiments were performed also on molecules, such that the distribution of charge within a single molecule and switching process with reorganization of charge were observed [22]. KPFM experiments together with submolecular resolution in topography ensure the exhaustive information about the orientation and position of molecules in assemblies. As a result, the organization of molecules on the surface and the interaction governing the assembly process can be understood better.

The experiments presented in this thesis have been performed on the Joule-Thomson Scanning Probe Microscope (SPECS), working in ultra high vacuum at low temperature. This instrumentation setup was ordered in 2013 and had been installed in the IEMN and put into operation in 2015, exactly in the beginning of this thesis. The main objectives of this thesis and the work presented here was directly related to the arrival of the new system in the laboratory and the will to test its possibility in the experiments at low temperature. Most importantly, we wanted to verify the sensitivity of the Kolibri sensor in both high resolution AFM imaging and charge detection in the KPFM measurements.

In the work presented in this thesis combined nc-AFM and STM have been performed together with KPFM measurements to study organisation of molecular assemblies on passivated surface of boron doped silicon. The first main objective of this work was to verify the sensitivity of Kolibri probe in the charge detection. In the Chapter **2**, KPFM measurements on Si:B defects are presented, showing different charge states for dangling bond (DB), silicon vacancy and buried boron dopant defect. Surface potential distribution obtained within the measurements presented in this Chapter, serve not only for calibration of Kolibri tip, but also for facilitating the analysis and interpretation of KPFM of molecules presented in the subsequent part of the manuscript. The second objective of this thesis was to obtain submolecular resolution on assemblies without intentional tip functionalization. The experiments start with a single molecule study presented in the Chapter **3**, for both CDB and CDB-I molecules. Submolecular contrast is revealed in the constant height frequency shift images and compared to the structural model. In KPFM measurement the submolecular features including three-phenyl core, aliphatic chains and oxygen atoms are distinguished as well. The comparison of organisation of CDB-I and

CDB molecules in assemblies is done in the Chapter **4**. For both molecules frequency shift images are analysed in order to find their orientation in assemblies and anticipate the interactions between molecules and silicon substrate. The asymmetry between both terminations is observed only for CDB-I molecule and then studied with KPFM in order to confirm the formation of dipolar assemblies.

Chapter 1

Introduction

The first chapter opens with brief historical outline and the description of main scanning probe microscopy techniques. In the first part of the chapter the theoretical model of tip-sample system with harmonic oscillator is described together with most important parameters of combined STM/nc-AFM measurement. Sections **1.6** and **1.7** give an introduction to imaging molecules with submolecular resolution using high stiffness probes. The limitation of sensitivity in low temperature measurements is done in the section **1.8**. The second part of the chapter is dedicated to experimental details and procedures used in measurements. The preparation of samples and spectroscopy methods are described in the last sections.

1.1 Principle of Scanning Probe Microscopy

Scanning probe microscopy (SPM) is a family of techniques which allows the investigation of surfaces down to the atomic scale. Their operation principle relies on monitoring the interaction between the probe and the sample while scanning its surface line by line. Thanks to SPM it is possible to study not only the topography but also many different properties of the surface, including magnetic, electrostatic or mechanical properties. Moreover, in the recent years a tremendous work was done in the field of manipulation of nanostructures and even single atoms by the means of scanning probe techniques. SPM techniques are versatile, and applicable not only in physics but also chemistry, biology and medical sciences. Compared to other microscopy techniques such as optical microscopy, the resolution of SPM images is not limited by the diffraction of light, but by the sharpness of the probe used, allowing imaging on the atomic or submolecular scale.

The most important part of SPM is a tiny, sharp probe which collects the information in every scanning point and allows creating an image of the surface. The control of the probe movement in three directions is done with piezoelectric elements which provide

subatomic positioning. Two main techniques belonging to SPM family are: Scanning Tunnelling Microscopy (STM), in which the tunnelling current between a metallic tip and a conductive surface is measured, and Atomic Force Microscopy (AFM), which is based on detecting force changes between the tip and the sample.

1.1.1 Scanning Tunnelling Microscopy

STM was the first SPM technique discovered by Gerd Binnig and Heinrich Rohrer in 1981 at IBM Zurich [6]. This technique uses the quantum phenomenon of current tunnelling occurring between two conductive materials in the very close proximity. In the measurement a bias V is applied between the tip and the sample and the tip is approached to the surface at a nanometric distance, which causes the tunnelling of electrons through the tip-sample gap. The relation between the value of the current and the tip-sample distance z has an exponential dependence with an attenuation factor κ in the $\mathring{A}^{-1}$ range. This leads to a high sensitivity of this technique on the topography changes of the sample:

$$I \propto e^{-2\kappa z} \tag{1.1}$$

where, in a simple model :

$$\kappa = \sqrt{\frac{2m}{\hbar^2}(\frac{\Phi_{tip} + \Phi_{sample}}{2} - \frac{eV}{2})} \tag{1.2}$$

with Φ_{tip}, Φ_{sample} being the work functions of the tip and the sample, respectively. STM measurements can be done in two different ways :

- in the constant height mode, where the scanning is done parallel to the surface plane and the detected signal is the tunnelling current (no z feedback is used),

- in the constant current mode in which a feedback loop keeps a constant value for tunnelling current during scanning, while adapting the tip-substrate distance z.

Due to the use of the feedback loop and smaller risk of tip accident the second mode is used in the most cases for topography imaging. STM images obtained in the constant current mode represent the changes in the sample topography and the electronic density of states of the surface. With regard to the principle of STM, the investigated materials are however limited to metals and semiconductors. It is however also possible to study thin (tunnelling) layers of insulators on metallic substrates.

1.1.2 Atomic Force Microscopy

Following the success of STM, Atomic Force Microscopy was invented in 1986 by Gerd Binnig, Calvin Quate and Christoph Gerber [7]. Compared to STM, the detected signal in the AFM technique is not related to the tunnelling current but to changes in forces between the tip and the sample. Therefore, the big advantage of AFM over STM is its application to both conductive and insulating materials. It is also possible to conduct measurements in a liquid environment, which is crucial for biological studies. Depending on the material and mode used, different types of forces can be detected *e.g.* electrostatic, van der Waals, chemical, magnetic or capillary forces. As a result, different imaging modes are derived from classic AFM, where the topography is obtained, including:

- Electrostatic Force Microscopy (EFM) - used to obtain electrostatic properties of the sample, for example the distribution of charges;
- Kelvin Probe Force Microscopy (KPFM) - measuring the surface potential;
- Magnetic Force Microscopy (MFM) - similar to EFM but magnetic interactions are measured instead;
- Scanning Near Field Optical Microscopy (SNOM) - in which an optical probe scans the surface at the distance of a fraction of the light wavelength;
- Scanning Ion Conductance Microscopy (SICM) - used mostly for ion transport in biological systems, in this technique the tip is used as an electrode.

In AFM, the tip is collecting the information about the sample in each scanning point through either changes in the probe deflection (static mode), or through the frequency or oscillation amplitude changes (dynamic mode). As in STM, a feedback loop is introduced, which keeps the interaction setpoint value constant, by regulating the distance between the tip and the sample. Three different modes in which AFM can be distinguished: contact, tapping and non-contact mode. In the first one the tip is all the time in contact with the surface and the force changes cause the deflection of the sensor. In the tapping mode the tip is oscillated at a fixed frequency near its resonance frequency, and is periodically touching the surface at the end of each cycle while the tip-surface interaction is probed via the reduction in the tip oscillation amplitude. Finally, in the non-contact AFM the tip is kept oscillating close to the resonance frequency f_0, and the tip-substrate interaction is monitored via the change in the probe oscillation frequency due to the surface force field. Most common AFMs detect the probe deflection or vibration properties via optical deflection systems (beam deflection or interferometry). More recently the use of piezo-electric quartz sensors (with electrical signal readout) became popular since it enables to

operate AFMs at low temperature without introducing the heat dissipation associated with optical readout.

1.2 Frequency modulation nc-AFM

In Frequency-Modulation AFM (FM-AFM) mode, the tip is driven with constant amplitude, however the changes in tip-sample interactions cause the shift in frequency $\Delta f = f - f_0$. The feedback loop uses this signal to decrease/increase the tip-sample distance and keep the shift Δf at a desired setpoint value. In ultra high vacuum environment, FM-AFM mode is preferable due to the possibility of higher scan speeds compared to Amplitude-Modulation (AM-AFM) mode [23] . The scheme of the nc-AFM system in FM mode is presented in the Figure **1.1**. In the system three feedback loops must be used: two loops in order to keep the tip oscillation amplitude and phase constant, and a third one to ensure a constant Δf by regulating the tip-sample distance. The phase locked loop (PLL) uses amplitude and phase of detected signal to obtain the frequency f and frequency shift $\Delta f = f - f_0$. The amplitude is then used by the feedback, which compares it with driving amplitude and determines the right excitation voltage to keep it constant. In this loop the information about the dissipation between the tip and the surface is obtained as well. In the third loop, the frequency shift is compared to the setpoint value and then used by Z-controller in order to adjust tip-sample distance.

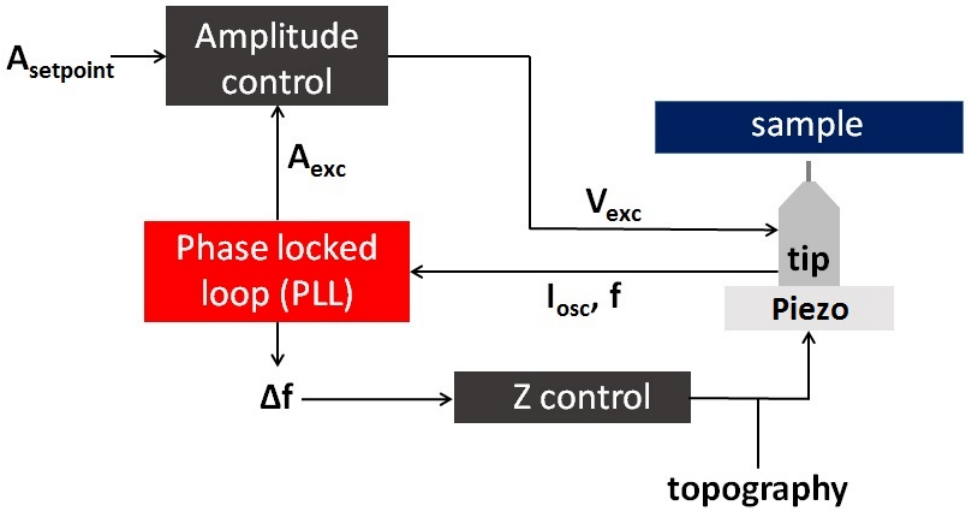

Figure 1.1: Scheme of different feedback loops in nc-AFM measurement with frequency modulation mode.

1.3 Harmonic oscillator

The motion of force sensor can be simplified with a model of a harmonic oscillator with mass m and stiffness k, driven by an external, sinusoidal force. Without tip-sample interaction, the motion equation is given by [24]:

$$m\frac{d^2z}{dt^2} + \gamma\frac{dz}{dt} + kz = F_0\cos(\omega_0 t) \tag{1.3}$$

where $\omega_0 = 2\pi f_0 = \sqrt{\frac{k}{m}}$ is the resonance angular frequency of the sensor, Q is the quality factor, $\gamma = m\frac{\omega}{Q}$ a damping coefficient, F_0, ω are the magnitude and the angular frequency of the driving force respectively. The solution of the differential equation describes the vertical position of the tip $z(t) = A_0\cos(\omega t + \varphi)$, in which the amplitude and phase shift between oscillation and excitation can be written as follows:

$$A_0(\omega) = \frac{F_0/m}{\sqrt{(\omega_0^2 - \omega^2)^2 + \frac{\omega_0^2\omega^2}{Q^2}}} \tag{1.4}$$

$$\tan\varphi = \frac{\omega_0\omega}{Q(\omega_0^2 - \omega^2)} \tag{1.5}$$

Upon interaction between the tip and the sample an additional, distance dependent force F_{ts}, must be taken into account on the right side in the Equation **1.3**. The force leads to an effective modification of the spring constant of the cantilever (here, written in the limit of small oscillation amplitudes) :

$$k' = k - k_{ts} = k - \frac{\partial F_{ts}}{\partial z} \tag{1.6}$$

such that the new frequency of the cantilever becomes:

$$f = \frac{1}{2\pi}\sqrt{\frac{k - \frac{\partial F_{ts}(z)}{\partial z}}{m}} \tag{1.7}$$

Assuming a weak interaction, where the force gradient is much smaller than the spring constant of the cantilever $k_{ts} \ll k$, the frequency and the frequency shift can be written as:

$$f = f_0\sqrt{1 - \frac{k_{ts}}{k}} \approx f_0(1 - \frac{1}{2}\frac{k_{ts}}{k}) \tag{1.8}$$

$$\Delta f = \frac{-f_0}{2k}\frac{\partial F_{ts}(z)}{\partial z} \tag{1.9}$$

The illustration of the frequency curve for attractive and repulsive interactions is presented in Figure **1.2**. The frequency shift is a direct observable in non-contact AFM which gives

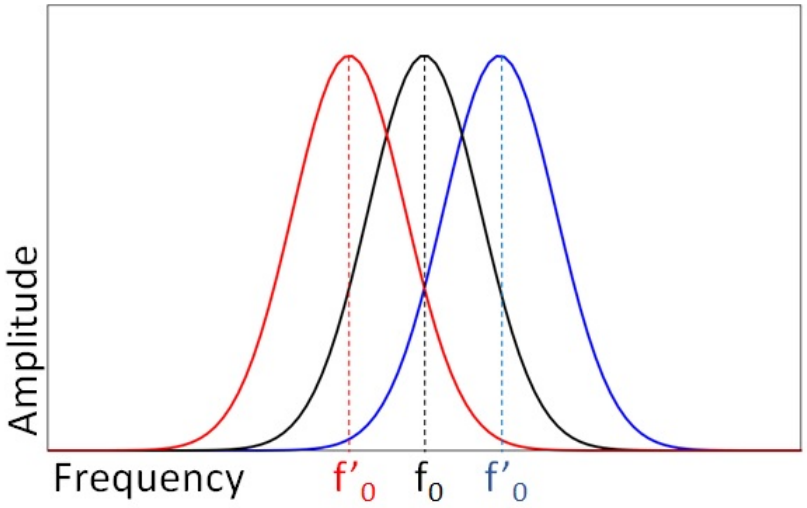

Figure 1.2: Amplitude versus frequency curves for different type of interaction, the curve is shifted positively relative to f_0 for repulsive forces and negatively for attractive forces.

information about the tip-sample interaction. However, the proportionality between the force gradient and frequency shift is valid only for small amplitudes, where the force gradient is assumed to stay constant during whole oscillation cycle. A more general expression between the frequency shift and the force can be obtained by using perturbation theory, treating the interaction between the tip and the sample as a harmonic potential perturbation [25, 26]:

$$\Delta f = \frac{-f_0}{kA_{osc}^2}\langle F_{ts} z\rangle \tag{1.10}$$

where the average $\langle F_{ts} z\rangle$ must be taken over full oscillation cycle of the cantilever. In the first order approximation, the relation for frequency shift, applicable to either small or large amplitudes can be described as follows [27]:

$$\Delta f = \frac{-f_0^2}{kA_{osc}} \int_0^{1/f_0} F_{ts}(z_0 + A_{osc}[1+\cos(2\pi f_0 t)])\cos(2\pi f_0 t)\mathrm{dt} \tag{1.11}$$

$$\Delta f = \frac{-f_0^2}{kA_{osc}} \int_{-1}^{1} F_{ts}(z_0 + A_{osc}[1+u])\frac{u}{\sqrt{1-u^2}}\mathrm{du} \tag{1.12}$$

where z_0 is the minimal tip-sample distance and the last term under the integral is a kernel function, providing utility of equation to both large and small amplitudes. This function has two singularities in the turning points $u = \pm 1$ where the velocity of the tip reaches zero. For small amplitudes it cancels long distance force contribution which varies weakly during oscillation cycle, whereas for big amplitudes it guarantees that the

moment of closest approach to sample has the biggest contribution to measured value of the frequency [26]. The method derived from AFM called force spectroscopy, relies on measuring Δf versus tip-sample distance, from which the force can be obtained. The inversion of equation **1.12** is necessary to obtain the value of the force from the measured value of the frequency shift in the experiment, nonetheless it is not a trivial task. So far, many techniques were suggested by Durig [26], Giessibl [27], Sader and Gotsmann [28]. The method proposed by Sader [28] can be implemented with basic computational programming but it requires analysing the tip-sample distance until free oscillation region. In contrast, Giessibl's procedure [27] needs more complicated mathematical algorithms but will give more accurate results when free oscillation region is not possible to explore.

1.4 Combined STM/nc-AFM

When using a conductive tip, coincident STM and nc-AFM measurements are possible, i.e. tunnelling current can be detected at the same time as frequency shift signal. Because of the oscillation of the tip, the value of the tunnelling current changes periodically. The average value of the current can be described by [29]:

$$\langle I_t(z, A_{osc})\rangle \approx \frac{I_t(z,0)}{\sqrt{4\pi\kappa A_{osc}}} \tag{1.13}$$

where $\kappa = \sqrt{2m\Phi}/\hbar$, with $\Phi = (\Phi_{tip} + \Phi_{sample})/2$. From the above equation we can see, that the mean value of the tunnelling current is smaller if the tip is oscillating during the measurement. Therefore, when working with I_t regulation, the tip must be approached closer to the surface (compared to non-oscillating tip) in order to keep the same value the tunnelling current.

To characterize the combined STM/nc-AFM measurement, a few parameters are needed:

- spring constant k: for typical rectangular cantilevers the value can be calculated from the dimensions and Young modulus of the material. For stiff probes like Kolibri or qPlus it can be determined from thermal noise experiment [30]; the spring constant for Kolibri, given by the SPECS is 540 kN/m [31], however it must be taken into account that Kolibri is made of two coupled oscillators and the effective stiffness is two times bigger, that is k=1080 kN/m;

- resonance frequency f_0: it can be found from the maximum peak of amplitude versus frequency. The value for Kolibri sensors is ≈ 1 MHz;

- quality factor Q: it is defined by the ratio of the energy stored in the resonator E to the energy dissipated per cycle ΔE_{CL} :

$$Q = 2\pi \frac{E}{\Delta E_{CL}} \tag{1.14}$$

  The quality factor can be also determined from the amplitude versus frequency curve by dividing f_0 by the resonance width (FWHM). For Kolibri sensors the value of Q in ultra-high vacuum can reach 100 000 at low temperatures.

- oscillation amplitude A_{osc}: for silicon cantilevers it is necessary to use large amplitudes (on the order of tens of nanometers) to prevent jump-to-contact, due to the small spring constant which limits the restoring force at the closest distance with the surface. The problem is overcome with high stiffness probes; for Kolibri operating amplitudes vary from 20 to 200 pm. The oscillation amplitude specified in the experiments presented in this manuscript is the half of peak-to-peak amplitude ($\mathrm{A}_{osc}=\frac{1}{2}\mathrm{A}_{pp}$).

- bias voltage between tip and the sample V_{bias}: similarly to STM in nc-AFM it is also possible to apply a bias, often the value of the bias is chosen to be close to contact potential difference voltage V_{CPD}, in order to minimize the electrostatic force.

- frequency shift of the sensor Δf: is used as a setpoint for AFM imaging with Δf regulation, however in high resolution imaging of molecules imaging is done with the z feedback loop open and detected signal is frequency shift of the probe.

The first three parameters (k, f_0, Q) are specified by the choice of the sensor, the other parameters can be freely tuned up during each experiment.

1.5 Force contributions

In AFM, different types of forces between the tip and the sample contribute to the total force measured in the experiment. They can be divided into attractive (with negative sign), and repulsive (with positive sign) interactions. The total force detected by the sensor is a combination of these interactions, although by varying tip-sample distance it can be controlled which contribution is dominating. In ultra-high vacuum environment, the total force consists of electrostatic interactions F_{el} (both long and short range), long range van der Waals forces F_{vdW} and short range forces F_{SR} including chemical and Pauli repulsion forces:

$$F_{tot} = F_{el} + F_{vdW} + F_{SR} \tag{1.15}$$

Long range forces that reach tens of nanometers from the surface are dominated by the macroscopic size and shape of the tip. In contrast, short range forces (distances smaller than nanometer) show a stronger decrease with the distance and only few atoms at the tip apex play the biggest role in the interaction, as presented in the Figure **1.3**. Other types of forces like magnetic forces or capillary forces will not be considered here.

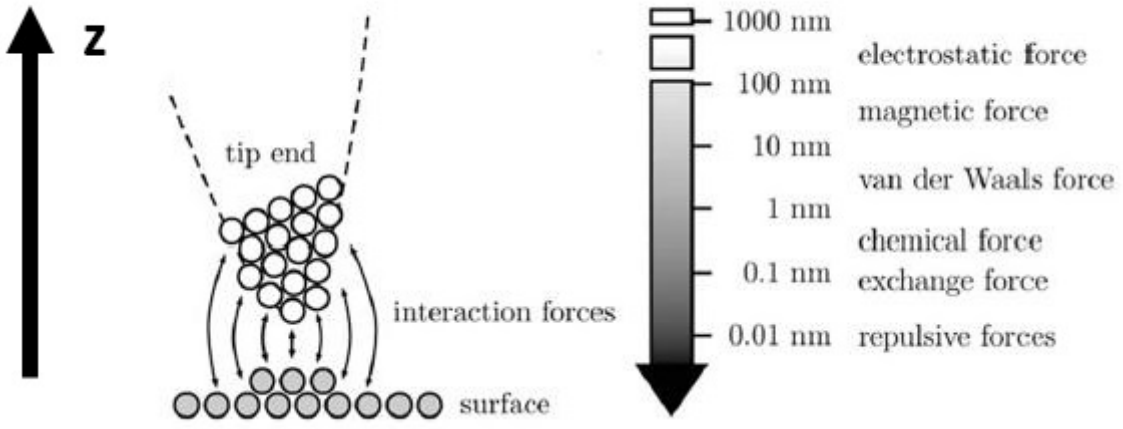

Figure 1.3: Illustration of different interaction forces measured in AFM in function of tip-sample distance [32].

Depending on the type of AFM mode, it is possible to work in different force regimes. The contact mode is performed in the repulsive regime, while non-contact measurements can be done in both repulsive and attractive regimes. Because of the fact that short range interactions have the biggest influence in creating atomic contrast in non-contact AFM, it is crucial to increase the sensitivity in detecting these forces. This can be done by scanning very close to the surface and by using small oscillation amplitudes. To overcome the problem of jump-to-contact with the sample, high stiffness cantilevers must be used, like length extensional resonators (LER) or tuning fork sensors.

1.5.1 Electrostatic forces

Long-range electrostatic interactions can be modelled by the charged capacitor, where the difference between the work functions of the tip and the sample lead to the formation of an internal electric field in the capacitance at equilibrium. By assuming the model of a plane capacitor, the force acting on the tip can be written as:

$$F_{el} = \frac{1}{2}\frac{\partial C(z)}{\partial z}(V_{bias} - V_{CPD})^2 \tag{1.16}$$

where $C(z)$ is a z dependent capacitance, V_{bias} is a voltage applied between the sample and the tip and V_{CPD} is the contact potential difference. Because the term $\partial C/\partial z$ is negative (the capacitance decreases with increasing z distance), F_{el} is negative: electrostatic capacitive forces are always attractive. F_{el} can be minimized by applying a bias that equals the contact potential difference [33], as done in Kelvin Probe Force Microscopy (KPFM).

While CPD values measured in KPFM at large tip-sample distances correspond well to the expected values, at smaller distances (less than 1 nm) a significant discrepancy is observed [34, 35] and CPD values become in particular distance-dependent. It has been shown, that for small tip-sample separations it is possible to obtain atomic resolution in KPFM images, however the origin of this resolution has been debated [36]. Previously, the atomic distribution of CPD was associated with imaging of the electrostatic force distribution [37] or the local electron density [38] depending on the type of the investigated surface. The concept of the local contact potential difference (LCPD) was initially presented by Wandelt, which is based on the short-range variation of the surface potential [39]. In recent works, the influence of the short-range electrostatic force on the atomic-resolved KPFM images was studied in the case of ionic surfaces and analytic models based of the Madelung potential appearing at the surface have been successfully developed for such surfaces [40, 41, 42].

1.5.2 Van der Waals forces

Van der Waals interactions are long-range forces that stem from dipole moment fluctuations and are always present during measurements. These forces are due to Coulomb attraction between electrically neutral particles where dipole moments or moment fluctuations can take place. These particles can be permanent dipoles, induced dipoles and nonpolar atoms. According to this division, different types of interactions can be specified [43]:

- Keesom force - between permanent dipoles
- Debye force - between permanent and induced dipole
- London force - between nonpolar particles

The total van der Waals force between two atoms is a sum of these three contributions where each scales with $1/r^7$, where r is the distance between two atoms. For macroscopic bodies, the force can be calculated using Hamaker approximation which assumes, that the interaction is additive and non-retarded [44]. The net interaction energy is obtained by integrating the interaction of the atoms of the first object with atoms of the second one,

over their volume. Following this procedure the interaction energy for different geometries can be derived analytically. If the tip apex is modelled as a sphere interacting with plane sample surface, the force can be written as :

$$F(z) = -\frac{AR}{6z^2} \tag{1.17}$$

where R is a sphere radius and z is the tip-sample distance. The interaction constant A, called Hamaker constant depends on the type of material of the tip and the sample and is defined as:

$$A = \pi^2 C n_1 n_2 \tag{1.18}$$

where C is an interaction strength and $n_{1,2}$ represents densities of atoms in the first and the second object respectively. Typical values of Hamaker constant are of the order of 10^{-19} J [44].

1.5.3 Chemical forces

Chemical forces are short range interactions that have their origin in the overlap of the electron wave functions and the repulsion of the ion cores of the tip and sample atoms [45]. For this reason, the acting range of these forces is of the order of angstroms. Chemical forces can be both attractive and repulsive. The attractive force occurs when the overlap of the wavefunction reduces the total energy and can be compared to the binding of the atoms in the molecule [44]. On the other hand, the repulsive force is due to the overlap of electron wavefunction of the atoms that stems from Pauli exclusion principle. To describe the chemical interaction different models can be used, including Morse or Lennard-Jones potential model. In the latter, the potential between pair of atoms can be written as:

$$V_{LJ}(z) = -4E_{bond}[(\frac{\sigma}{z})^{12} - (\frac{\sigma}{z})^{6}] \tag{1.19}$$

where E_{bond} is a bonding energy and σ is the distance between two atoms for equilibrium state. For the tip and the sample setup, the interaction between many atoms must be taken into account as well as their displacement upon the force which will cause modification of the above potential.

Figure **1.4** shows a Δf(z) curve done on the silicon substrate with oscillation amplitude of 50 pm (peak to peak amplitude A_{pp}=100 pm). The measurement of frequency shift signal in the function of Z position, where the long range electrostatic force was compensated by applying V_{bias} equalling the surface potential. The values of Δf signal are in the range of hundreds of millihertz and the absolute value of shift is smaller than 1 Hz, the minimum of Δf(z) is here $\approx$ -550 mHz. In the graph it can be seen, that detection

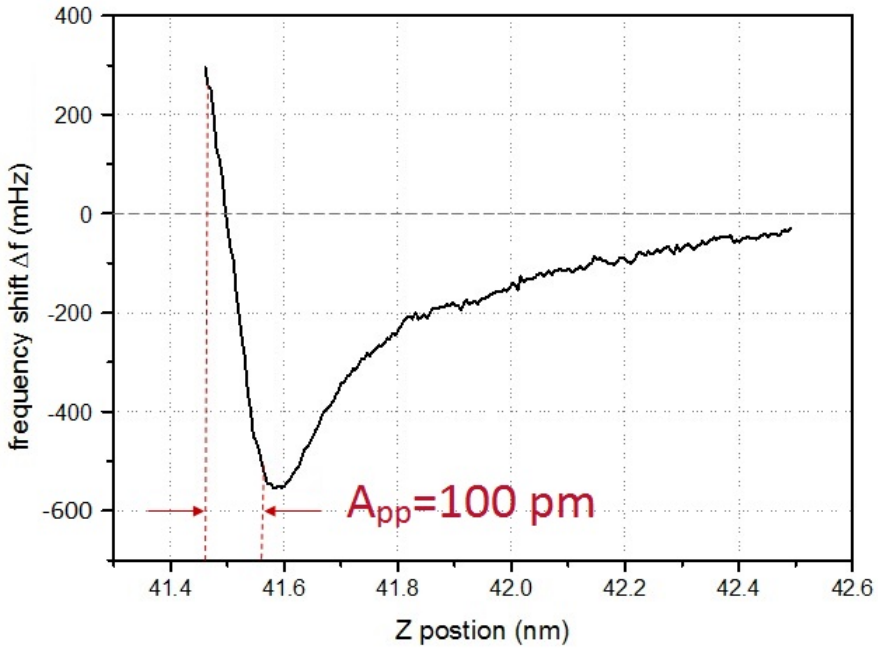

Figure 1.4: Experimental Δf(z) curve on the silicon substrate with V_{bias}=150 mV and A_{osc}=50 pm (peak to peak amplitude A_{pp}=100 pm). On the graph the oscillation amplitude is indicated, showing the range of Δf detected during imaging.

of short range repulsive forces requires working with small oscillation amplitude where the measured Δf signal during imaging is on the negative slope of the curve.

1.6 Imaging molecules

The most important factor in imaging molecules in nc-AFM is the tip termination. While macroscopic properties of the tip including material or crystallographic orientation matter, it is the tip apex which has the biggest contribution in contrast formation at the atomic scale. The following tip characteristics affect the contrast obtained on molecules and can also be decisive in achieving submolecular resolution:

- Size: a small size of tip apex increases lateral resolution, tip decoration with single atoms or molecules (CO, Xe, Br) is preferable in imaging molecules; this process called functionalization is known to be the best method in obtaining submolecular contrast[15, 16].

- Reactivity: to obtain high resolution, one needs to operate in repulsive force regime

[9], which in turn requires approaching the tip very close to the surface. At these distances an inert tip would be needed to prevent displacing or modifying the molecule.

- Dipole: the charge distribution in the tip apex must be taken into account owing to the electrostatic force acting between the tip and the molecule, scanning with charged apex will cause distortion in AFM images due to the repulsion/attraction of the tip with charged zones of the molecules [14].

- Relaxation: at close tip-sample distances the forces can lead to relaxation of the tip apex which then result in artefacts and asymmetric contrast in images, often observed for flexible CO functionalized tips. It was shown that flexibility of the probe particle is essential in imaging sharp contrast between the molecules, possibly caused by close proximity of the atoms [11, 46].

In the most of studies concerning imaging molecules, tip functionalization is performed. This process, relying in attaching molecules or atoms to the end of the tip can be executed in two ways: either in STM regulation through ion field emission when applying voltage pulses (due to the electric field between the tip and the sample) or by mechanical contact between the tip and the sample that leads to bond creation and extraction atom from the surface. Regarding the tip termination different atoms/molecules are used:

- metal atoms : Au, Ag or noble gas atoms that are deposited on metallic surface (Cu, Au) or insulating NaCl film on metallic surface (for example NaCl/Cu(111)) [9, 15]

- semiconductor atoms Si, Sn, Ge [20, 47] extracted from the surface

- diatomic molecules CO, NO [15, 18], CuO [17] also deposited on metallic or insulating surfaces

- functionalization using large molecules already present on the investigated surface C_{60} [48], CH_4 [16], pentacene [9], NTCDI [19]

An example of tip functionalization with Xenon on NaCl/Cu(111) surface is presented in Figure **1.5** together with the comparison of molecule images with submolecular resolution obtained in constant height AFM for CO and Xe tips[15]. In this procedure, scanning is done parallel to the surface plane with z regulation loop turned off while measuring the frequency shift of the sensor. The tip-sample distance is decreased gradually until a high resolution image is achieved, without causing unstable imaging.

In order to understand which force regime needs to be probed to obtain submolecular resolution on molecules, different force contributions were plotted as a function of tip-sample distance (Figure **1.6a**). In this graph we can see that while being far away from

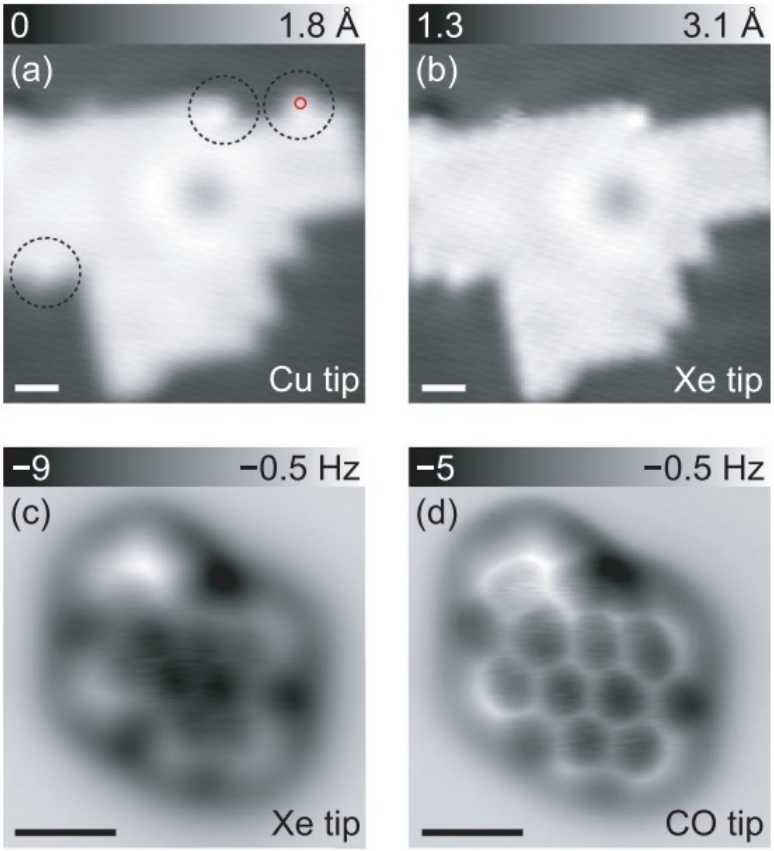

Figure 1.5: Tip functionalization with xenon atoms adsorbed at the edge of NaCl island on Cu(111), a) before and b) after picking up Xe atom on Cu tip, scanning parameters I=2 pA, V=0.2 V. c), d) constant height AFM images of DBNP molecule on Cu(111) recorded with Xe and CO tips. Adapted from [15].

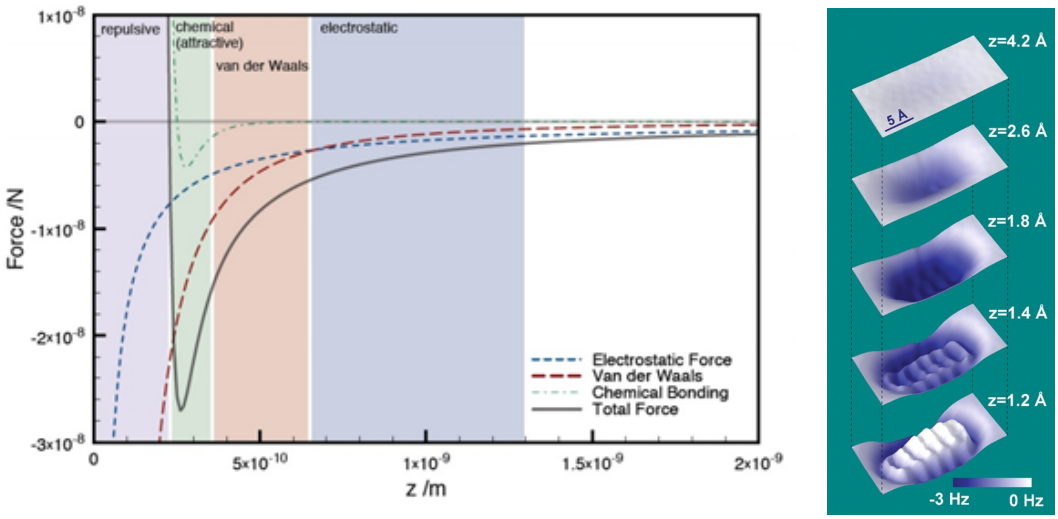

(a) (b)

Figure 1.6: a) Different force contribution detected in AFM plotted in tip-sample distance, extracted from [49] b) Maps of frequency shift above the pentacene molecule for different tip-sample separation [9]

the surface, the electrostatic and van der Waals forces contribute mostly to the detected signal; this situation corresponds to images presented in Figure **1.6b** [9], of negative Δf over the molecule and poor resolution. Approaching the tip closer to the surface results in detecting repulsive short range interactions; this in turn corresponds to images Figure **1.6b**, where the frequency shift becomes more positive (with respect to the substrate, for z=1.4 $\mathring{A}$) and submolecular resolution is achieved. In the AFM images with molecular bonds resolved, often overall interaction is still attractive, however the contribution from repulsive force is significant, such that high resolution is obtained.

1.7 LER sensor

One of the biggest drawback of silicon cantilevers is the necessity of using large amplitudes due to the jump-to-contact issue [50]. Therefore, the capability in detecting short range forces is limited, as the cantilever spends only a small fraction of the oscillation cycle in the lower turning point of the oscillation cycle. Additionally, combined STM/nc-AFM is not trivial due to the limited conductivity of silicon cantilevers. These problems can be overcome by using stiff probes, one example of such probes being Kolibri (SPECS). This piezoelectric quartz sensor based on length extensional resonator (LER) allows for simultaneous AFM measurements with detecting tunnelling current. It consists of an oscillating quartz rod with a small metallic (tungsten) tip attached to its end. The central part of the rod is supported by two side frames with gold coated electrodes at their ends. All the components are enclosed in a metallic cover used as a sputter shield. The spring constant of the sensor is 1080 kN/m and the resonant frequency 1 MHz [31]. The oscillation of the rod is caused by the piezoelectric effect: the sinusoidal bias U_{exc}

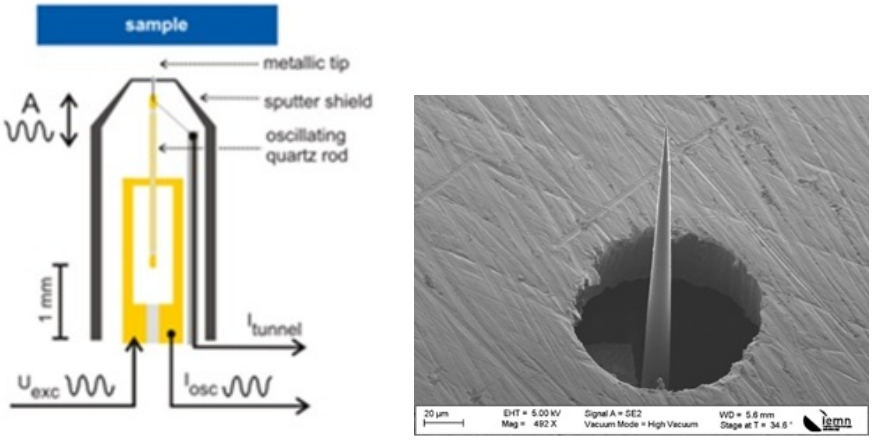

(a) (b)

Figure 1.7: a) Schematics of Kolibri sensor from [31], b) SEM image of Kolibri tip

is applied on one side electrode, which leads to periodic contraction and extension of the quartz material and therefore oscillation of the tip. Furthermore, due to the piezoelectric effect, charges are induced on the surface of the rod and are collected as a current I_{osc} on the opposite side electrode. This ac current enables monitoring the tip oscillation. The conductive tip is isolated from the quartz resonator, which results in a separated readout of the tunnelling current I_t from the oscillation current I_{osc}. The scheme of the probe with their elements is depicted in the Figure **1.7**. What is worth pointing out, is the fact that Kolibri is a purely electrical probe and it does not require any optical readout, as compared to typical silicon cantilevers. Due to the high stiffness of Kolibri it is possible to use small oscillation amplitudes (0.02-2 nm) and to approach the tip very close to the sample surface, which causes increased capability in detecting short range interactions.

1.8 Noise sources

In nc-AFM measurements there are several noise sources that limit the sensitivity. The most important noise contributions are [51]:

- thermal noise
- instrumental detection system noise
- frequency drifts caused by temperature changes

Thermal noise

Even without mechanical oscillation of the tip, the sensitivity is limited by the thermal excitation of the sensor. The fluctuations in sensor deflection can be converted into frequency noise, given by the formula [23]:

$$\frac{\delta f_{thermal}}{f_0} = \sqrt{\frac{k_B T B}{\pi k A_{osc}^2 f_0 Q}} \tag{1.20}$$

where k_B is a Boltzman constant and B is the measurement bandwidth. Using the relationship between the force gradient and the frequency shift $k_{ts} = 2k \cdot \Delta f / f_0$, this noise can be expressed as a force gradient noise as:

$$\Delta k_{thermal} = \sqrt{\frac{4 k k_B T B}{\pi A_{osc}^2 f_0 Q}} \tag{1.21}$$

For Kolibri sensor quality factor Q in ultra high vacuum is around 50000 at room temperature and 100000 at 4 K, for qPlus sensor Q is 5000 at room temperature and reaches up

to 200000 at helium temperature. Thermal noise gradient and other noise contributions for Kolibri and qPlus are summarized in the Figure **1.8**.

Temperature	Sensor	$\Delta k_{thermal}$ [mN/m]	$\Delta k_{detector}$ [mN/m]	Δk_{drift} [mN/m] ΔT=0.1 K at 300 K ΔT=1 mK at 4 K
300K	qPlus	25	58	0.05
	Kolibri	34	33	31
4K	qPlus	0.5	29	0.04
	Kolibri	2.8	33	21.6

Figure 1.8: The summary of noise contribution for both qPlus and Kolibri sensor at 4 K and 300 K. Quality factor Q taken for the calculations for Kolibri is 50000 at 300 K and 100000 at 4 K, for qPlus sensor Q is 3000 at 300 K and 200000 at 4 K. The resonant frequency and spring constant is 1 MHz and 1080 kN/m for Kolibri and 30 kHz and 1800 N/m for qPlus respectively. Thermal frequency drifts at 300 K, were calculated using formula **1.24**, at 4 K for both sensors the relative frequency drift was assumed to be 1 ppm/K. All noise sources were calculated for B=100 Hz and A_{osc}=100 pm.

Instrumental detection noise

This contribution depends on the type of sensor used and the properties of its deflection detection system. One of the the most important factors of detection noise is deflection noise density n_q, which determines the accuracy at which frequency changes can be measured. The frequency and force gradient noise can be described with [51]:

$$\frac{\delta f_{det}}{f_0} = \sqrt{\frac{2}{3}} \frac{n_q B^{3/2}}{A_{osc} f_0} \tag{1.22}$$

$$\Delta k_{det} = \sqrt{\frac{8}{3}} \frac{k n_q B^{3/2}}{A_{osc} f_0} \tag{1.23}$$

For the calculations, the values of deflection noise density were taken from [51], that is 1.89 fm/$\sqrt{Hz}$ for Kolibri and 62 fm/$\sqrt{Hz}$ and 31 fm/$\sqrt{Hz}$ for qPlus at 300 K and 4K, respectively.

Thermal frequency drifts

While performing precise AFM experiments, for instance force spectroscopy, it is important that the sensor oscillation is kept at its eigenfrequency f_0. The variations in the temperature can lead to changes in eigenfrequency. This behaviour is material depen-

dent, for silicon cantilevers is linear with temperature 35 ppm/K, while for quartz based sensors has a parabolic character. In the case of LER and tuning for sensor the drift in eigenfrequency changes quadratically with the temperature, with parabola centred at the turnover temperature T_P:

$$\frac{\delta f_{sensor}}{f_0} = \chi(T - T_P)^2 \tag{1.24}$$

Where coefficient $\chi = 35 \times 10^{-9} K^{-2}$. The turnover temperature depends on the crystal cut, for Kolibri sensor is usually $\approx$ 313 K, while for qPlus $\approx$ 298 K. The noise related to this type of drift expressed in force gradient is:

$$\delta k_{tsdrift} = -2k\chi(T - T_p)^2 \tag{1.25}$$

The relation **1.24** is valid only around turnover temperature T_p. A detailed analysis of frequency drifts was done by Pielmeier [52] for LER, tuning fork and different geometries of qPlus sensors in the range 4.8-48 K. In the case of LER sensor the relative frequency drift is $\approx$ -0.46 ppm/K while for qPlus goes up to $\approx$ -1.69 ppm/K (depending on the geometry).

1.9 Our experimental setup

All the experiments presented in this manuscript were performed with a Joule-Thomson (JT) Scanning Probe Microscope (SPECS), working in ultra-high vacuum (UHV) at low temperature, down to 1.2 K, thanks to a Joule-Thomson cooling stage. Also, there is a possibility of using magnetic field of maximum 3 T.

The system consists of three chambers: load lock, preparation and analysis chamber separated with gate valves. In the two former chambers there are manipulators that enable the transfer of the samples and tips between the individual chambers. The pressure obtained in the load lock is of the order of 10^{-8} mbar, whereas for preparation and analysis chambers is about $2{\times}10^{-10}$ mbar.

Load lock

This chamber is used for introducing and taking out the samples from the system. The load-lock door is sealed with a viton gasket, this is why the minimal pressure obtained is 10^{-8} mbar.

Preparation chamber

The preparation chamber is situated between load-lock and analysis chamber and as its name implies, is used for preparation of the tips and samples. It is equipped with an

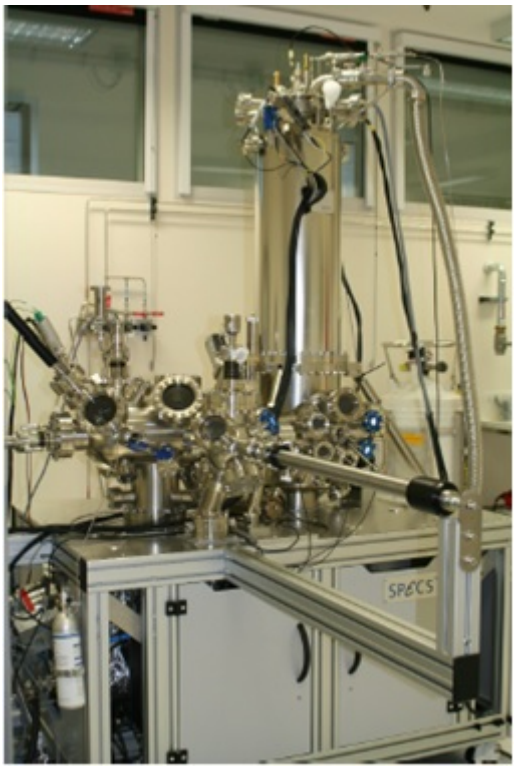

Figure 1.9: Image of JT UHV system

ion sputter gun for bombarding with high energy argon ions and a heating stage used for annealing the samples. Moreover, it contains a Knudsen cell evaporator (Kentax 3-cell TCE-BSC) used for deposition of the molecules.

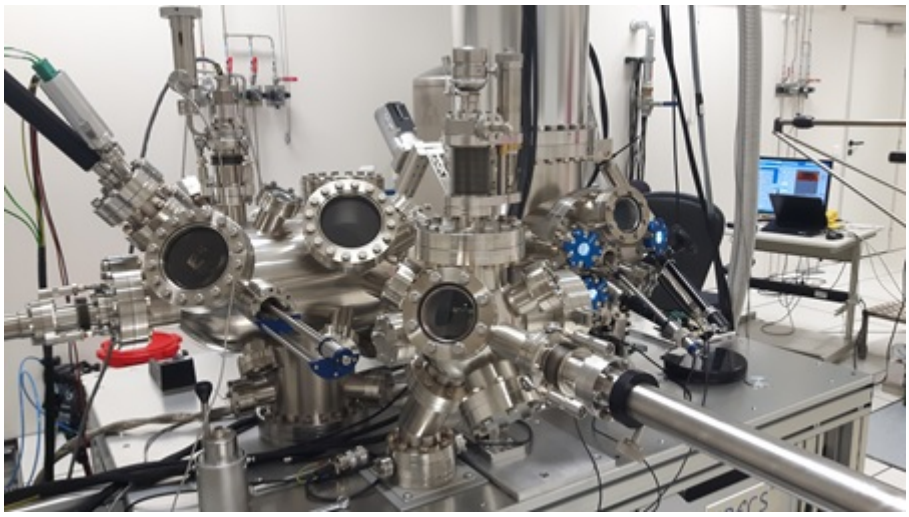

Figure 1.10: Photo of the preparation chamber with ion sputter gun and heating stage

Analysis chamber

In this chamber JT microscope is situated, with the sample stage mounted below

liquid helium bath cryostat and surrounded by another vessel with liquid nitrogen. On the outer LN_2 shield there are four parking positions used for the storage and cooling the samples before introducing them into the microscope. The minimal drift values found in X,Y directions were ≈ 150 pm/h, whereas in Z direction ≈ 200 pm/h.

1.10 Tip preparation

After introduction in UHV, Kolibri tips are cleaned by sputtering during 15-30 min with 3 keV argon ions, under the pressure of 1-2×10^{-5} mbar. Subsequently, tips are sharpened by conditioning during scanning, through bias pulses and tip indentations in the surface in order to obtain sharp form and small apex of the tip. In the case of tip crash on the surface, bent tips were possibly recovered using FIB (Focused Ion Beam) technique present in the Nanofabrication Clean Room of IEMN. An example of a bent tip recovered with FIB is presented in the Figure **1.11**.

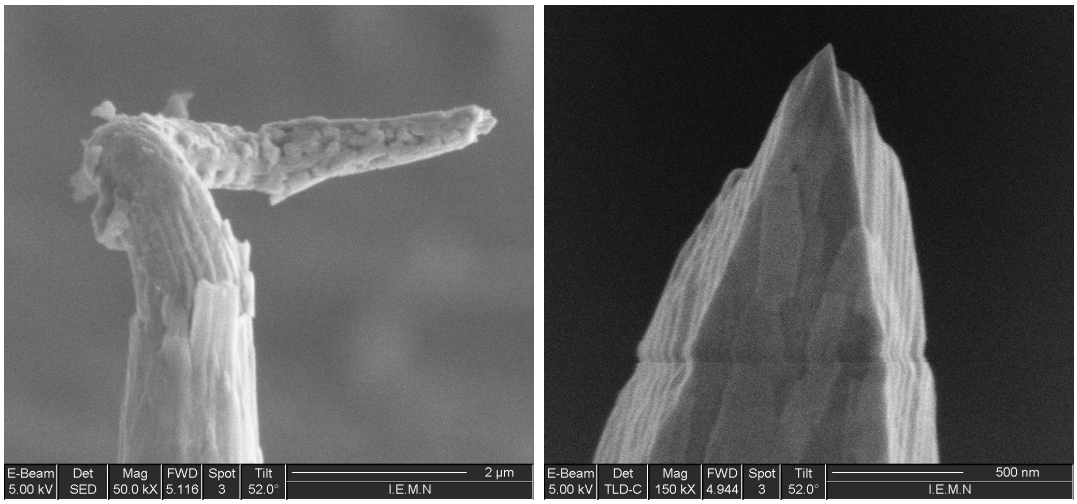

(a) (b)

Figure 1.11: SEM images of Kolibri tip a) before and b) after recovery with FIB

1.11 Sample preparation

1.11.1 Si(111)-$(\sqrt{3} \times \sqrt{3})R°30$-B

Silicon crystallizes in a diamond structure, which is formed by two face centered cubic (fcc) lattices shifted with respect to each other. The size of the cube side measures a=0.543 nm, while the distance between two neighbouring silicon atoms is 0.235 nm (see Figure **1.12a**).

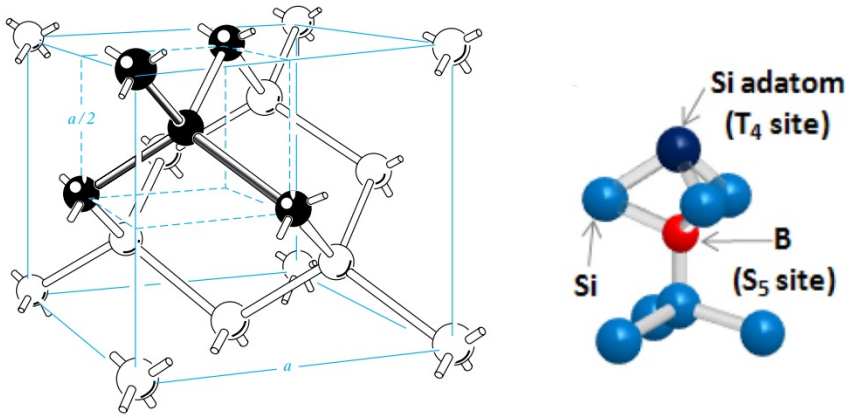

(a) (b)

Figure 1.12: a) Diamond structure of a silicon made of 2 fcc lattices, adapted from [53], b) structural model of Si-B surface reconstruction from [54]

In Si, atoms in the bulk have four neighbours, while the Si (111) surface atoms have only three. Therefore, each of the surface atom possesses an unsaturated bond oriented perpendicular to (111) surface plane called dangling bond (DB). The presence of DBs is responsible for a high reactivity of the surface, such that deposited molecules will form strong interaction with the substrate, hindering the assembly process. Suitable treatment of silicon highly doped with boron can overcome this problem by passivating the surface DBs. During the annealing of the sample, the boron dopants migrate and stay in the subsurface layer at so called S_5 sites, directly below silicon adatoms (T_4 sites) [3] (See Figure **1.12b**). Since boron has only three valence electrons it can catch an extra electron from the dangling bond of silicon adatom above. This results in the passivation of DBs of outer silicon layer and in inertness of the surface. In our experiments we used silicon wafers highly doped with boron with resistivity of 0.001 Ω.cm. Before introduction in UHV, the samples were firstly cleaned with hydrofluoric acid (HF) and then treated with UV ozone for 15 min in order to grow a proper oxide. Subsequently, in UHV system the sample was mounted in a special holder and then placed in the direct heating stage (in the preparation chamber) which allows to heat the substrates through Joule effect, where the passing current over the sample causes the rise of its temperature. The preparation was done in the following steps:

- Firstly the sample was slowly heated up to 900 °C in order to degas the sample and remove the oxide layer (around 700 deg C)
- Several flashes were done (10-15 flashes) until 1200 ° C to remove the contaminants of carbon and to reconstruct the surface

- The temperature of 900 °C was kept for few hours to allow boron dopants segregation to the surface
- The temperature was finally decreased slowly to keep sufficient mobility of silicon adatom

Si(111)-$(\sqrt{3} \times \sqrt{3})R°30$-B reconstruction

The preparation process leads to the migration of boron atoms to the surface and the creation of Si(111)-$(\sqrt{3} \times \sqrt{3})R°30$-B reconstruction, rotated by 30° to the unit cell of bulk (111) structure. The distance measured between two surface adatoms is 0.66 nm which is in accordance with a theoretical value. For the sake of simplicity this surface reconstruction will be named as Si:B in the manuscript.

1.11.2 Deposition of molecules

Sublimation of the molecules and their deposition on the substrates is done using evaporator Kentax (TCE-BSC) placed in the preparation chamber. The evaporator consists of three quartz crucibles with a shutter mounted on top, which serves for opening and closing individual cells. Also it is possible to make co-deposition of the substances in two or three different crucibles. The molecules in the crucibles are in the form of a powder which is heated using tungsten wires until the sublimation. The temperature is measured by a thermocouple and regulated by the power supply. The evaporator is mounted on a linear translation stage (170 mm) behind a gate valve, allowing loading molecules without venting the preparation chamber. Before evaporation of molecules, the crucible is degassed slowly up to the sublimation temperature, in order to remove the water and solvents used in synthesis process and keeping correct level of pressure in the preparation chamber. When the sublimation temperature is reached, the shutter is opened and the molecules are deposited on the sample placed exactly in front of the evaporator (perpendicular to molecule flux). Due to the difference in the sublimation temperatures of molecules used, the cooling system (with water) is installed to prevent the rise of the temperature in the others crucibles during the heating and evaporation. In this thesis, all evaporations have been performed at same distance (around 15 cm) and perpendicular to the molecule flux in order to provide similar evaporation conditions and increase the reproducibility of obtained depositions. Two molecules investigated in this thesis were provided and synthesized in the research group of Frédéric Cherioux (FEMTO ST):

- CDB-I molecule (name in the manuscript): 1-(4'cyanophenyl)-2,5- bis(decyloxy)-4-(4'-iodophenyl)benzene
- CDB molecule: 1,4 bis(4'cyanophenyl)-2,5bis(decyloxy)benzene

1.12 Topography imaging modes

In this thesis both STM and nc-AFM measurements were performed, with most often the STM preceding the AFM experiment. Two different imaging modes implemented are shown in the schemes of the Figure **1.13**. STM imaging is done with constant current I_t regulation, such that the tip follows the profile of constant density of states (often called STM topography). Furthermore, the tip oscillation is activated, so the setpoint is a mean value of the current during one oscillation cycle. Afterwards, in order to perform AFM measurements the z-feedback loop is opened, the bias on the sample V_s is reduced and the scanning is done in the constant height mode. It means that the tip is scanning parallel to the surface plane and the detected signal is a frequency shift of the sensor. Subsequently, the tip is approached slowly to the sample (with steps of 10 pm) until a high resolution imaging is achieved.

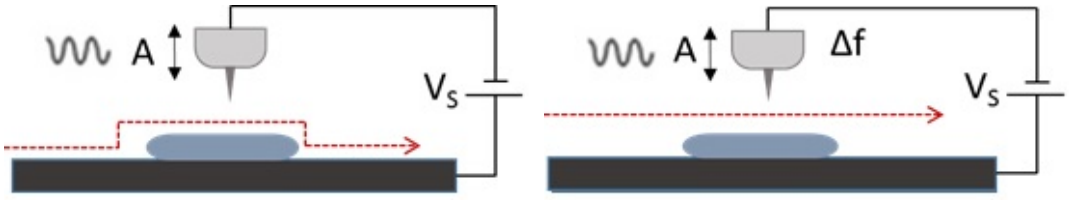

(a) (b)

Figure 1.13: Imaging modes used in the experiments, a) STM with constant current regulation (z feedback closed), b) AFM constant height mode (z feedback open)

1.13 Spectroscopy methods

In order to get deeper insight into properties and interaction mechanisms of investigated molecules, different types of spectroscopies were performed in this work:

- frequency shift versus bias $\Delta f(V_s)$
- tunnelling current versus bias $I_t(V_s)$
- frequency shift versus distance $\Delta f(z)$

In each spectroscopy at first, the tip is positioned at the certain place of the sample and then the Z-feedback loop is turned off during the spectroscopy measurements. During the spectroscopy experiments other parameters can be also recorded, including amplitude, phase or excitation.

1.13.1 Frequency shift versus bias spectroscopy

Modelling the tip-sample system as a metallic capacitance $C(z)$, we can write the formula for gradient of electrostatic force as:

$$\frac{\partial F}{\partial z}(z_0) = \frac{1}{2}\frac{\partial^2 C(z)}{\partial z^2}(V_{bias} - \frac{\Delta\Phi}{e})^2 \tag{1.26}$$

where $\Delta\Phi = \Phi_{sample} - \Phi_{tip}$ is the difference between work functions of the sample and the tip. With the presence of charges in the tip-sample capacitance, an additional term of the electrostatic potential $V_Q(z)$ must be taken into account in the equation:

$$\frac{\partial F}{\partial z}(z_0) = \frac{1}{2}\frac{\partial^2 C(z)}{\partial z^2}(V_{bias} - \frac{\Delta\Phi}{e} - V_Q(z))^2 \tag{1.27}$$

Combining Equation **1.27** and **1.9** leads to the relation between frequency shift signal and the bias:

$$\Delta f = -\frac{f_0}{2k}\frac{\partial^2 C(z)}{\partial z^2}[(V_{bias} - \frac{\Delta\Phi}{e})^2 - 2(V_{bias} - \frac{\Delta\Phi}{e})V_Q(z) + V_Q(z)^2] \tag{1.28}$$

The spectroscopy $\Delta f(V)$ experiment consists in recording frequency shift in function of applied bias on the sample; from the maximum of the parabola we can obtain information about the contact potential difference and the charges present in the sample. The different signal contributions can be dissociated using spectroscopic analysis of the Δf signal [55]. In the Equation **1.28** three different signal contributions appear: a quadratic, a linear and a constant term with sample bias. Importantly, the model of capacitor applied here treat the sample and the tip as continuous-like metallic bodies. At short tip-sample distances, another mechanism needs to be included, involving mostly polarization effects. In that case, an additional term, with a linear dependence on the sample bias should be considered, which stems from the short range electrostatic force [40, 56, 57]. This linear effect can be phenomenologically incorporated into the equations **1.27** and **1.28** as part of $V_Q(z)$ and thus, be taken into account though a parabolic analysis of Δf(V) spectroscopic curves (see here below). A typical spectroscopic curve is presented in the Figure **1.14**.

1.13.2 Tunnelling current versus bias spectroscopy

Using scanning tunnelling spectroscopy we can obtain the information about the electronic properties of the system on the nanoscale. In order to obtain the value of the tunnelling current between the metallic tip approached to the sample at the distance d the integration of the transmission coefficient of the tunnelling barrier must be done by

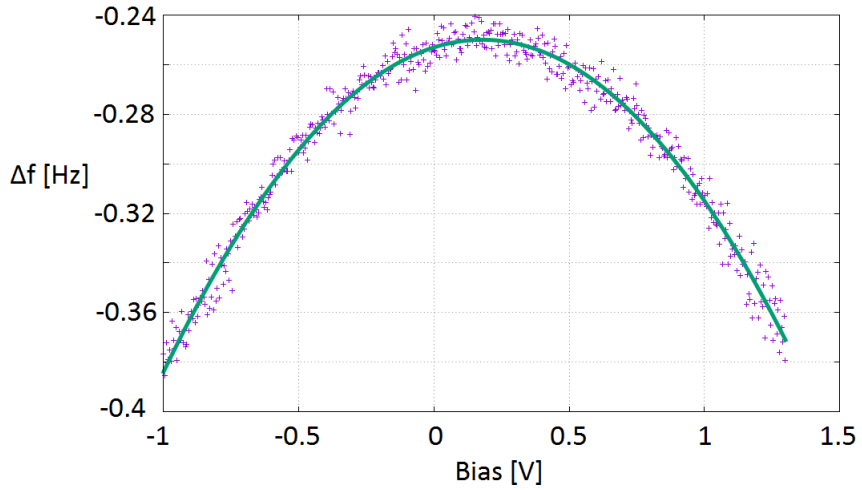

Figure 1.14: Frequency shift versus bias spectroscopy curve presenting parabolic character. The spectroscopy was done on Si:B without z-regulation, with A_{osc}=50 pm. In the plot, violet crosses correspond to experimental data points, the fitted parabolic curve is indicated on green. In the graph, the instrumental offset in Δf signal is observed due to the frequency thermal drift.

all the energy states E from 0 to eV [58]:

$$I = \int_0^{eV} T(E, eV)\rho_{tip}(E, eV)\rho_{sample}(E)\mathrm{dt} \tag{1.29}$$

where ρ_{tip}, ρ_{sample} are the local densities of states of the tip and the sample and eV is the bias applied to the sample. For small eV we can assume that ρ_{tip} and T stay constant, such that the current will depend mostly on the local density of states (LDOS) of the sample. Differentiating the tunnelling current by the bias leads to:

$$\frac{dI}{dV} \propto \rho_{sample}(eV) \tag{1.30}$$

where the derivative of the current is proportional to the local density of states of the sample. The shape of the measured derivative is independent on tip-sample distance, by changing the polarity of the applied bias we can get information about both occupied and empty states of the surface.

1.13.3 Frequency shift versus distance spectroscopy

This spectroscopy is an equivalent of a force curve performed in contact mode AFM. The procedure relies in measuring frequency shift signal while decreasing the distance between the tip and the sample. Most often, the spectroscopic measurement contains two curves, for approach and retract Δf measurements. During the experiment, it is common to apply the bias on the sample which is equal to the surface potential in order

to compensate capacitive long range electrostatic forces. Moreover, it is recommended to start imaging after the spectroscopy to check any possible changes of the tip. As a signal of frequency shift is an observable measured in nc-AFM measurement it must be then converted to the force. There has been several methods of extracting the force from spectroscopy $\Delta f(z)$, which are mentioned in the section **1.3** of this manuscript.

Due to the fact that KPFM is the principal technique used for the electric measurements presented in this work, Δf(V) spectroscopy and different signal contributions were described in details. Other spectroscopy techniques: $I(V)$ and $\Delta f(z)$ were explained shortly as well but will not be used systematically in the work presented here.

1.14 Summary

In this introductory chapter the principles of main scanning probe techniques have been explained, including STM and AFM. The oscillator model for tip-sample system was described and the most important parameters characterizing nc-AFM experiment. The introduction to imaging molecules with high stiffnes probes: Kolibri and qPlus was done as well. In the second part of the chapter the experimental details of measurements have been presented. In the last section different spectroscopy methods were explained with a particuler focus on Δf(V) spectroscopy, which is the main technique used in this work. In the next chapter KPFM measurements on Si:B defects are presented with the objective of detecting single charge using Kolibri probe.

Chapter 2

Charge detection of Si(111)-$(\sqrt{3} \times \sqrt{3})R^{\circ}30$-B defects

In this chapter, charge spectroscopy measurements performed on defects of boron doped silicon surfaces are presented. We are interested in the possibility to use Kolibri sensors to detect single charges using Δf(V) spectroscopy at 4 K, and in the high-resolution imaging of such charges. The Si:B surface constitutes an interesting example of a surface with several defects characterized with different charge states, which have been previously studied with STM [59, 60, 61]. The only nc-AFM work presented so far deals with LCPD measurements obtained as point-spectroscopy as a function of tip-sample distance [62], however the information about the lateral variation of the surface potential above surface defects is missing. In our experiments we observe and map the charge states carried by either Si dangling bonds, buried ionized boron dopants and Si vacancies, which fall in accordance with previous STM and theoretical studies. A detailed analysis of spectroscopy measurements permits the obtention of maps of the surface potential, together with maps of capacitance and van der Waals signals. The effect of the tunnelling current on the sensor frequency shift, known as "phantom force", is studied as well[63, 64], and leads to the detection of additional frequency shift features in the Δf(V) spectroscopy.

Spectroscopy experiments were previously realized with qPlus sensors on single gold atoms deposited on NaCl/Cu(111) substrate[13, 21]. These measurements included the determination and the manipulation of a charge state of an atom by the use of Δf(V) spectroscopy. Although both qPlus and Kolibri sensors belong to family of quartz sensors characterized by a high stiffness, not many studies were presented with the latter. The high stiffness of the LER sensor (k'=1080 kN/m) lays beyond the optimal k for high sensitivity and it is still at issue [51]. The results presented in this chapter will therefore serve as test of sensitivity in charge detection by Kolibri sensor. They show that single charge event detection and single charge mapping is not an issue for such high-stiffness

sensors.

2.1 Previous Si:B studies

The surface of boron doped silicon is of particular interest due to the passivation of silicon dangling bonds and therefore chemical inertness of the surface. In absence of surface defects, the electronic structure of a molecule deposited on this surface is hardly perturbed and its interaction with the substrate consists of van der Waals forces rather than covalent bonding. Due to this fact, Si:B has served in the last years as a substrate for the growth of many supramolecular networks that have been extensively studied with STM [65, 66, 67, 68].

The passivation of a surface silicon atom by an underlying boron atom corresponds to an electron transfer from the silicon atom dangling bond to the boron atom, and results in the formation of a surface dipole. The occasional absence of a boron atom under a surface silicon atom leaves the DB unpassivated, which is one of the mostly studied defects of this surface. It gives rise to a prominent bright contrast in STM images for both occupied and empty states, which makes it easy to discriminate it from passivated adatoms. The dangling bond defect is associated with an electronic state located in the bandgap of the Si surface, with a position of $\approx$ 0.6 V from the valence band (as observed in STM spectroscopy). It has been shown that this state is able to support large tunnelling currents, even more than 1 nA [59]. To explain this phenomenon, the mechanism involving the electron recombination with holes from the acceptor band was proposed, in which the excess of energy is released in form of vibration of the surface silicon adatom. In the Figure **2.1(a)** the schematics of the electron transfer to the DB is shown, corresponding to transition from positively charged to neutral DB state (+/0). The vibrational states are observed in the dI^2/dV^2 spectroscopy with a separation of 31$\pm$3 mV between adjacent peaks (Figure **2.1(b)**). In order to obtain the DB negatively charged, the tunnelling barrier must be furthermore reduced, allowing the transfer of second electron. Continuous occupation of DB state can be provided by saturating the tunnelling current in the dI/dV spectroscopy with keeping the constant value of tunnelling current. It allows in turn approaching the tip close to the surface and leads to observation the second peak in dI^2/dV^2 curve, corresponding to the transfer of second electron in the DB[61].

Another defect observed in STM images is a "buried" boron dopant located in layers under the surface. Because of high doping, the holes are no longer localized on boron atoms even at low temperature, therefore the buried boron dopants are negatively charged. This charge causes band bending at the surface and locally changes the tunnel barrier in STM

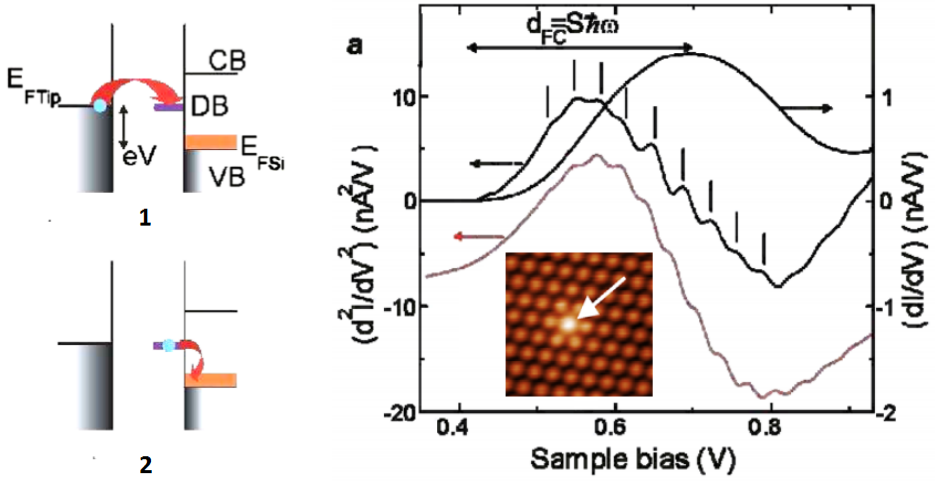

(a) (b)

Figure 2.1: a) Energy diagrams presenting the process of electron transfer from the tip to dangling bond (1) and electron recombination with the hole from the acceptor band (2). b) Spectroscopy curves of dI^2/dV^2 obtained on DB atom from the experiment (black curve) and calculated (red curve), the vertical lines indicate the vibrational states. The spectroscopy was done at 5 K, with parameters of V_{bias}=1.5 V, I_t=500 pA. Adapted from [59].

imaging [68]. It gives rise to a dark or bright blurry contrast for empty and occupied states respectively (shown in the Figure **2.2**), which intensity decreases with the depth of the dopant. By analysing the form of STM contrast it was possible to define in which layer the boron atom is located, starting from fourth layer under the surface. As the STM gives local information of the surface, other techniques were also used to obtain macroscopic results. From the NEXAFS studies the information about position of boron in subsurface layer was acquired [69]. The location of boron dopants highly depends on the preparation of the surface, including the temperature of sample flashing [70]. In the recent STM studies of Si:B surface it has been shown that it is possible to switch the charge state of a single silicon adatom by applying small bias pulse [54]. Each silicon adatom on this surface has two reversible charge states - normal and bright one. The former corresponds to passivated silicon atom while the latter to two electron bound state with displacement of silicon adatom from the surface plane. This negatively charge state presents bright contrast in the STM images, similar to dangling bond defect, however in STS shows a peak in the bandgap at E=0.84 eV, which allows its identification. It has been also shown as well that the bright atom state is quite stable at 78 K and can withstand up to two days [54].

Concerning nc-AFM studies of the boron doped silicon surface, an extensive work has been realized by Spadafora *et al.* [62] in which different defects were investigated, including DB, buried boron dopants and silicon vacancy. This work was realized with qPlus sensor

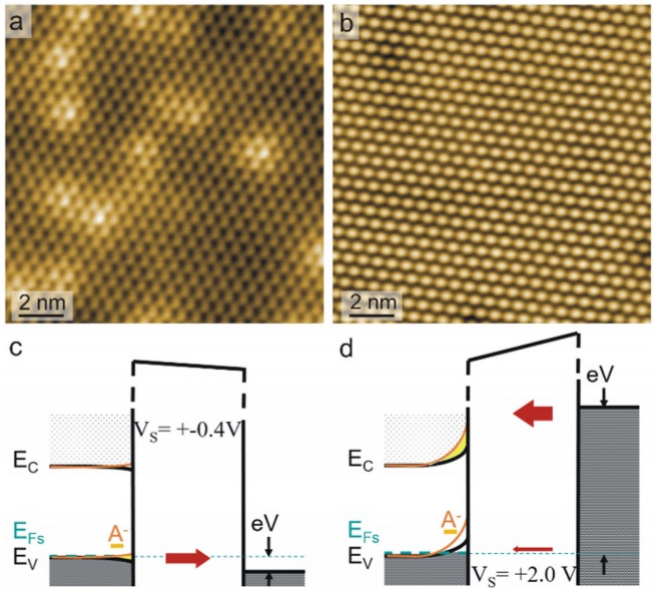

Figure 2.2: STM images presenting change in contrast of boron dopants for a) V_{bias}=-0.4 V, b) V_{bias}=2 V, both images done with current setpoint of 1 nA. Energy diagrams and effect of tip-induced band bending caused by negatively charge dopants for c) occupied and d) empty states. Images extracted from [68].

at temperature of 4 K, and permitted the identification of defects in the constant height frequency shift images. Apart from the topography contrast, the force spectroscopies were performed which consisted in recording Δf, I_t and dissipation signals as a function of the tip-sample distance. Short range forces were calculated from Δf signals, in order to study the reactivity of different surface sites. From the results obtained, the DB defect showed the biggest reactivity with force value of $\approx$ 0.8 nN [62]. Boron in subsurface layers were far less reactive, with a maximum force of $\approx$ 0.2 nN although the value depended on the depth of the defect. Additionally, LCPD measurements as a function of the tip-substrate distance were realized above DB, and regions with smaller and higher tunnelling current (depending whether smaller or bigger amount of boron dopants are located underneath). At closer distances V_{CPD} values start to differ between the defects and present the highest difference for DB but also significant difference between regions of higher and lower tunnelling current (corresponding to bright and dark zones presented in the inset of the Figure **2.3a**), $\Delta V_{CPD} \approx$ 40 mV. Therefore, the arrangement of these defects can influence the assembly process of molecules deposited on this surface [62]. Recently, the surface of boron doped silicon has been used to demonstrate the possibility of tip functionalization with silicon atom [20]. The process was done with a Kolibri sensor tip by means of a controlled indentation in the surface. The single silicon adatom was successfully attached to the tip which resulted in increased resolution in the constant height Δf and I_t images. To confirm the effectiveness of the procedure the vacancy was

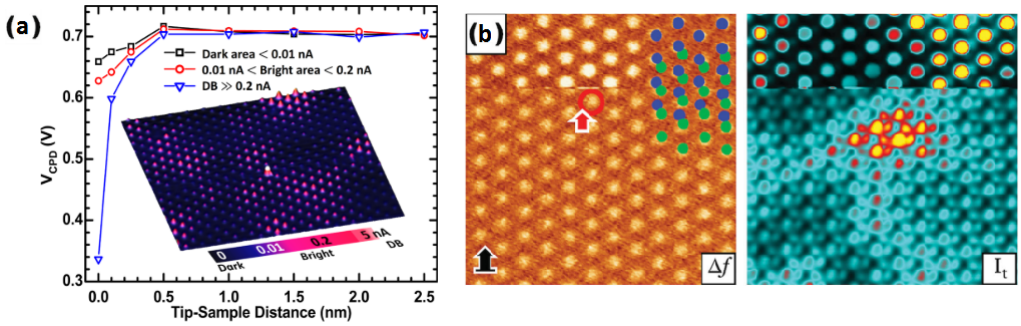

Figure 2.3: a) LCPD measurements in the function of tip-sample distance z for dangling bond, bright and dark regions in the I_t map (correponding to the zones of high and low tunnelling current), in the inset I_t map extracted from constant height image. b) Increase in resolution in Δf and I_t after picking-up a silicon atom from the surface shown in b), images done with V_{bias}=-10mV. Red arrow displays the position of Si atom used for functionalization procedure, green and blue circles indicate the positions of atoms before and after functionalization. The images shown in a) extracted from [62], b) from [20].

observed in the place of indentation with three underneath silicon atoms in the first subsurface layer, as shown in the Figure **2.4**. The high resolution achieved with Si tip make it a promising candidate of tip termination, which is crucial in imaging molecules, as compared to most frequently used carbon monoxide functionalization on metallic surfaces.

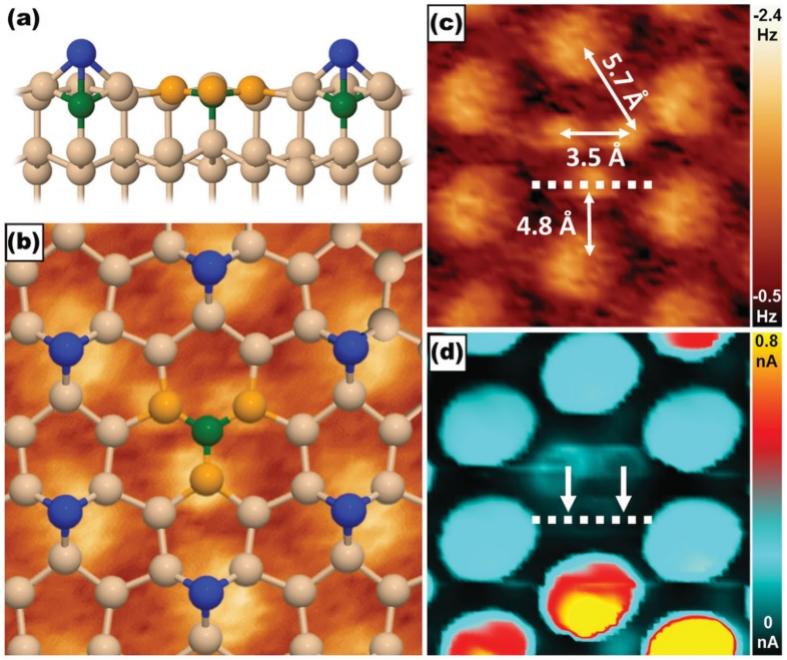

Figure 2.4: a) The model of Si-B surface first bilayer with silicon vacancy, b) the same model from the top view showing three silicon atoms in the subsurface layer (indicated with yellow) and boron atom (indicated with green). Increased resolution after tip functionalization with silicon atom in c) frequency shift and d) tunnelling current image from AFM measurement. Adapted from [20].

2.2 Identification of defects with STM and AFM

During the preparation of the Si(111)-$(\sqrt{3}\times\sqrt{3})R°30$-B reconstruction, the sample is kept at 900° C during several hours to allow the segregation of boron in the subsurface layer and passivation of silicon dangling bonds. Nevertheless, on the large scale, the surface reconstruction is not perfect and different types of defects can be found. Figure **2.5** shows STM images of Si-B surface for empty and filled states with different defects indicated. The first noticeable defect in the empty state image is a bright protrusion with 'flowery' shape which stays bright in the filled state STM, however surrounded by a darker contrast (indicated with blue colour in **2.5**). This defect corresponds to non-passivated dangling bond, caused by the absence of boron underneath the silicon adatom (silicon atom in S_5 site). The dark halo around the DB in **2.5(b)** was formerly associated with Coulomb interaction between the holes and charged DB [60]. Another defect, giving a darker contrast in **2.5(a)** is a buried boron dopant, located in a deeper subsurface layer, starting from fourth layer under silicon adatom plane. Depending on the depth of the dopant, the contrast in STM varies, giving rise to a bright blurry contrast in the filled state STM. A third defect (indicated with yellow circle in **2.5**), in the form of dark adatom in the empty state STM corresponds to silicon vacancy. The contrast of this defect has a hexagonal bright form in the corresponding filled STM image. Moreover, we notice the presence of additional irregular defects, also changing their contrast in filled/empty STM images, that we associate with surface adsorbates (see *e.g.* the defect marked with a black circle). Figure **2.6** shows an AFM experiment performed in the

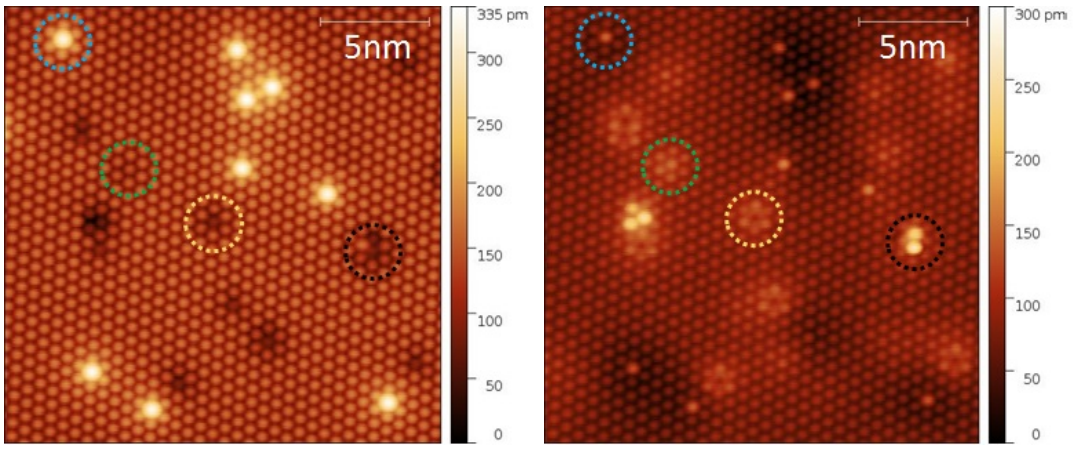

(a) (b)

Figure 2.5: STM images of the Si:B surface reconstruction presenting different types of defects for a) empty states (V_{bias}=1.5 V, I_t=10 pA) and b) filled states (V_{bias}=-0.5 V, I_t=10 pA). Oscillation amplitude A_{osc}=100 pm. Defects are indicated with different colours: dangling bond-blue, buried boron dopant-green, vacancy-yellow, adsorbates-black.

constant height mode, of the same zone as in the STM images of Figure **2.5**. Prior to AFM imaging, the tip was lifted by 500 pm, the sample bias was gradually reduced to 0 V and the oscillation amplitude was decreased to 50 pm. Subsequently, the tip was slowly approached to the surface until atomic resolution was obtained. Besides the frequency shift signal, different parameters were registered as well, including phase and excitation, as shown in **2.6(a)-2.6(d)**. Despite zero bias applied on the sample, a residual signal was

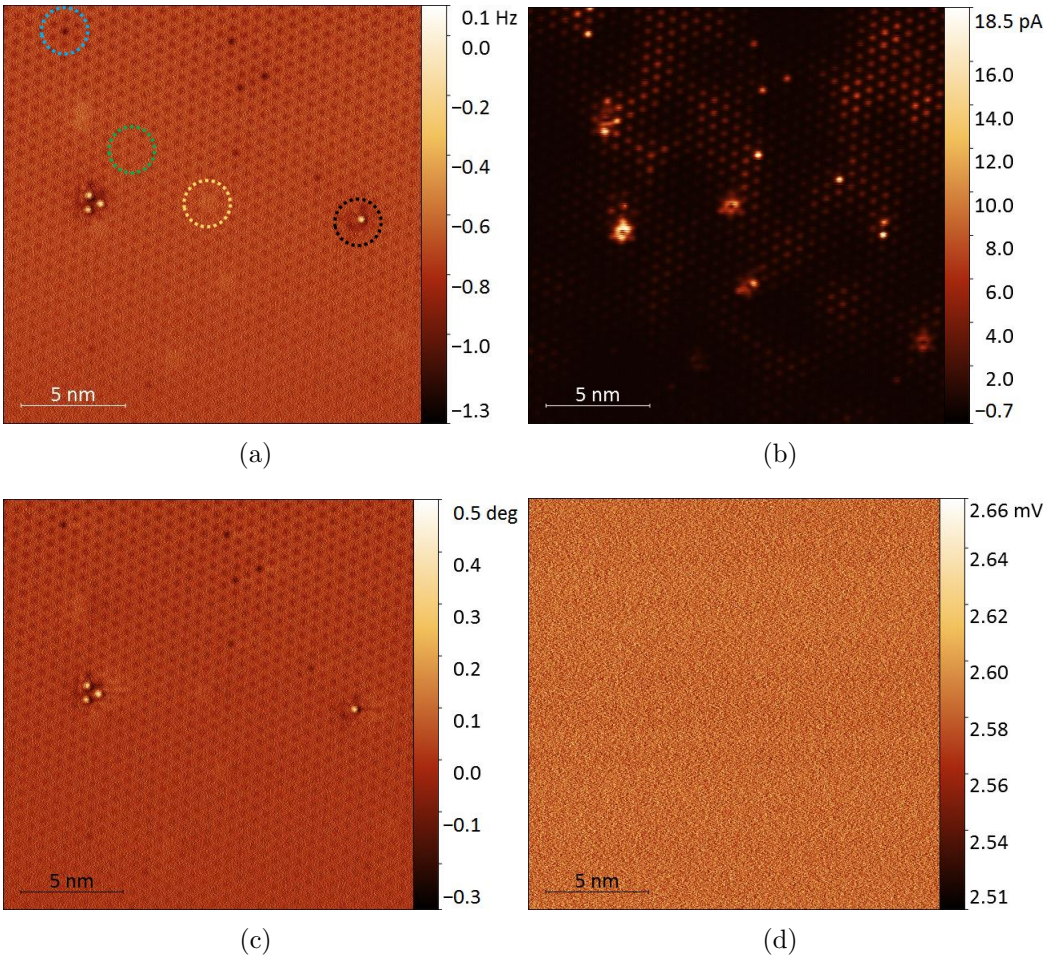

Figure 2.6: AFM images of Si:B surface (the same zone as in the Figures **2.5**) done in constant height mode with A_{osc}=50 pm, V_{bias}=0 V and different experimental channels: a) Δf, b) I_t, c) phase, d) excitation channel.

also detected in tunnelling current channel presumably caused by a sample bias offset at the electronics output. It allows for additional identification of different defects from STM view. A residual current of maximum 18.5 pA was measured in the image, which serves here exclusively to compare the contrast on different defects. The frequency shift signal measured above normal silicon adatoms is negative, indicating an attractive force regime in which the tip was scanning. In the AFM images we recognize different defects described above. For a dangling bond, frequency shift contrast is more negative and the value of

tunnelling current is higher compared to passivated adatoms, $I_t \approx 20$ pA. The absence of adatom is sighted for silicon vacancy in Δf, giving a round shaped contrast in I_t image. In the case of buried boron dopant no variation of signal is detected in Δf channel, probably owing to the weak interaction between the tip at zero bias and the defect located deep under the surface plane. Nonetheless, for atoms with the same Δf contrast, we distinguish different regions, showing smaller or higher tunnelling current. This variations are caused by changes in electronic properties, stemming from different depth and organisation of boron dopants under the surface [62]. We observe the adsorbent defects as well, presenting bright contrast in both Δf and I_t, due to greater height compared to other defects.

2.3 Single point $\Delta f(z)$ spectroscopy

Spectroscopy measurements were done in the constant height mode with Z-feedback loop open, similarly to AFM imaging. The spectroscopy relied in measuring the frequency shift signal in function of the sample bias applied, at the fixed z-position. Additionally, other experimental parameters were registered during the sweep, including tunnelling current and excitation, which provide more detailed information about the defect. Before the measurement, the tip was lifted by 150-250 pm from AFM scanning conditions (depending on the measurement), so as not to pass too much current that would perturb Δf signal. Moreover, it allowed to increase the oscillation amplitude in order to reduce the noise in Δf signal. The example of a spectroscopic curve is presented in the Figure **2.7**.

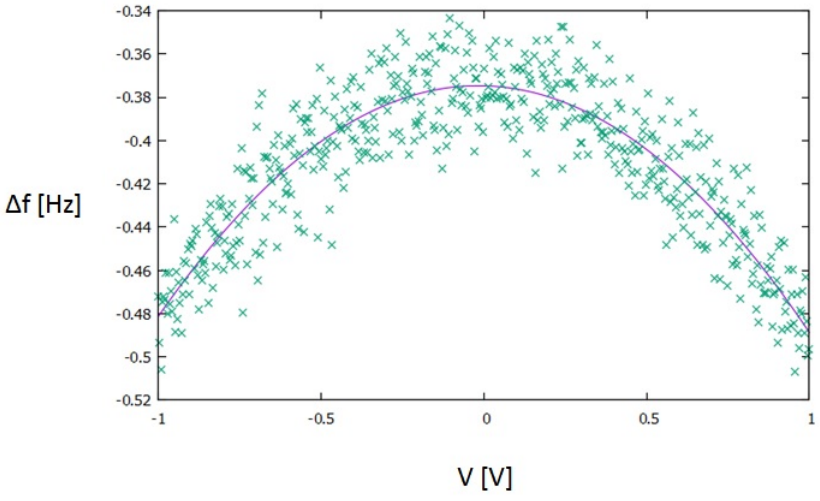

Figure 2.7: Spectroscopy Δf(V) curve above passivated silicon adatom. Spectroscopy experimental points (blue crosses) showing parabolic dependence (fit curve in violet).

Considering a parallel plate capacitor model of tip-sample system leads to relation of the frequency shift signal being proportional to the second derivative of the tip-sample

capacitance and with parabolic behaviour with sample bias. The model has been described in the section **1.13.1**. Parabolic function in canonical form $\Delta f = A + B \times (V_{bias} - V_s)^2$ was fitted to experimental data, which permitted direct access to contributions of van der Waals, capacitance and surface potential respectively. The analysis of Δf(V) signal leads to three different information:

- surface potential V_s - this value corresponds to the bias at the maximum of Δf(V) function (vertex of the parabola). V_s contains both the information about the tip and the sample work functions difference, as well as additional (local) electrostatic contributions (for example, a local charge). This last contribution was described as $V_Q(z)$ in the equation **1.28**,
- capacitance - represented by the concavity of the parabola, coefficient B [Hz/V^2],
- all interactions independent on the tip bias: van der Waals forces, image charge contribution with presence of local charges. This signal is measured for V_{bias}=V_S and is represented by coefficient A in the equation. It may also include in practice an offset on the resonant frequency of the probe f_0, if any (for instance in case of thermal drift).

2.4 Experimental method

2.4.1 Grid procedure

In order to acquire the lateral distribution of surface potential, van der Waals (+image charge) and capacitive force contributions, a grid spectroscopy over different defects was performed. All grids presented in this manuscript were carried out starting from AFM 'constant height' imaging, except for the comparison done in section 2.4.2. The grid of specified X,Y points was set over an AFM image of the defect, providing sufficient lateral resolution. In the each point of the grid several spectroscopy measurements Δf(V) were done (4-6 curves) in order to verify the reproducibility of the experiment and to reduce Δf noise. The average curve was further analysed and all the signal contributions were extracted. Despite the small lateral and vertical drift at low temperature, in long experiments the displacement of the defect in the scanning zone can be observed. A procedure of drift compensation in Δf(V) and Δf(z) mapping was previously described by Mohn [71]. In this method, initially the STM is done, which serves as an reference for subsequent measurements. Next, the feedback loop is open and the spectroscopy is performed. Every 20 min, the measurement is stopped, the loop is closed and again the STM imaging is done. This STM is correlated with the reference image so as to calculate

and compensate for the drift. Then, the spectroscopy is continued in the same manner. Although such a procedure can ensure exact positioning of spectroscopy measurements with respect to the topography, in the experiments presented here no drift compensation was adopted. The AFM image was done prior to and immediately after grid spectroscopy, in order to calculate the drift, which for 2 h grids resulted in lateral displacement of maximum 300 pm.

2.4.2 Constant distance vs constant height mode

There are two possible ways in which grid spectroscopy measurements can be performed:

- in a constant distance mode
- in a constant height mode

In the constant distance mode, the tip-sample distance is kept constant such that the tip follows the topography of the sample. Before spectroscopy in each grid point, the feedback loop is closed and z-regulation is activated whether in STM or AFM. As a result, the z-reference for each spectroscopy is done with respect to STM (AFM) setpoint, which follows (point by point) the sample topography. In the constant height mode, the feedback loop is open in the whole image and no z-regulation is activated. Hence, the spectroscopy in each grid point is done at the same height position with respect to the substrate plane. The signal of frequency shift at zero bias can be extracted from the spectroscopy measurement, as well as the tip-substrate capacitance signal, which can serve as a topography reference. As an illustration, a comparison of Kelvin probe spectroscopy done along a line on a molecule in constant distance and constant height mode is shown in the Figure **2.8**. The molecule in the example is not studied in this thesis and its structure will not be described here as the illustration focuses on the KPFM results while scanning above any nano metric object. The implementation of the constant distance mode for spectroscopy measurements is justified when the capacitance is kept constant by reproducing the sample topography. However this is no longer the case in the experiments on the nanoscale where lifting the tip above a small object like molecule, leads to a topography footprint artefact. This occurrence can be seen in Figure **2.8**, where three signal contributions are in like manner, that is they follow the topography contour. As the macroscopic part of the tip (and not the extremity) contributes mostly to measured capacitance signal, lifting the tip above the molecule results in overall decrease in tip-sample capacitance, as shown in Figure **2.8(e)**. On the contrary, no artefact is observed for constant height mode where the tip is scanning at the constant height above the sample. Moving over the molecule results

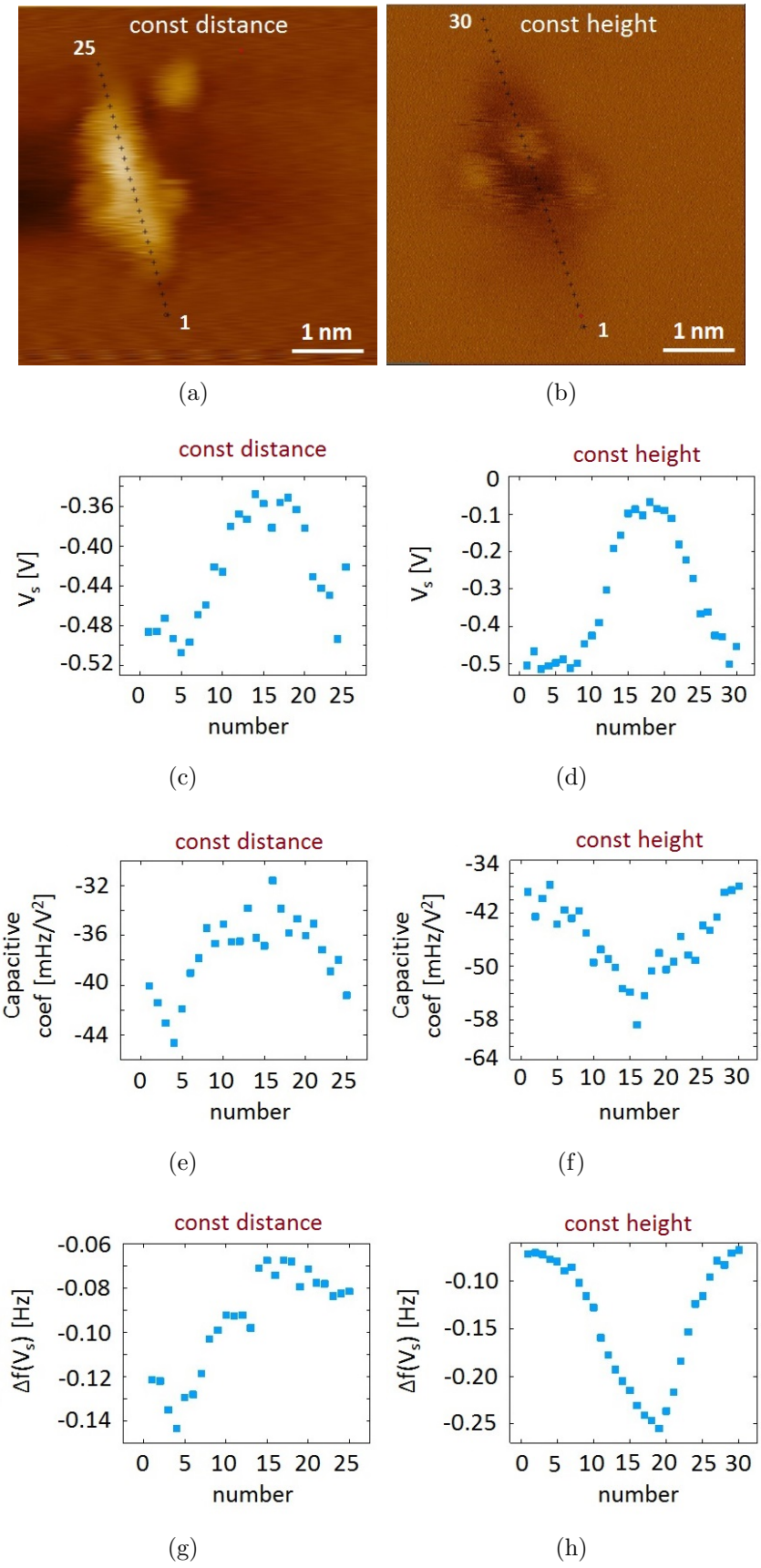

Figure 2.8: Comparison of constant distance and constant height mode for a line spectroscopy of a molecule. Constant current STM image (V_{bias}=-1.9 V, I_t=5 pA) with a line grid of 25 points shown in a), constant height Δf image (V_{bias}=0 V) with line grid of 30 points presented in b). Signal contributions extracted from the spectroscopy : surface potential c),d), capacitance e),f), van der Waals g),h) for constant distance and constant height mode respectively. STM and AFM images were done with A_{osc}=50 pm, all spectroscopy with A_{osc}=100 pm.

in increase of the capacitive force (due to the smaller tip-sample) distance and negative capacitive signal, as presented in Figure **2.8(f)**. Consequently, the constant height mode has been applied in all grid measurements presented in this thesis.

2.5 Grid spectroscopy on a buried boron dopant

Figure **2.9** shows the maps of surface potential, capacitance and van der Waals signal together with incertitudes, obtained on buried boron dopant. The filled state STM image is acquired in a first step, in which boron dopant is more visible. Additionally, as this defect is not apparent in Δf image, it needed to be located preferably in the vicinity of other defects. In our case, two dangling bonds served as a reference for the grid spectroscopy measurements of the dopant (Figure **2.9(a)**-**2.9(c)**). In the next step, the grid of 4.5 nm x 4.5 nm (15x15 points) was imposed on constant height AFM image, centred at the defect but including normal silicon adatoms as well. The tip was lifted by 150 pm and the oscillation amplitude was increased to 100 pm. The parameters of the grid, including the time of integration and number of sweeps were optimized to provide a minimal lateral drift during the experiment, as presented in **2.9(b)**-**2.9(c)**. The duration of the grid experiment was $\approx$ 2 h with the lateral drift of $\approx$ 200 pm. In the surface potential map, that can be interpreted as a charge map, the bright contrast is observed in the middle of the image (Figure **2.9(d)**), corresponding to the negative elementary charge detected over the ionized boron dopant. The capacitance map - as expected - is rather flat and no variation of the signal is detected over the image. In the van der Waals map in turn, **2.9(f)**, a small gradual change in contrast is observed and the signal becomes more negative in the upper part of the image. This change is due probably to the drift in Z during the measurement, such that the tip becomes closer to the surface in the upper part of the grid and results in more negative Δf signal. Additionally, the contrast in this map compared to former AFM image is lost, due to the tip lifting and reduced lateral resolution of the grid. From the cross section in the V_s image we find a mean value of surface potential difference between the boron dopant and normal silicon adatoms of 35 mV $\pm$ 7 mV. The lateral dimension of charge imaged for boron dopant is $\approx$ 3 nm. It is worth noting, that no crosstalk between individual maps of surface potential, capacitance and van der Waals is observed. Furthermore, the quality of the parabolic fit to experimental data (Figure **2.9(h)**) is homogeneous and relatively small, pointing to correct fitting procedure for the full set of spectroscopic data.

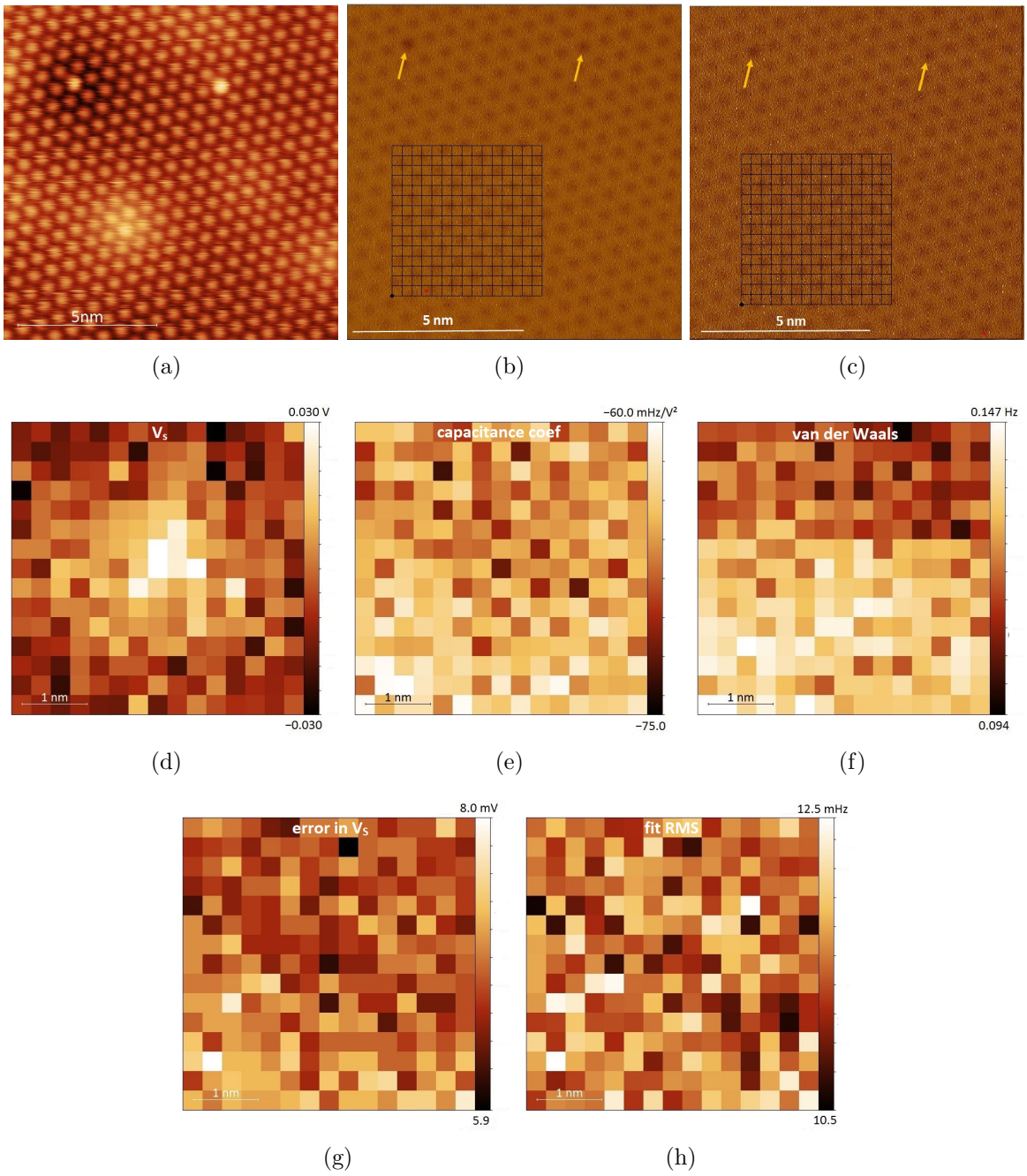

Figure 2.9: Grid spectroscopy measurement on buried boron dopant, a) STM image prior to AFM imaging (V_{bias}=-0.7 V, I_t=10 pA) with boron dopant and two dangling bond defects, corresponding constant height Δf images with grid imposed b) before and c) after the grid experiment. Colour scale for: AFM images -0.9 Hz $< \Delta f <$ 0.6 Hz, STM image $0 < z <$ 160 pm. Signal maps extracted from Δf(V) spectroscopy of d) surface potential, e) capacitance, f) van der Waals signal, g) incertitude of V_s, h) fit error (root mean square (RMS)). STM and AFM images were done with A_{osc}=50 pm, grid spectroscopy with A_{osc}=100 pm. Two yellow arrows indicate the position of DB atoms giving slightly darker Δf contrast.

2.6 Grid spectroscopy on a silicon vacancy

Figure **2.10** shows a grid experiment done on the defect of silicon vacancy (4 nm x 4 nm and 15 x 15 points). A great care was taken in finding an isolated defect that is not disturbed by the properties of other defects in its close proximity. Prior to the spectroscopy, the tip was retracted by 200 pm and the oscillation amplitude was increased

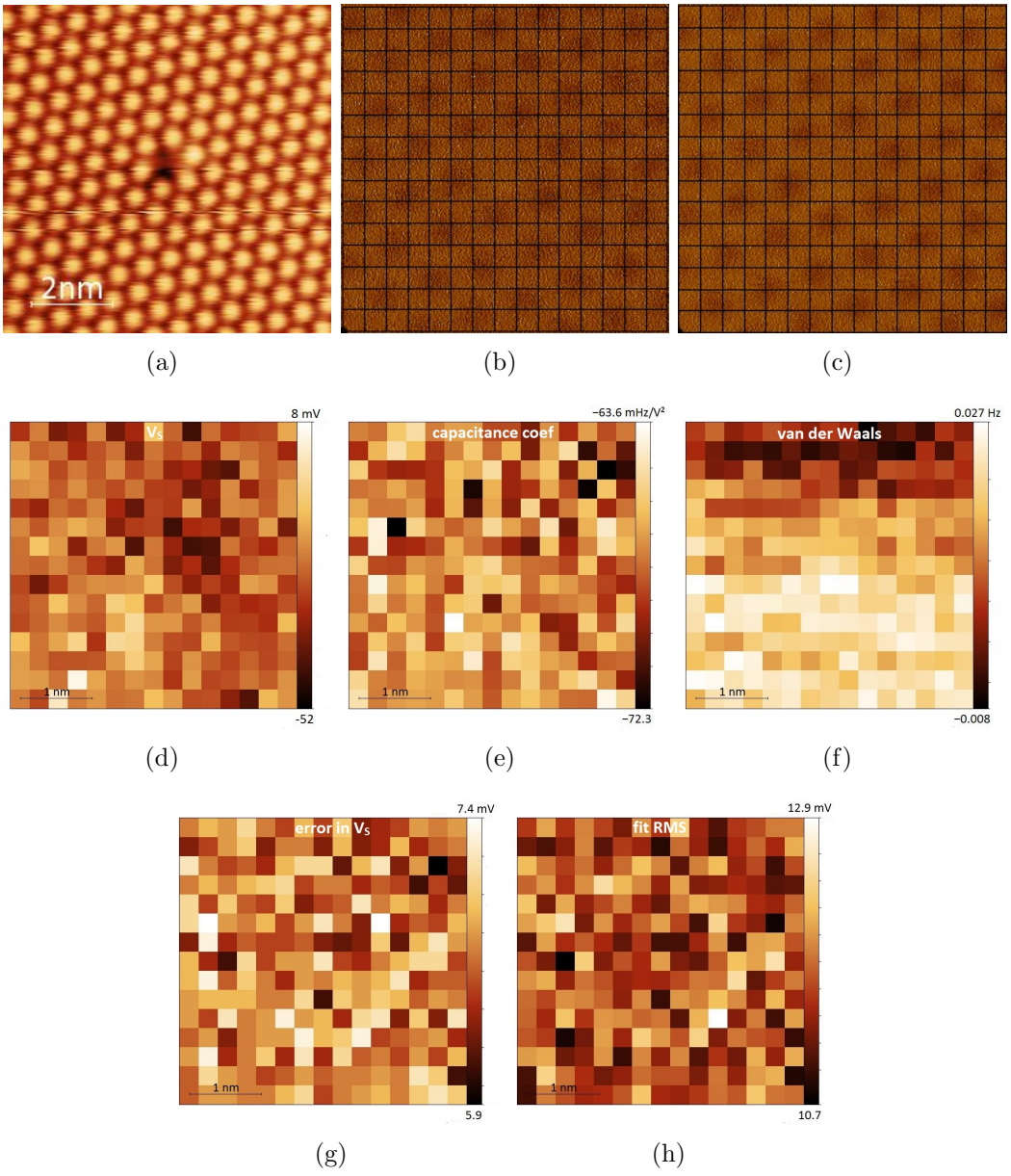

Figure 2.10: Grid spectroscopy measurement on silicon vacancy, a) STM image prior to AFM imaging (V_{bias}=2 V, I_t=10 pA), constant height Δf images of vacancy with grid imposed b) before and c) after the grid experiment. Color scale for: AFM images -1.0 Hz $< \Delta f <$ 0.2 Hz, STM image $0 < z < 120$ pm. Signal maps extracted from Δf(V) spectroscopy of d) surface potential, e) capacitance, f) van der Waals signal, g) incertitude of V_s, h) fit error (RMS) on Δf(V) spectroscopy. STM and AFM images were done with A_{osc}=50 pm, grid spectroscopy with A_{osc}=100 pm.

to 100 pm. By comparison between Δf images before and after the spectroscopy (**2.10(c)**-**2.10(c)**), we estimate the lateral drift of ≈ 100 pm for the 2h grid experiment. Small variations of the signal are measured in V_s map with single fluctuations of maximum 15 mV (shown in **2.10(d)**). Therefore we deduce that the vacancy is an electrostatically neutral defect. Similarly to buried dopant, change in contrast between bottom and upper part of van der Waals chart caused by the vertical drift is observed. Regarding the capacitance plot, no signal contrast is observed, possibly due to the small height difference between silicon adatoms and the vacancy that is indiscernible in this experiments. Once more, no crosstalk between individual signal contributions is observed.

2.7 Grid spectroscopy on a silicon dangling bond

A grid spectroscopy measurement together with STM image before the grid, performed on a non-passivated silicon dangling bond is presented in Figure **2.11**, following the same procedure as for the buried dopant or silicon vacancy. The grid of 2.8 nm x 2.8 nm and 15x15 points was imposed on Δf image of an isolated dangling bond. Before the spectroscopy, the tip was lifted by 150 pm and the amplitude was changed to A_{osc}=100 pm. In Figures **2.11(d)**-**2.11(e)**, an evident correlation is noticed between surface potential and capacitance. In the center of both maps, a bright round contrast is observed with few dark points in the very middle of the grid, corresponding to the DB. Moreover, it can be noticed that the incertitude in the estimation of the surface potential is much higher in the middle of the grid, as shown in **2.11(g)**. This indicates a problem in the fitting procedure to experimental data in this part of the grid. Although the tip is retracted before the spectroscopy and the range of bias sweep is chosen so as not to pass the tunnelling current between the tip and the sample (bias range of -1 V to 1 V), still a significant current is detected. Figure **2.12** shows the examples of I_t map at the voltage of 750 mV, corresponding to DB state located in the band gap and for -950 mV. In the former, the maximum value of current is measured on non-passivated adatom ≈85 pA and decreases to ≈15 pA on first adatom neighbours, whereas for -950 mV the current is detected systematically above all adatoms. For this reason, the spectroscopy curves in each grid point were analyzed individually, to verify if the tunnelling current has an impact on their form. Figure **2.12** presents spectroscopy Δf(V) with corresponding I(V) curves acquired on the dangling bond in the middle part of the grid. An obvious influence of the tunnelling current on frequency shift signal is observed in both cases. As seen in the Figure **2.12(a)**, **2.12(b)** the increase of frequency shift signal and change in the shape of parabola is noticed for the positive bias ≈ 0.5 V which corresponds to abrupt rise of the tunnelling current. For the negative bias, a gradual change in parabolic shape

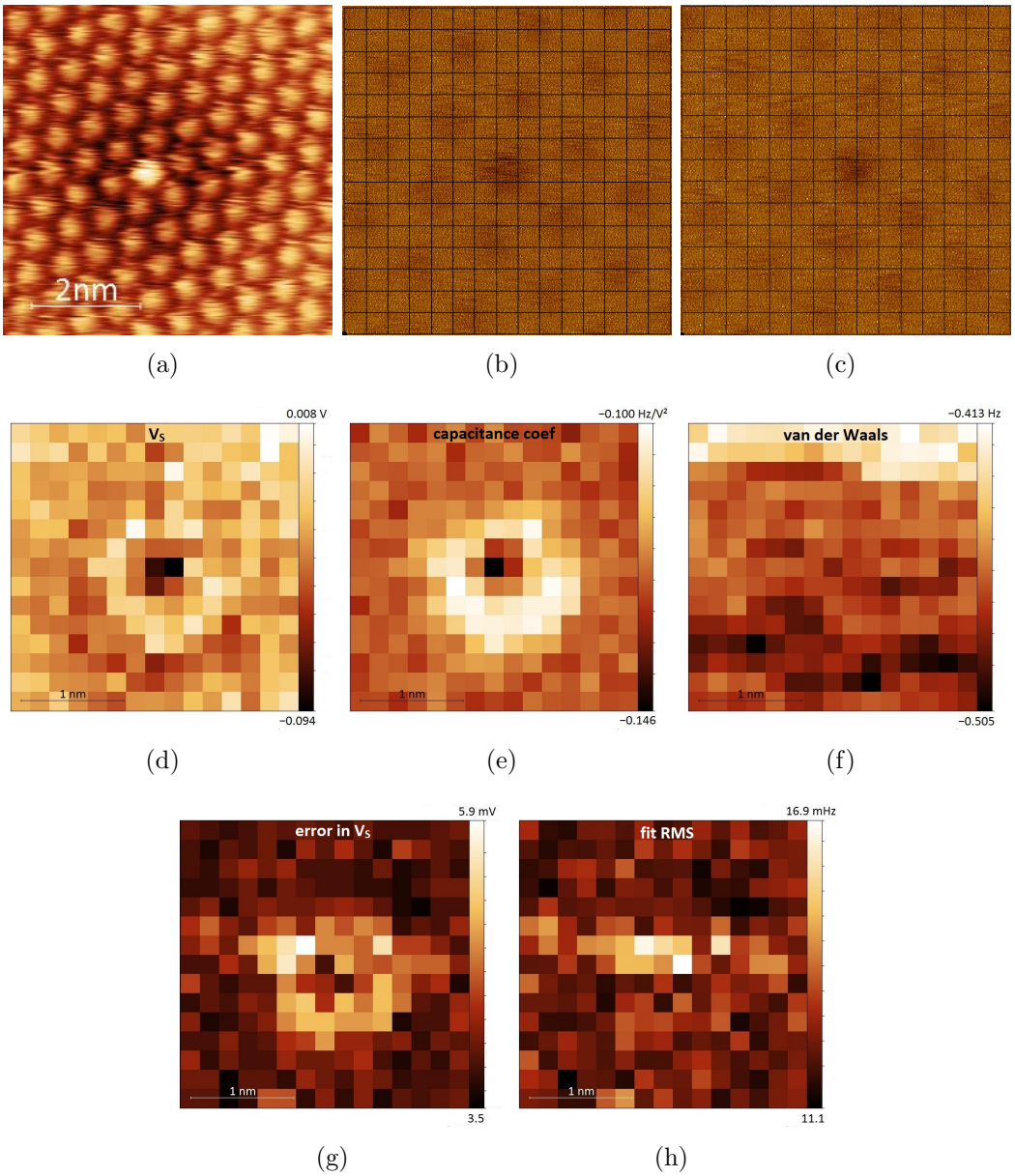

Figure 2.11: Grid spectroscopy measurement on dangling bond using the bias range [-1 V, 1 V] a) STM image prior to AFM imaging(V_{bias}=-0.7 V, I_t=10 pA), constant height Δf images of DB with grid imposed b) before and c) after the grid experiment. Color scale for: AFM images -1.6 Hz $< \Delta f <$ 0.1 Hz, STM image $0 < z <$ 140 pm. Signal maps extracted from Δf(V) spectroscopy of d) surface potential, e) capacitance, f) van der Waals signal, g) incertitude of V_s, h) fit error(RMS). STM and AFM images were done with A_{osc}=50 pm, grid spectroscopy with A_{osc}=100 pm.

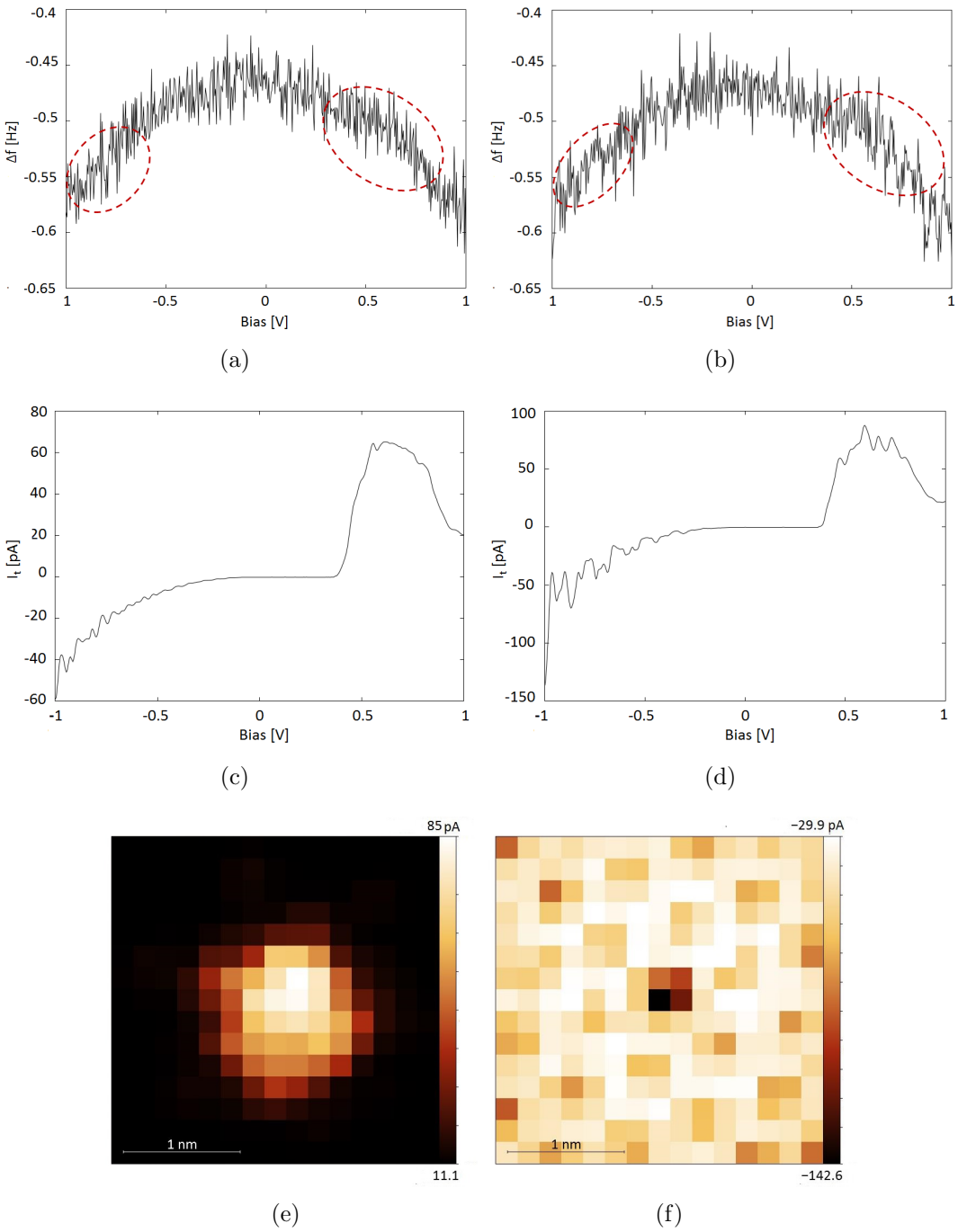

Figure 2.12: The effect of tunnelling current on the frequency shift signal, a),b) Δf(V) spectroscopy with corresponding c), d) I(V) curves. Tunnelling current detected during grid spectroscopy for e) 450 mV and f) -950 mV. The change in the shape of parabola due to the increase of the tunnelling current is indicated with red intermittent line in a) and b).

of Δf(V) curve is noticed, caused by systematic increase of the current passing from the tip to the sample. As a result, fitting a parabolic function to these data leads to artefacts in obtained results and correlation between individual signals of capacitance and charge distribution as observed above. The influence of tunnelling current of frequency shift

signal is studied in the section **2.7.2**.

2.7.1 Corrected grid spectroscopy

In order to correct the grid experiment and eliminate the influence of tunnelling current on frequency signal, the bias range where the fitting is done was reduced to (-0.4 V, 0.4 V) for which the current stayed at lower level (less than 10 pA). As a result, the frequency signal was not perturbed, staying parabolic in the whole bias range. Corrected maps for dangling bond are presented in the Figure **2.13**. In the Figure **2.13(e)** still some noise in

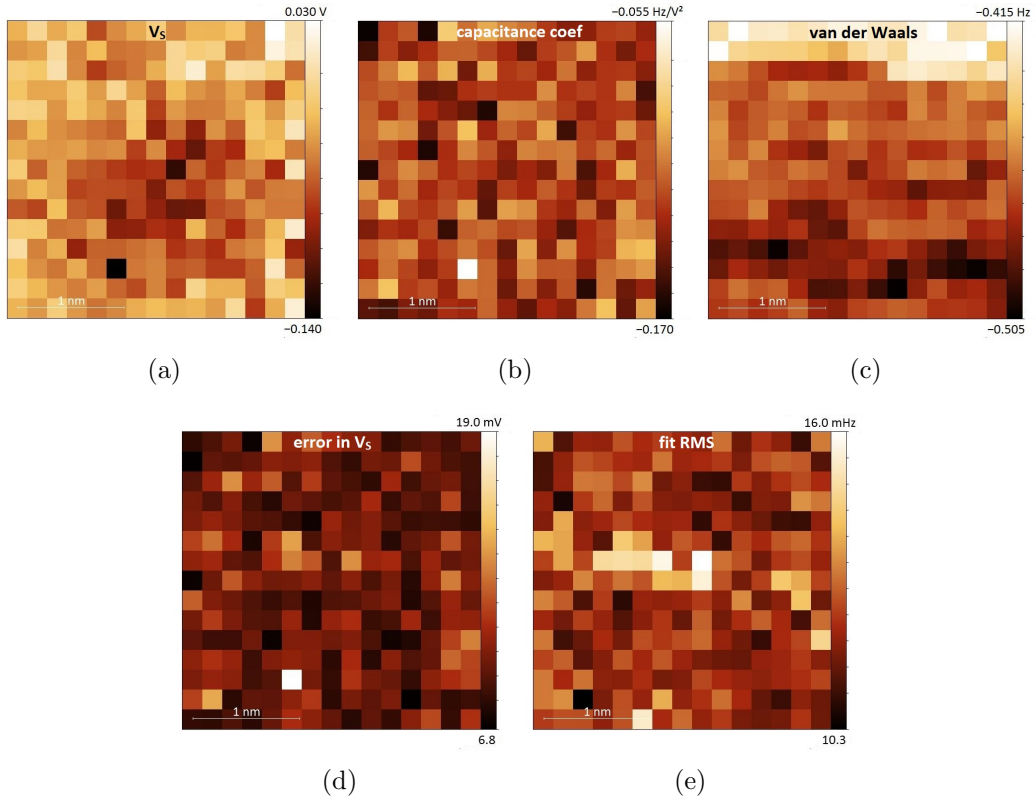

Figure 2.13: Corrected grid spectroscopy on dangling bond, bias range was reduced to (-0.4 V, 0.4 V). Grid maps extracted from Δf(V) spectroscopy of a) surface potential, b) capacitance, c) van der Waals signal, d) incertitude of V_s, e) fit error (RMS). STM and AFM images were done with A_{osc}=50 pm, and the grid spectroscopy with A_{osc}=100 pm (with the tip lifted by 200 pm).

the middle of the image is observed, however the incertitude of V_s is now more uniform. Its larger mean value is caused by reducing the bias range, hence the number of data points used for the fitting. Importantly, no correlation between surface potential and capacitance is observed. Upon the correction of grid, a dark contrast is seen in the middle of surface potential map which corresponds to the detection of a positive charge state for the DB, similary to the results presented previously by Spadafora *et al.*[62] . The contrast is slightly elongated in the horizontal direction of the grid, caused by a drift during the

measurement(≈ 100 pm). We find an average -85 mV ± 10 mV of a difference in V_s between DB and normal silicon adatoms. Regarding the capacitance, the signal stays constant throughout the map which indicates no detectable capacitive difference between the charged adatom DB and the passivated silicon adatoms.

2.7.2 Charging vs phantom force effect

In the previous studies of DB defect, it has been shown that it is possible to change the charge state of non passivated silicon atom through dI/dV spectroscopy[59, 60, 61]. Non parabolic behaviour of Δf presented here could be explained by the transfer of electron from the tip to the dangling bond atom. In the Δf(V) spectroscopy such transition would be revealed by a shift of the parabolic function [21, 72] towards positive sample bias. From the DB grid experiment different spectroscopy curves have been extracted and further analysed (Figure **2.14**).

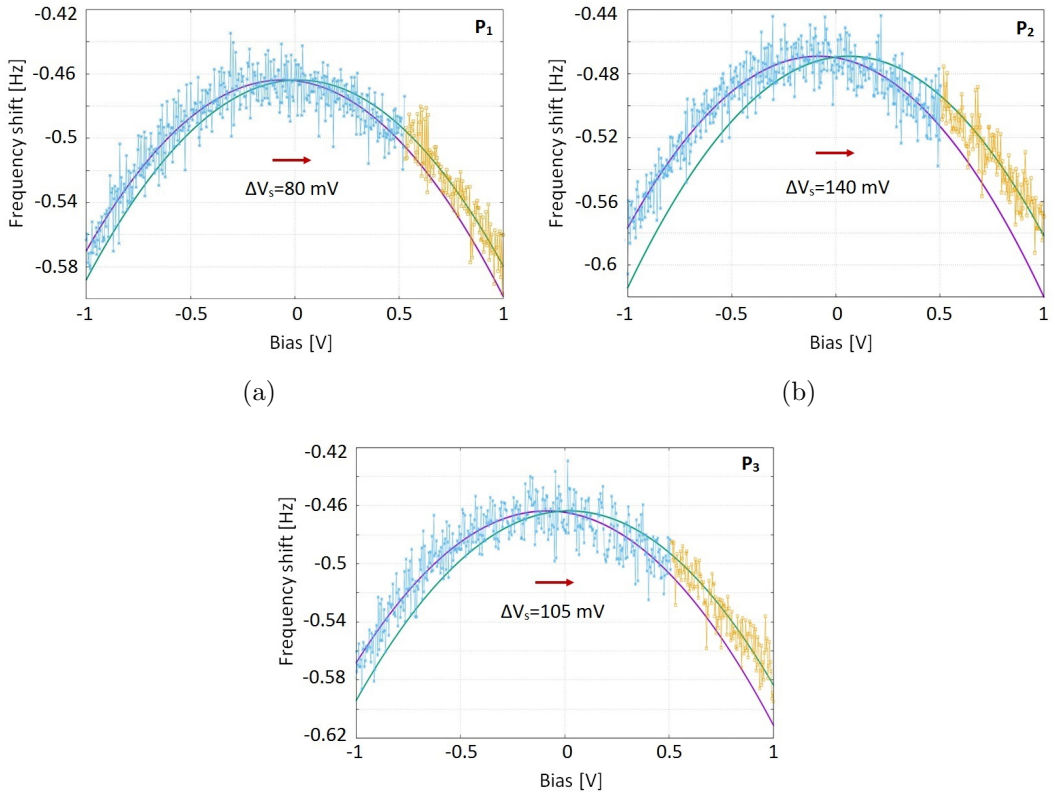

Figure 2.14: Spectroscopy curves extracted from three grid points P_1, P_2 and P_3, showing possible charge transfer between the tip and DB atom at ≈ 0.5 V. Positive DB state is indicated with blue experimental points (fitted with violet curve), the neutral DB state after charging indicated with yellow data points (fitted with green curve).

In each graph, the Δf signal has parabolic character until ≈ 0.5 V, where a small jump

is observed, the other experimental points are shifted upwards, towards less negative Δf values. Fitting another parabola to these points resulted in the function shift towards more positive value of V_s compared to the first parabola, which is in accordance with negative charging of DB atom. The values of V_s shift found from the analysis are 80 - 140 mV ± 10 mV which is the same order of magnitude of single charge detected in the DB grid.

Another possible explanation of non-parabolicity of frequency shift curves could be "phantom force" effect which is related to the change of Δf signal while detecting the tunnelling current at the same time. Phantom force has been studied previously on silicon surfaces with low and high doping level [63, 64]. The tunnelling current passing through a sample leads to local voltage drop and therefore causes the detection of additional electrostatic force, which is proportional to the resistance of the sample and the current, the measured signal is described with:

$$\Delta f = A + B(V_{bias} - V_S - R_s I_t)^2 \tag{2.1}$$

where R_s is the resistance of the sample. The coefficients A, B represent the vdW and capacitance signals and have been described in the section **2.3**. In the Δf(V) curves, an additional positive frequency shift signal is observed for both negative and positive sample bias if the tunnelling current is passed during the measurement. To account for the possibility that phantom forces may explain the non-linearities of Δf(V) spectroscopies over dangling bonds, Δf signal was fitted by the parabolic function however by adding additional term $\propto R_s I_t(V)$. The results for the same three spectroscopy points are presented in the Figure **2.15**. In the plots it can be seen that the parabola deflects at around 0.5 V where the tunnelling current through DB occurs. For each Δf(V) curve the sample resistance of 10 MΩ was incorporated in order to reproduce at best the experimental data points. In the work of Weymouth *et al.* [63] the obtained sample resistance R_s=164 MΩ, however investigated Si(111) sample was low-doped with higher resistivity of 6-9 Ωcm, which can explain much lower value of sample resistance found here.

Another process related also to the tunnelling current is a parasitic coupling between Δf and I_t, observed for the quartz sensors [73]. Here the principle is that the oscillating tip radiates the electromagnetic field which is then coupled by the motion of the sensor by inverse piezoelectric effect. This effect would be also proportional to the value of the tunnelling current.

Comparison of different hypothesis discussed in this section it is not enough to conclude which mechanism is responsible for non-parabolic behaviour of spectroscopy curves. Both charge transfer and phantom force effect result in similar behaviours of Δf(V) curves. At

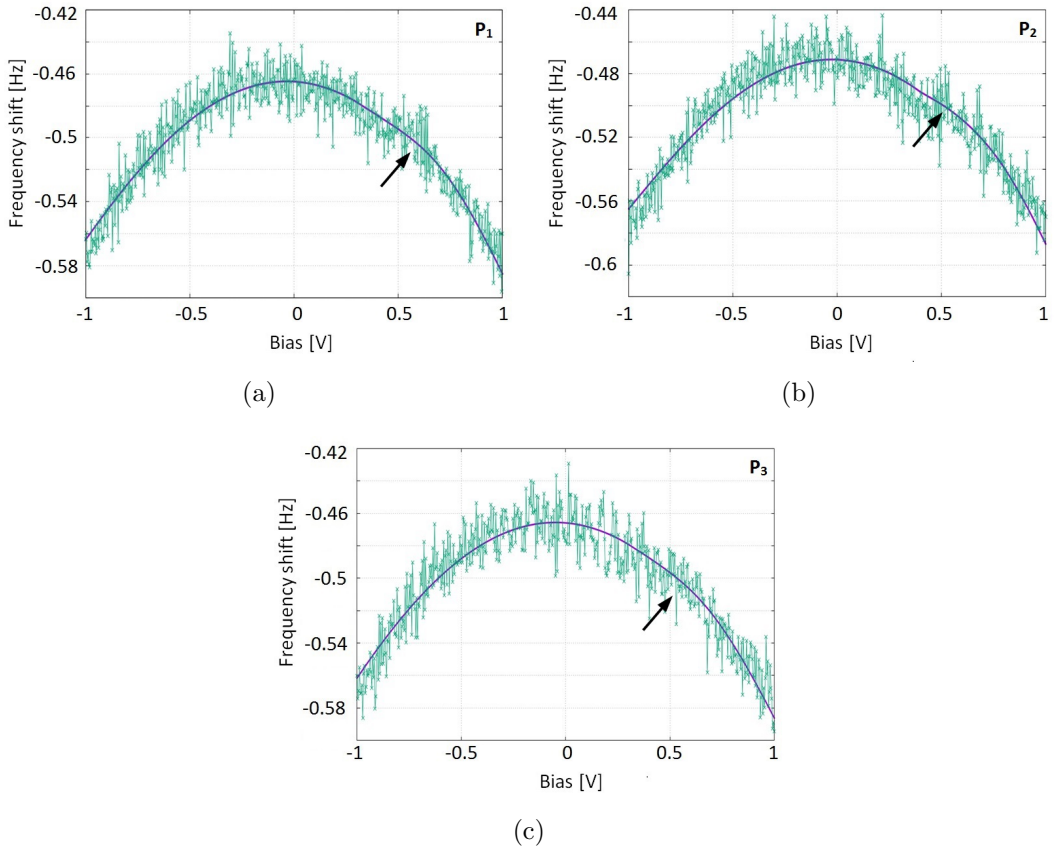

Figure 2.15: Δf(V) spectroscopy for the same grid points P_1, P_2 and P_3 as presented in the Figure **2.14**, the data were fitted with by the function $\Delta f = A + B(V_{bias} - V_S - R_s I_t)^2$ where R_s=10 MΩ. The deflection of the fitted cure is observed at ≈ 0.5 V, where the significant current is passed through dangling bond state (indicated with the arrows).

sample bias of ≈0.5 V the tunnelling current increases significantly and the experimental point are shifted towards less negative values which can be caused either by charge transfer or detection additional signal caused by phantom force effect. The significant noise of frequency shift signal hinders the interpretation of results and needs to be improved in order to distinguish between both effects.

2.8 Comparison of different defects

Figure **2.16** shows the comparison of surface potential maps obtained on buried boron, silicon vacancy and dangling bond. High doping level of silicon crystal results in delocalization of holes and formation of an impurity band. Therefore, the positive surface potential measured on buried boron in the experiment is in accordance with the fact that sub-suface boron dopants are negatively charged. The dangling bond, as it is known from the previous work, can have three charge states:

- positively charged observed for the small bias,
- neutral, when one electron is transferred to DB, observed at $V_{sample} \approx 0.6$ V in the spectroscopy,
- negatively charged, when the saturation of tunnelling current leads to the transfer of second electrons to DB, for $V_{sample} \approx 1.4$ V.

At small bias, the electron of non-passivated dangling bond which state is located in the bandgap, will recombine with the hole from the valance band leaving DB positively charged [61]. This state is observed in the grid experiment presented here, as the negative V_s is detected on the DB atom. In the case of silicon vacancy, no charge was detected. It must be pointed out that by the means of only AFM imaging it was not possible to distinguish whether boron or silicon atom resides under the vacancy. Nevertheless, the analysis of defect in the grid measurement indicates the presence of a silicon atom in the vacancy, as the boron atoms in S_5 site would give a significant surface potential difference compared to other passivated adatoms. The absolute value of surface potential measured for DB defect is much higher than for a buried dopant, as it is located in deeper subsurface layers. Furthermore, the lateral extent of V_S is much smaller for the point defect like dangling bond ($\approx$ 2 nm), compared to buried dopant ($\approx$ 3 nm).

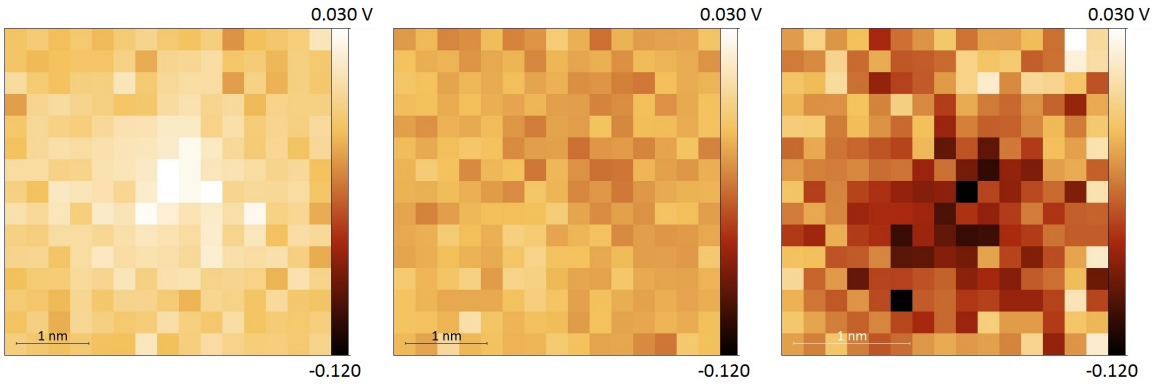

Figure 2.16: Comparison of surface potential maps for a) boron dopant, b) silicon vacancy and c) dangling bond.

2.9 Conclusions

Spectroscopy measurements presented in this chapter showed the possibility of single charge detection using Kolibri sensor. Different types surface defects have been identified

using STM and nc-AFM techniques and studied with Δf(V) spectroscopy in the context of charge detection. From the grid experiments three different charge states have been detected: neutral state for the silicon vacancy, negative charge state for buried boron dopant and positive charge for DB defect. These charge states are accordingly to the theory and previous STM studies presented on Si:B surface. The negative charge observed for buried dopant yielded $\approx$ 35 mV in the surface potential map which is significantly less than the value measured on DB defect due to the location of the dopant deeper under the surface plane. In the analysis of dangling bond, non parabolic behaviour of Δf(V) was observed at sample bias of $\approx$ 0.5 V that can stem from two phenomenas - either charge transfer from the tip to Si atoms or phantom force effect, related to the tunnelling current passing through the sample. Despite the fact that it is not possible to clearly distinguish which mechanism dominates, the care must be taken in the analysis in order to avoid artefacts. The negative potential map obtained for DB defects with $\approx$ -85 mV indicates that the dangling bond is found in the positive charge state and determines the reference potential value for a single surface charge.

Chapter 3

nc-AFM and KPFM study of CDB and CDB-I molecules on Si:B

The main objective of this chapter is the verification of the resolution and sensitivity of Kolibri sensor in topography and electrical imaging of a single molecule deposited on semiconductor surface. From Δf images obtained in constant height mode we observe submolecular resolution, achieved without intentional tip functionalization. The details of aliphatic chains and three phenyls of the probed molecules are identified in nc-AFM images. The features of molecule structure observed in Δf are affirmed by comparing images with simulation. Moreover, an asymmetry in the length of two side phenyl groups is systematically observed between different CDB-I molecules. In the second part of the chapter, KPFM measurements are presented on both CDB-I and CDB molecules. Two different types of contrast are observed in surface potential maps, showing that part of molecules can be charged either negatively or positively. We associate this difference with different adsorption sites and possible charge transfer from the molecule to substrate when the molecule is adsorbed on a surface defect.

3.1 A brief overview of high resolution imaging of single molecules

The first important work presenting ultra high resolution in nc-AFM on molecules was realized by the IBM group in 2009 [9], in which the chemical structure of individual pentacene molecules deposited on Cu(111) was resolved, using a metallic AFM tip terminated with a single carbon monoxide (CO) molecule. In this work it has been shown that the crucial factor in obtaining high resolution is the process of controlled tip functionalization. The decoration of the tip apex with single CO molecule results in an increased resolution

in both STM and AFM, such that the five hexagon carbon rings and C-H bonds of pentacene are visible in constant height Δf images (shown in Figure **3.1**). The intramolecular resolution was also achieved on thin film insulating surface of NaCl(2ML)/Cu(111) with various tip functionalizations of CO, Ag, Cl and pentacene [9]. The dependence of Δf contrast on tip-sample distance was explored and showed the importance of repulsive forces detection in obtaining submolecular resolution. Since then, a large number of different

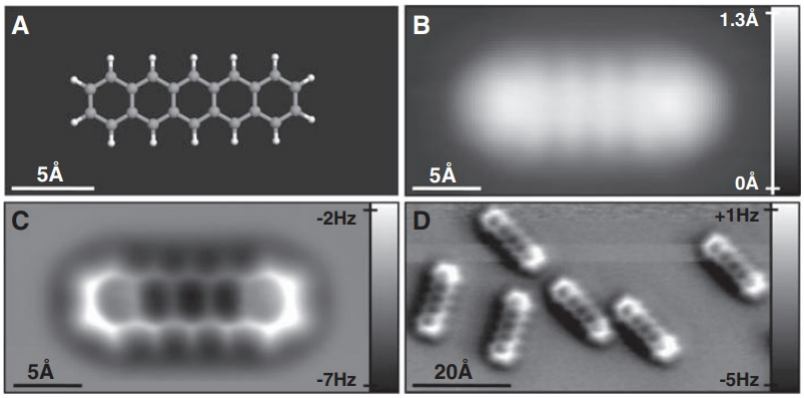

Figure 3.1: Chemical structure of pentacene on Cu(111) resolved in constant height AFM images. The model of pentacene molecule with five carbon rings shown in a), b) STM (I_t=170 pA, V_{bias}=170 mV) and c),d) AFM images of a molecule using CO terminated tip with oscillation amplitude of 20 pm and 80 pm in c) and d) respectively. Adapted from [9]

(essentially flat) molecules have been resolved with CO tip on metallic and passivated surfaces with NaCl [74, 75, 76]. Different tip functionalizations were also tested including Xe [16, 15, 77], copper oxide CuO [12, 17] and nitrous oxide N_2O [18]. Nevertheless, not many works have been demonstrated on semiconductors. One study has been achieved by Sweetman *et al.*[19] in which a single molecule deposited on highly reactive silicon surface was imaged. Figure **3.2** presents STM and AFM image where the chemical structure of the NTCDI molecule was resolved at 78 K. What is important, this high resolution was obtained without intentional tip functionalization, only by conditioning the tip on the silicon surface. From the comparison of experimental Δf(z) curves with simulations it is possible to determine which tip termination is responsible for creating the high resolution. The most probable candidate for the image shown in **3.2b** is NTCDI molecule adsorbed at the tip with oxygen atom pointing towards the surface. Nevertheless, it is also possible that silicon dimer at tip apex would produce the same Δf contrast [19].

Except for high resolution imaging of molecules structure, thanks to nc-AFM the distribution of contact potential difference was obtained on the submolecular scale, using Δf(V) spectroscopy [22]. The Figure **3.3** shows STM, AFM and KPFM images of naphthalocyanine molecule adsorbed on NaCl(2ML)/Cu(111) surface. The LCPD value was extracted from the maximum of Δf(V) parabola in each point of the grid for metallic

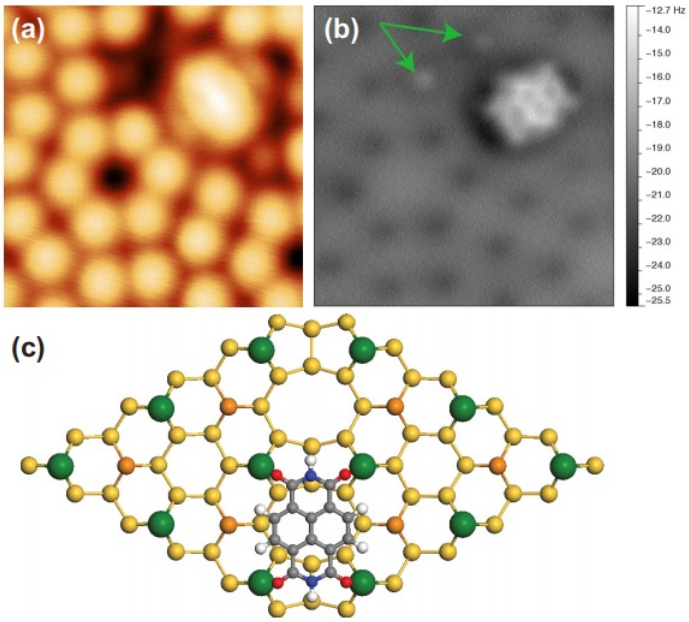

Figure 3.2: NTCDI molecule on Si(111) 7x7 surface at 78 K, a) STM (I_t=40 pA, V_{bias}=1.5 V), b) constant height Δf image, A_{osc}=0.28 nm, c) model of molecule adsorption on the silicon surface. Green arrows indicate the positions of two passivated silicon atoms. Size of images a), b) 3.8 nm x 3.8 nm. The image extracted from [19]

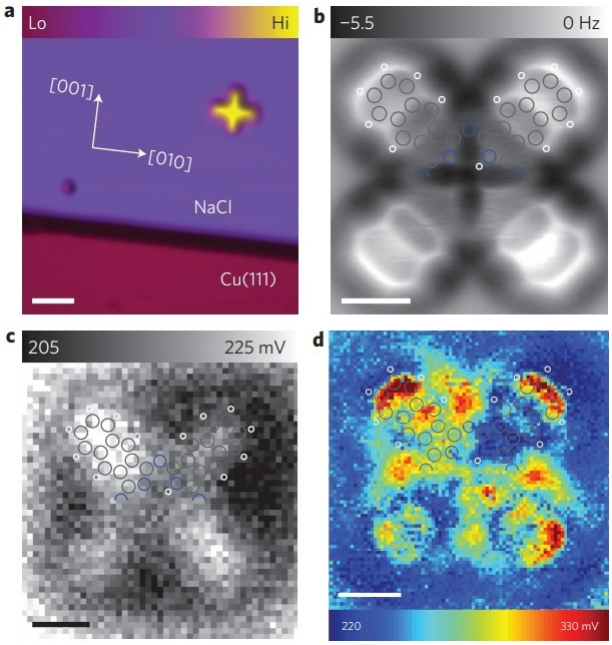

Figure 3.3: a) STM image (I_t=2 pA, V_{bias}=0.25 V) of naphthalocyanine molecule adsorbed on NaCl film on Cu(111), b) constant height Δf image with chemical structure resolved, image was taken with CO functionalized tip. KPFM maps of LCPD of the molecule obtained with metallic (after tip indentation in the copper surface) and CO tip are shown in c) and d) respectively. Scale bars: 2 nm in a) and 0.5 nm in b)-d). Images extracted from [22]

and CO tip, presented in **3.3c**, **3.3d** respectively. From the comparison of both images it is evident that the functionalization process leads to an enhanced resolution also in KPFM measurements. Additional DFT simulations affirm that the contrast observed in the KPFM images reflects the charge distribution within a single molecule.

3.2 Presentation of molecules used in this work

The two molecules studied here are organic molecules containing three benzene rings and aliphatic chains. The first molecule is 1-(4'cyanophenyl)-2,5- bis(decyloxy)-4-(4'-iodophenyl)benzene, named in this manuscript as CDB-I. This molecule is made of two aliphatic chains attached to a three-phenyl core ended with two different terminations. The design of the molecule (length of the aliphatic chains or phenyl chain) has been made in order to generate self-assemblies on Si:B [78] as studied in Chapter **4**. In the CDB-I molecule, the first termination of the phenyl chain is cyano group, known to be a strong electron withdrawing group; the second termination is an atom of iodine, acting as an

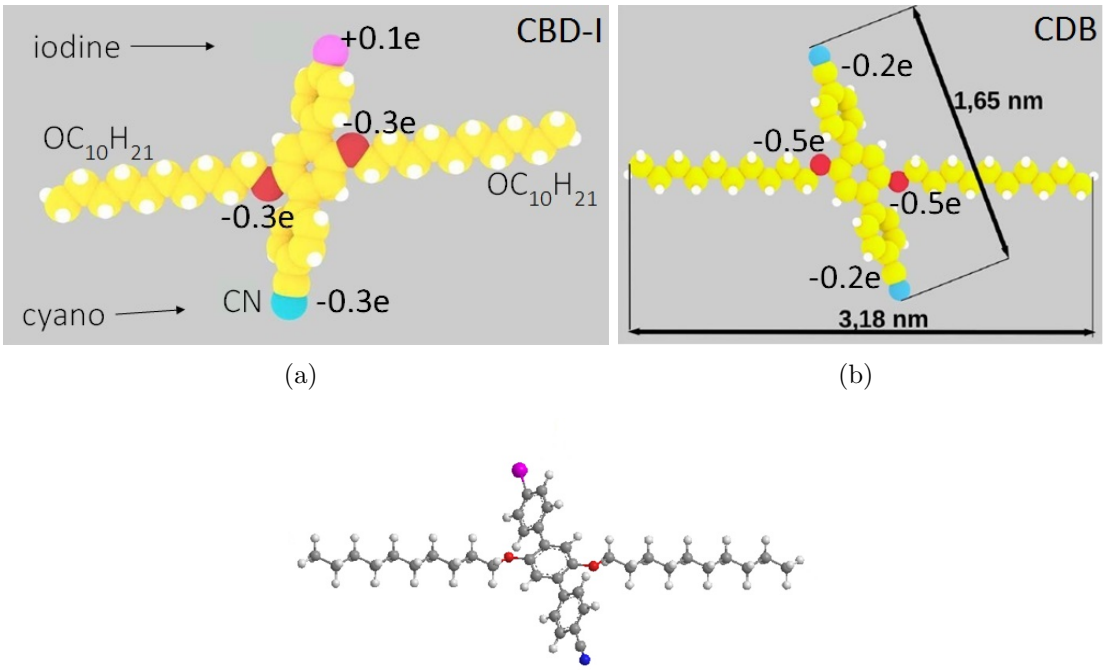

(a) (b)

(c)

Figure 3.4: The structure of a) CDB-I with two aliphatic chains $C_{10}H_{21}$ and three-phenyl core, the different terminations of the molecule are indicated: nitrogen atom of cyano group (blue) and iodine atom (pink). The charge distribution was obtained for a molecule in vacuum from DFT calculations. b) CDB with two identical cyano terminations, the distance between the extremities of aliphatic chains is 3.18 nm, the separation between two nitrogen atoms of cyano groups is 1.65 nm. The structure of CDB-I after minimization of energy (using PM3 method) for a molecule in vacuum presented in c). The images in a) and b) are extracted from [79].

electron donor. Due to the difference in electronegativity of both terminations, a dipole of 3.6 Debye is formed along the phenyl core of the molecule. The second molecule is 1,4 bis(4'cyanophenyl)-2,5bis(decyloxy)benzene, labelled as CDB. This molecule resembles CDB-I, however it is ended with two identical terminations of cyano groups and therefore exhibits no dipole along the phenyl chain. Previously, the CDB molecule was also studied on ionic alkali halide surfaces on which it formed highly-organised molecular networks [80, 81]. The distance between the extremities of aliphatic chains for each molecule is 3.18 nm. Structures of CDB-I and CDB molecule together with dimensions are shown in the Figures **3.4(a)** and **3.4(b)**. The charge distribution for both molecules in the vacuum was obtained from DFT calculations done by Christophe Krzeminski (IEMN). The model of the molecule in vacuum after minimization of energy (PM3 method), as done by David Guérin, is presented in **3.4(c)**. The tilt of two side phenyls with respect to the central phenyl is observed, caused by steric effects related to the hydrogen atoms of each of the phenyl groups. The same tilting of the side phenyls is also observed in the case of CDB molecule.

3.3 Structure of molecule resolved with nc-AFM

In this section, single molecule AFM measurements are presented showing the highest resolution obtained without intentional tip functionalization. The deposition of molecules presented here was effectuated at low temperature, that is, the sample was taken out directly from the microscope and was not thermalized back to 300 K during the molecule deposition. This type of deposition resulted in the formation of small ordered domains, but also many individual molecules have been found in the vicinity of surface defects. A STM image showing the molecules organisation is presented in the Figure **3.5**. One of the single molecules has been chosen for AFM imaging. The constant height Δf image and a possible orientation of the corresponding molecule are presented in **3.6(a)**, **3.6(c)**. Despite a slight double tip (as seen in **3.6(b)**), the submolecular details are observed in the AFM image. First of all, we observe the details of aliphatic chains in the form of five protrusions. Knowing that each aliphatic chain contains ten carbon atoms arranged in a zigzag form, we associate these protrusions with either five topmost carbon atoms along the chain or C-H groups pointing out perpendicular from the surface plane. Moreover, the distances measured between the protrusions - from 260 pm to 275 pm $\pm$10 pm - are close to the distance value between two carbon atoms - 250pm - represented in the model in **3.6(d)**. Small differences can be caused by the tilting of the chain on the surface. Furthermore the bottom aliphatic chain is bended at the end at 120° which corresponds to the directions of substrate silicon rows.

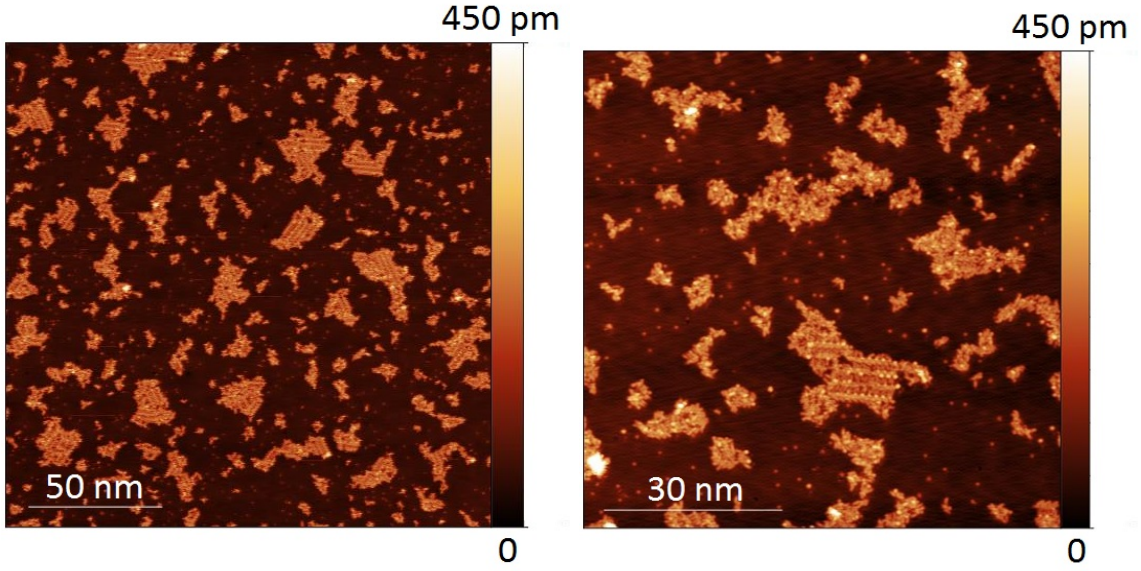

(a) (b)

Figure 3.5: a), b) STM images of molecules organisation after LT deposition. The formation of small molecular islands is seen, as well as many individual molecules found close to Si(111):B defects. Images have been taken with A_{osc}=50 pm, V_{bias}=-1.9 V, I_t=5 pA.

Secondly, for the aromatic core of the molecule three phenyls can be distinguished. The central phenyl, is orientated flat on the surface and therefore gives dark contrast in Δf image. Two side phenyls have much higher Δf signal due to their tilting on the surface. Furthermore, the cross section through the core shows an asymmetry in length between two side phenyl groups of 120 pm $\pm$20 pm, as shown in the Figure **3.6(e)**. It is likely at this stage, that the length difference stems from the sole comparison of the length of the signals associated with phenyl ring terminations in Δf images **3.6(c)**. On the one hand, the cyano group termination is longer than iodine termination which could indicate that it corresponds to the phenyl group with greater length observed in Δf image. On the other hand, the atom of iodine is bigger than atoms of carbon and nitrogen and could give higher Δf contrast than cyano (and therefore apparent as a longer termination) when passing at the constant height during AFM imaging. At this point it is not possible to distinguish between both terminations and KPFM measurements will need to be done to verify if the longer termination corresponds to cyano or iodine. The comparison of cross sections for both CDB-I and CDB molecules will be presented for the assemblies in the section **4.8** of the next Chapter.

Another single molecule CDB-I imaged with AFM is presented in the Figure **3.7**. During the measurement a small negative bias (-390 mV) was applied on the sample which allowed measuring the tunnelling current at the same time with Δf signal. The contrast on silicon adatoms shown in **3.7(c)** served for finding the adsorption site of molecule on

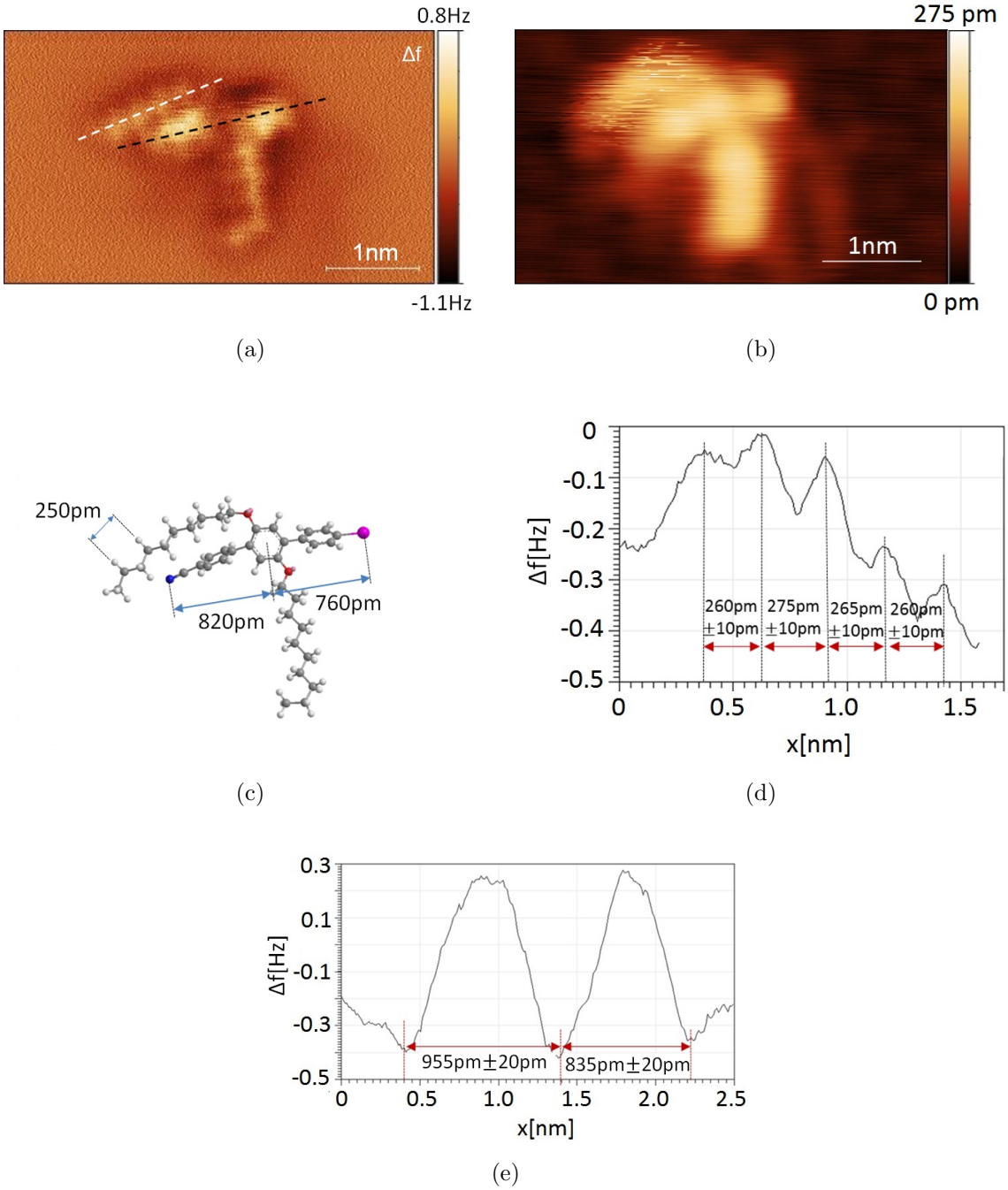

Figure 3.6: a) Δf image of a single CDB-I molecule, A_{osc}=50 pm, V_{bias}=0 V, b) STM image of the molecule (A_{osc}=50 pm, V_{bias}=-1.9 V, I_t=5 pA), c) molecule configuration reproducing possible orientation of molecule corresponding to AFM image, d) cross section of the aliphatic chain with distances between the protrusions, corresponding to the white intermittent line in a), e) cross section of the aromatic core of the molecule showing the asymmetry between both terminations, corresponding to the black intermittent line.

the substrate. The positions of Si atoms are indicated with white dotted intermittent line in **3.7(d)**. It is observed, that aliphatic chains (whether straight or bended) always follow the substrate and place themselves between the rows of silicon atoms. Therefore,

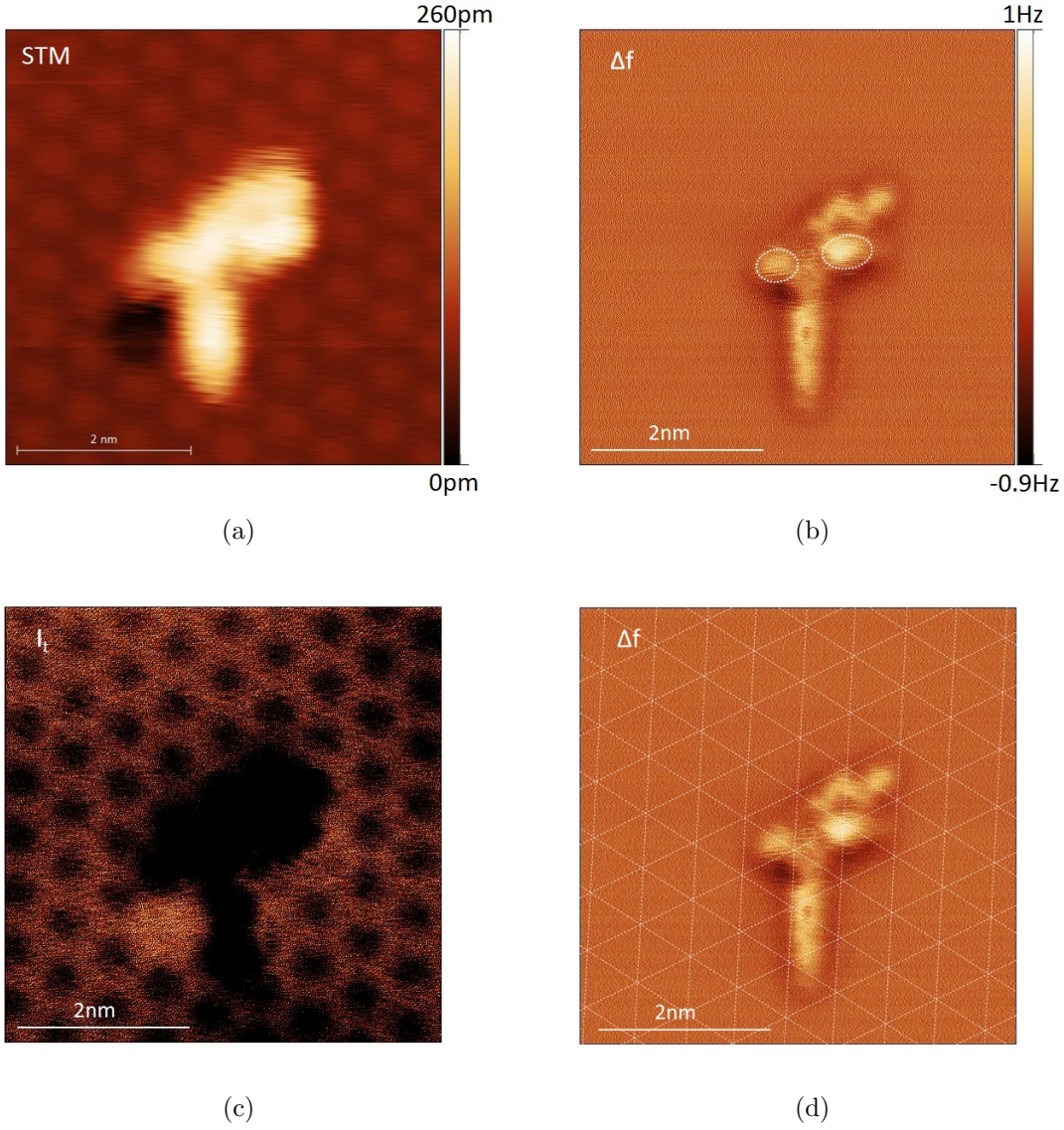

Figure 3.7: a) STM image of the CDB-I molecule located near surface defect (V_{bias}=-1.8 V, I_t=5 pA, A_{osc}=50 pm,) and b) corresponding constant height Δf image (V_{bias}=-390 mV, A_{osc}=50 pm,). Tunnelling current channel extracted from the AFM measurement is presented in c), the contrast on silicon atoms was then used and superimposed on Δf image shown in d). Two side phenyls groups are indicated with white dotted line in the image b).

it indicates an important interaction between the substrate and the molecule. The same behaviour was systematically observed for several molecules found isolated on the surface. Again, the asymmetry between two side phenyl groups are observed for these molecules as well.

3.4 KPFM of a single molecule

KPFM measurements of single molecules presented in this section have been achieved in the same manner as measurements of surface defects described in the section **2.3**. Prior to spectroscopy, the tip was retracted by 100-300 pm and the oscillation amplitude was increased to 100 pm. Depending on the measurement, in each grid point 4-6 spectroscopies were done. In order to reduce the Δf noise, the average curve of all spectroscopy curves for forward and backward sweeps was then analysed.

The grid measurement of 33 x 31 points and 2.5 nm x 2.4 nm size of CDB-I molecule is presented in the Figure **3.8**. The tip was retracted by 100 pm before the grid and the time of measurement was 9h. From comparison of the AFM image before and after the grid, we measured the lateral drift of $\approx$ 500 pm. Despite this, it is possible to clearly identify the structure of the molecule in the reconstructed $\Delta f(V_s)$ signal map, as seen in **3.8(c)**). This signal contains a van der Waals contribution but also short range repulsion where the signal becomes positive. The contrast obtained resembles the one in Δf images, with darker contrast on the central phenyl and higher signal on two side phenyls. In the surface potential map of molecule (presented in **3.8(e)**), a more positive V_s signal is detected on the molecule compared to silicon substrate. A slightly more negative signal is observed in the "capacitance" image for the three phenyl core in **3.8(d)**, which is caused by increased capacitance due to the molecule height when moving the tip at the constant height above the surface plane. The error in fit (RMS) is rather homogeneous with average value of 12 mHz as presented in **3.8(f)**. The variation of surface potential above the molecule was further analysed and shown in the Figure **3.9**. First of all, the surface potential measured on aliphatic chains is smaller than the other part of the molecule. The mean value of 50 mV is found, with respect to the silicon substrate. The signal measured on the molecule core is higher, $\approx$ 130 mV on side phenyls and $\approx$ 220 mV on the central phenyl. Moreover, two brighter features are observed symmetrically on the both sides of central phenyl, having higher V_s value of around 60 mV compared to the central phenyl. We associate these features with two oxygen atoms located at the beginning of each aliphatic chains, that are bearing a negative charge and therefore more positive V_s. The cross section of surface potential through central phenyl is indicated with blue intermittent line and presented in **3.9(c)**. Furthermore, we can distinguish the parts of molecule with negative and positive signals in V_s which is in accordance with a situation without significant net charge transfer between the substrate and the molecule. The cross section of V_s done for the core of the molecule, presented in the Figure **3.9(d)**, shows the asymmetry in the surface potential of 100 mV between both terminations. The distance between the maximum of V_s signal at first extremity and minimum at the opposite one is 1.6 nm.

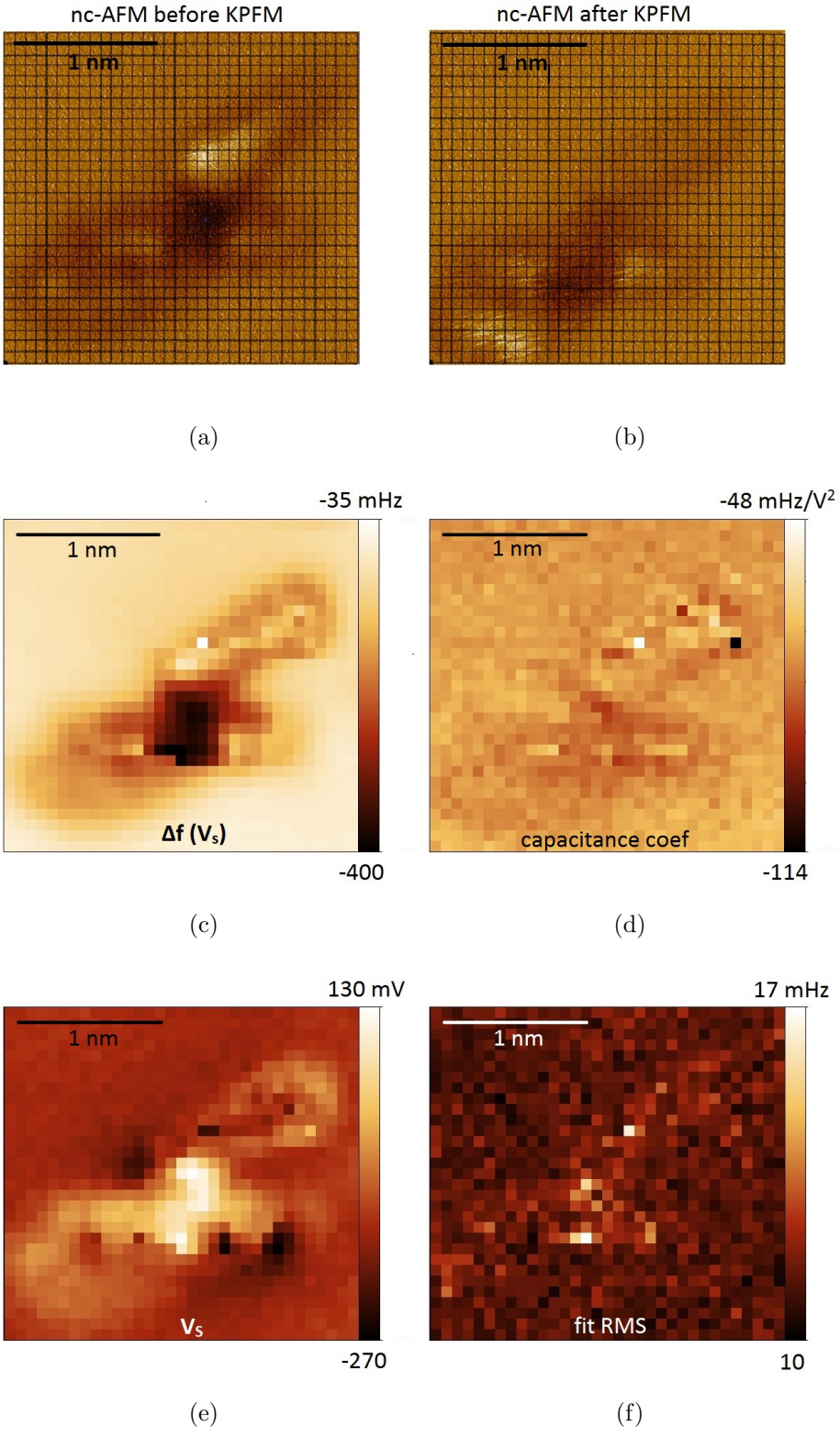

Figure 3.8: KPFM grid measurement of CDB-I molecule, a) constant height AFM image with grid before and b) after measurement, c) $\Delta f(V_s)$ signal map, d) capacitance coefficient, e) surface potential and f) fit error(RMS). AFM images were done with A_{osc}=50 pm, and the grid spectroscopy with A_{osc}=100 pm (with the tip lifted by 100 pm with respect to AFM imaging conditions). The duration of the grid - 9h.

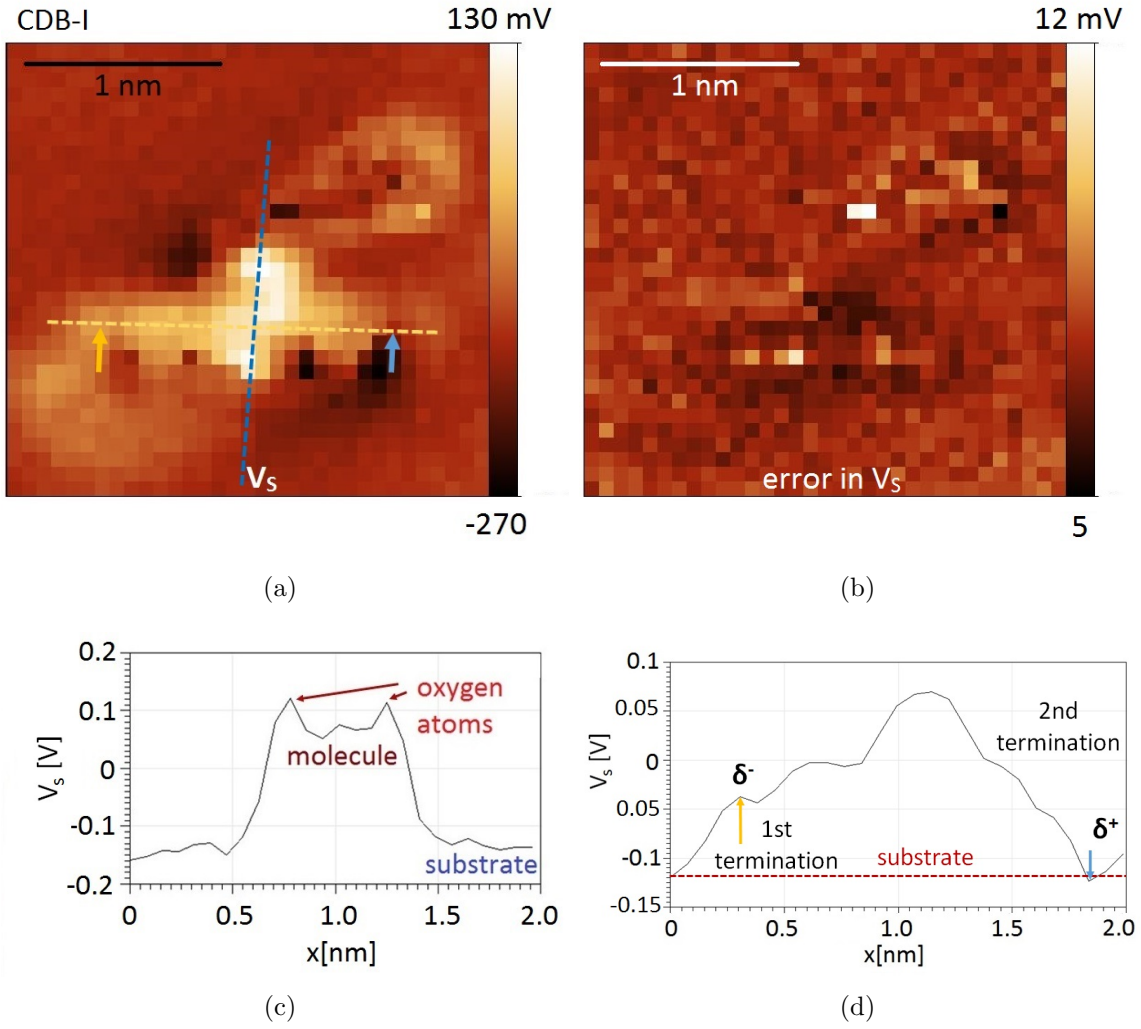

Figure 3.9: a) Surface potential map of CDB-I molecule presented in the Figure **3.8**, b) incertitude in surface potential. Two cross sections of V_s indicated with intermittent lines in the image a) and are presented in c) cross section of the central phenyl with oxygen atoms (blue colour) and d) cross section through three-phenyl core (yellow colour).

The side phenyl group with greater length in Δf image corresponds to the termination of positive V_s, while the shorter one corresponds to negative V_s. For this reason, we attribute the longer termination with positive surface potential (and negative charge) to the cyano group, whereas the shorter termination with slightly negative surface potential (and positive charge) corresponds to the iodine atom.

A similar contrast of surface potential was found on several molecules, KPFM measurements of two other CDB-I molecules are shown in the Figure **3.10**. The aliphatic chains have smaller V_s signal compared to three-phenyl core of each molecule, however the absolute values varies, depending on the molecule investigated. For CDB-I shown in **3.10(a)** surface potential of $\approx$ 120 mV was measured on the molecule core and $\approx$ 50

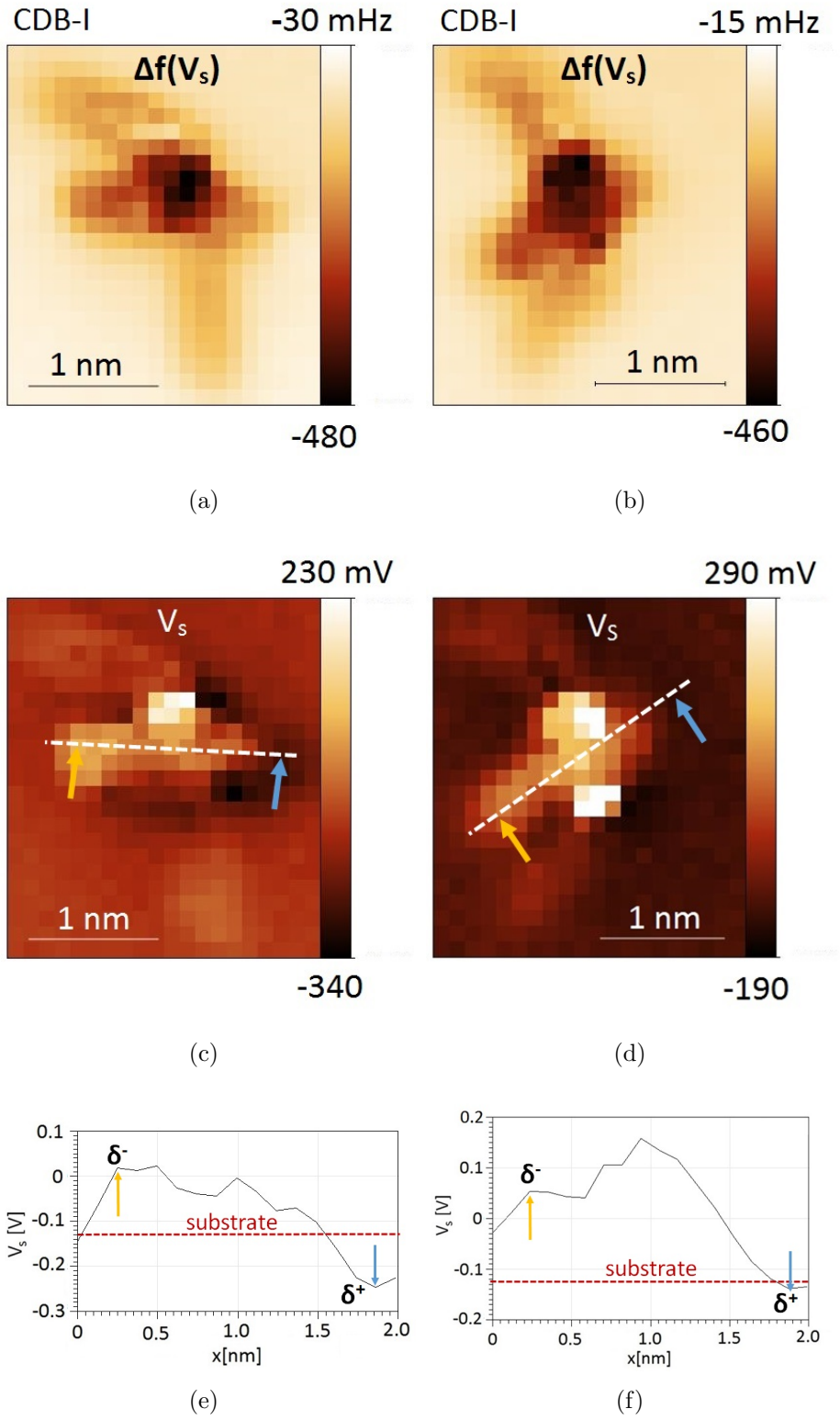

Figure 3.10: Two grid measurements of CDB-I molecules showing the same V_s contrast. a), b) $\Delta f(V_s)$ signal map, c), d) Surface potential and e), f) Cross sections of V_s through the cores of the molecules indicated in c) and d) . The grid spectroscopy was done with A_{osc}=100 pm (with the tip lifted by 100 pm with respect to AFM imaging conditions). The duration of both grids was 4h.

mV on aliphatic chains, with respect to silicon substrate. Comparatively, in the case of **3.10(b)**, V_s of $\approx$ 80 mV and $\approx$ 25 mV was found on the core and chains respectively. Once again, bright features are found on the sides of central phenyl with much higher signal, as seen in **3.10(c)** and **3.10(d)**. The differences in measured values of surface potential may be caused by the different scanning conditions in constant height AFM and therefore, different heights at which KPFM measurement were performed. Moreover, the adsorption and different inclination of each molecule on the surface can contribute to the differences in V_s. For both CDB-I molecules investigated here, the asymmetry in the surface potential is observed between both extremities of the molecule core, as seen in the cross sections in **3.10(e)** and **3.10(f)**. Similarly to the molecule presented in the Figure **3.9**, the positive surface potential is detected for the termination with greater length and negative surface potential for the shorter termination. The difference of 270 mV and 290 mV is measured between the terminations for **3.10(e)** and **3.10(f)** respectively, the corresponding distances between the extremities are 1.6 nm and 1.7 nm. The systematic asymmetry observed in both Δf and V_s images for CDB-I molecule indicates that the longer termination refers to cyano group, while the shorter extremity to iodine atom.

A different type of surface potential contrast was found as well, on both CDB-I and CDB molecules. $\Delta f(V_s)$ signal and KPFM maps are shown in the Figure **3.11**. For both molecules a negative surface potential is measured, which indicates the positive charging of molecules compared to the substrate. The incertitudes in fitting procedure (RMS) are homogeneous and no crosstalk between different signal contributions is observed. The maximum value of V_s for CDB-I was -75 mV, whereas for CDB -60 mV. While in STM measurements it is very often seen that single molecules are located in the close vicinity of surface defects, we will link the negative V_s with the electron transfer from the molecule to the surface when it is adsorbed on the defect. In the case of CDB-I molecule (**3.11(a)-3.11(c)**) the spectroscopy was done for the bias range (-950 mV, 600mV), thus we decided to verify if any tunnelling current is measured during the grid at 0.6 V, which would correspond to DB state. Eventually, no current was detected in the whole image, which suggests, that after adsorption of molecule on the defects, the DB becomes passivated and its state is no longer visible in the band gap.

3.5 Conclusions

The nc-AFM measurements presented in this chapter proved the possibility of obtaining submolecular resolution without intentional functionalization of the tip. In the Δf image of CDB-I molecule the structure is identified, with three-phenyl aromatic core and details of aliphatic chains in the form of bright protrusions. The central phenyl is always

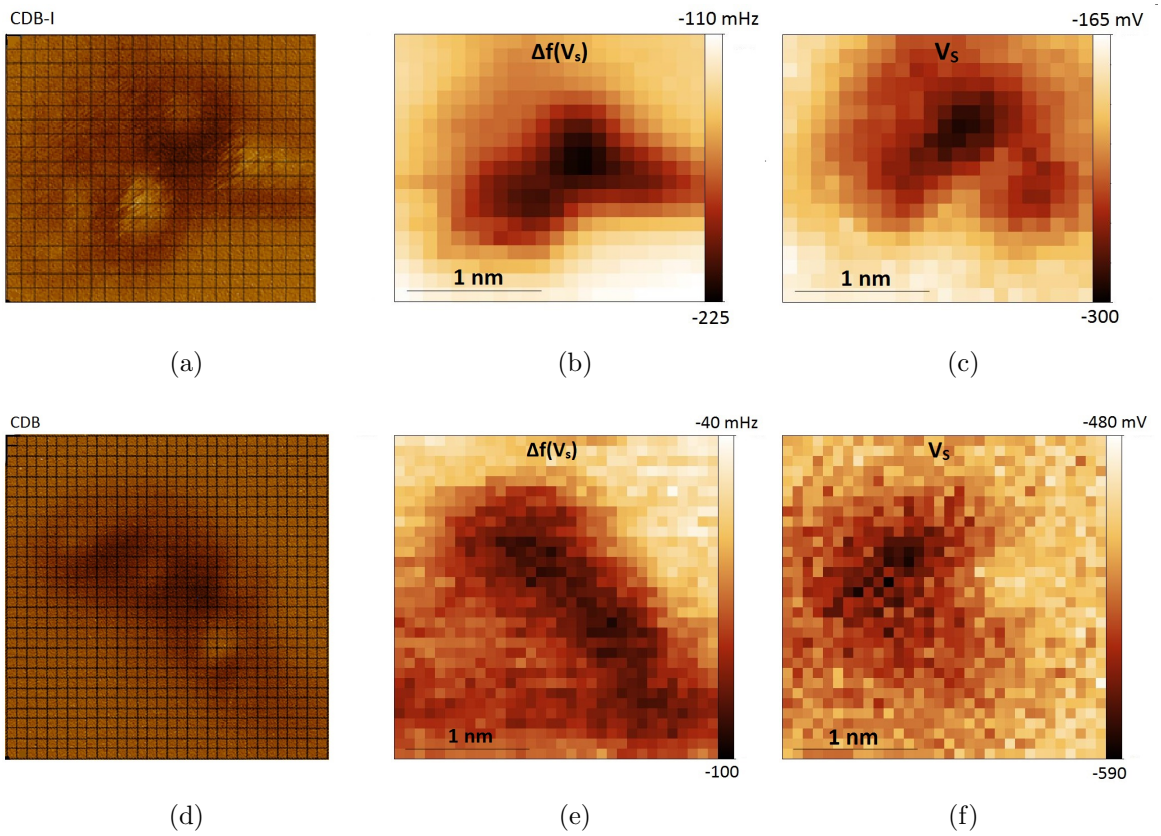

Figure 3.11: a), d) AFM images with grid indicated before the spectroscopy, b), e) $\Delta f(V_s)$ signal map and c), f) surface potential for CDB-I and CDB respectively. Constant height Δf images for both grids were done with A_{osc}=50 pm, and the grid spectroscopy with A_{osc}=100 pm (with the tip lifted by 200 pm for CDB-I and 300 pm for CDB with respect to AFM imaging conditions). The duration of the grid was 6h for a)-c) and 9h for d)-f).

oriented flat, where two side phenyls are tilted on the silicon surface, in accordance to the simulated model of the molecule. Moreover, the asymmetry in length of two side phenyl groups is observed, possibly due to the difference in molecule terminations. Furthermore, the aliphatic chain orientation is not aleatory and always follows the directions of silicon rows. Regarding KPFM measurements, we distinguish two different adsorption types of molecule on the surface. In the first one, the variation of positive surface potential is detected on the molecule core and aliphatic chains, but also the oxygen atoms (charged negatively) give prominent contrast in the surface potential maps for both CDB-I and CDB molecule. In the second adsorption type, the observed KPFM contrast is dark (corresponding to a positive charge) and not well resolved. We tentatively assign this negative contrast to the charge transfer of electron from the molecule to the dangling bond underneath and therefore positive charging of the molecule.

Chapter 4

Comparison of CDB-I and CDB self-assemblies studied with nc-AFM and KPFM

4.1 Introduction

In the previous STM studies it has been shown, that organic molecules with long aliphatic chains can form self-asemblies due to the van der Waals interactions that arise between aliphatic chains of neighbouring molecules, known as chain interdigitation. The first objective of this chapter is the high resolution imaging of the assemblies with non contact AFM, which will provide more detailed information about the topology of the sample as compared to the STM technique. From these measurements the orientation of molecules in the assemblies is obtained as well as their position with respect to the silicon substrate atoms. In the case of CDB-I molecules, which exhibit a dipole along the chain of phenyl rings, the open question is whether the self-assembly is dipolar or not. It is expected that nc-AFM - which reveals in the asymmetry of individual CDB-I molecules as presented in Chapter **3** - is a suitable tool to evidence for the dipolar character (or not) of such assemblies. The dipolar character of the assemblies can also be verified from KPFM measurements, which give information about the charge distributions in molecules and help in identifications of the different molecule terminations.

4.2 Previous STM/AFM studies of molecular assemblies

We present here a short review of previous studies of molecular assemblies by means by Scanning Probe Microscopy. The first study revealing intra-molecular contrast of molecular assemblies was presented by Weiss *et al.* [82] where PTCDA assembly on Au(111) was imaged using scanning tunnelling hydrogen microscopy (STHM). In this work, the submolecular resolution of molecules structure and apparent contrast between molecules was observed, which was assigned to imaging noncovalent bonds. Afterwards, molecular assemblies were studied with nc-AFM using functionalized tips with CO molecules. In the work of Zhang *et al.* [10] the sharp contrast between 8-hydroxyquinoline (8-hq) molecules was also observed in Δf images. These features were associated with hydrogen bonding between individual molecules however the mechanism of the contrast formation remained unknown. Similar intramolecular contrast was also observed on passivated surface of Ag:Si(111) [83] for NTCDI assembly. The interpretation of the intramolecular contrast was done by Hapala *et al.* [11] who demonstrated that the tip relaxation is responsible for creating sharp edges between molecules. The mechanism includes the flexible tip termination which relaxes away from the regions of strong Pauli repulsion created by the proximity of atoms and not increased electron density corresponding to the presence of intermolecular bonds.

Mapping the electrostatic potential provides a further information about the position and orientation of molecules in assemblies in addition to nc-AFM topography. The surface potential distribution was previously indirectly obtained on PTCDA assemblies on Ag(111) surface with Kolibri at 1.2 K [14], by scanning with two differently charged Xe tips (neutral and positively charged Xe atom). The electrostatic potential was calculated then from the deformation field obtained from two different Δf images. KPFM measurements consisting in Δf(V) spectroscopy were done of FFPB assembly on Au(110) surface with Au terminated qPlus sensor [84]. LCPD with Δf topography and tunnelling current images shown in the Figure **4.2** allow to unambiguously identify fluorine sides in each molecule.

Concerning the growth of molecular networks on Si:B surface, many examples have been presented and studied extensively with STM techniques [85, 78, 65, 68]. One of these studies includes the work of Makoudi *et al.* [78], in which the assembly of 1,4 bis(4'cyanophenyl)-2,5bis(decyloxy)benzene molecule (CBD) on Si:B surface was investigated, using STM at 110 K. This molecule is one of two molecules studied in this thesis. It has been shown, that the deposition of molecules on a Si:B surface (at room temperature) resulted in formation of a periodic molecular network, with a simple crystallography and

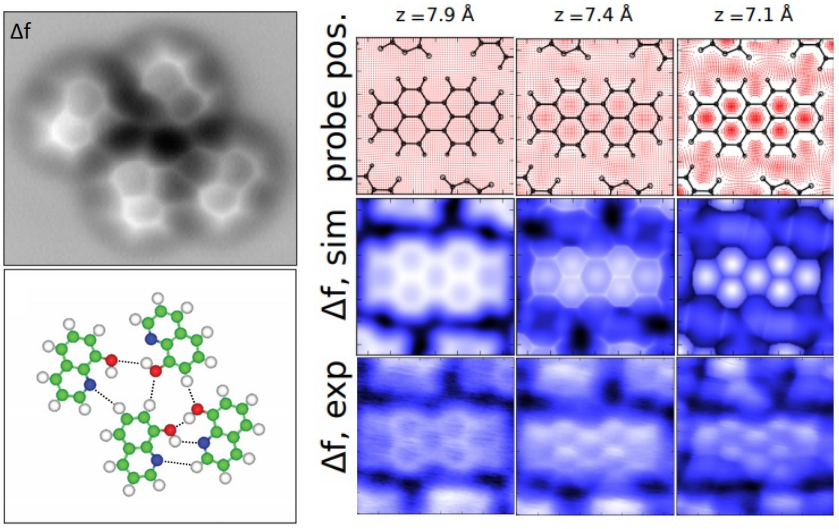

Figure 4.1: a) Δf image of 8-hq assembly on Cu(111) with CO functionalized tip, the bottom image shows a stucture model corresponding to AFM image. Extracted from [10] b) Experimental and simulated Δf images presenting contrast inversion and sharp edges in the intramolecular region for different tip-sample distances, in the upper panel the probe position after relaxation of tip apex is shown. Sharp features between the molecules start to appear for z=7.4 Å, adapted from [11].

regular distances of 2 nm between the molecular lines. The empty states STM image of the assembly is presented in Fig.**4.3(a)**. The network consists of bright lines made of the cores of the molecules and separated with darker stripes, corresponding to aliphatic chains of molecules in adjacent lines. Bright lines are made of pairs of bright protrusions where each one refers of one of cyano-phenyl groups of the molecule. The precise analysis of STM images permitted to propose the adsorption model of molecule on silicon surface and determination of interactions governing the assembly process. It has been observed, that the central phenyl is adsorbed between two silicon atoms and that the aliphatic chains are always placed between silicon rows. Therefore, both cyanophenyl groups of molecule are adsorbed above silicon adatoms, the core of the molecule forms an angle of 7° with Si lattice vector. This type of adsorption suggests predominance of molecule-surface (MS) over molecule-molecule (MM) forces. For the former, the main contribution is the van der Waals interaction of the aliphatic chains with silicon atoms of the substrate (green circle in the Fig. **4.3(b)**). For the MM interactions, the main contribution is π-π stacking between cyano-phenyl group of two subsequent molecules in the same nanoline (red circle in **4.3(b)**).

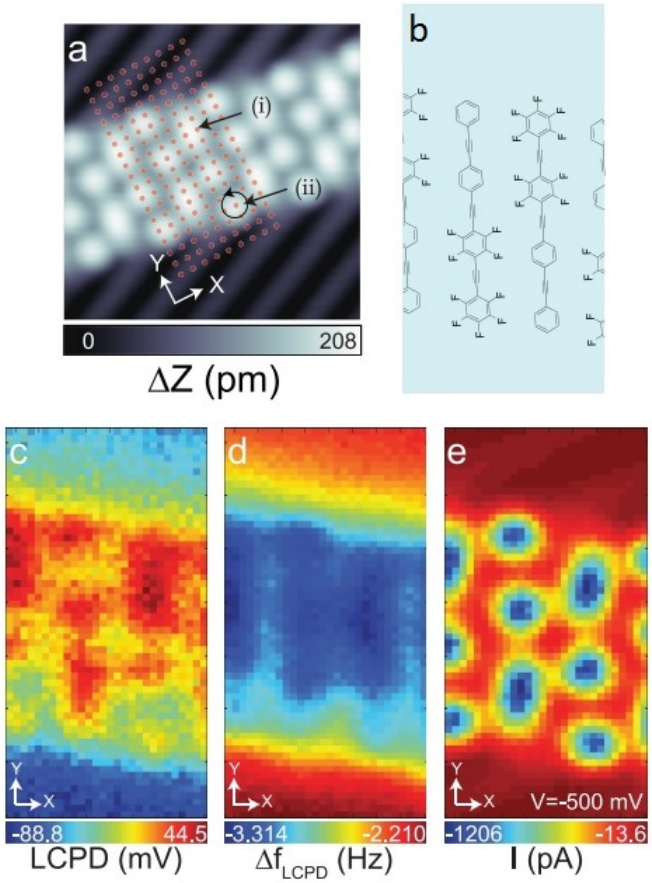

Figure 4.2: a) STM topography of FFPB assembly on Au(110) surface, b) structural model corresponding to KPFM images. LCPD and corresponding Δf_{LCPD} are shown in c), d), the tunnelling current map extracted from KPFM measurement for V=-500 mV is presented in e). Images adapted from [84].

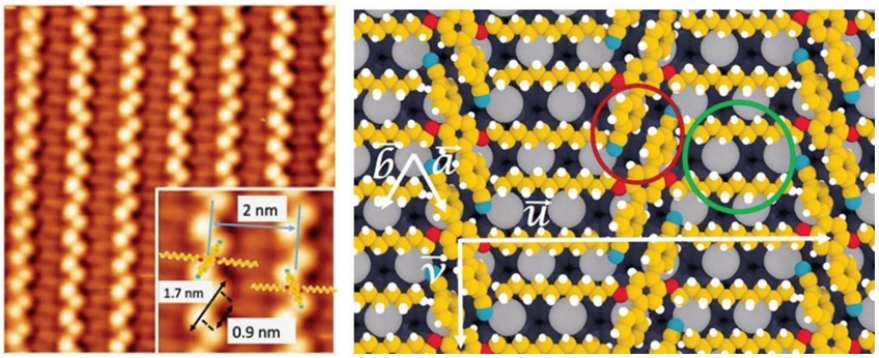

(a) (b)

Figure 4.3: a) STM image of CDB network on Si:B surface (V_{bias}=1.7 V, I_t=10 pA), in the inset molecules position with characteristic dimensions are indicated. b) Model of adsorption of molecule on Si:B surface, π-π stacking between molecules are indicated with red circle, chain interdigitation is indicated with green circle. Extracted from [78].

4.3 Organisation of CDB-I assemblies on the Si:B surface

Figure **4.4** presents STM images of the organisation of CDB-I molecule on the Si-B surface for RT depositions. Molecules were sublimated at 175°C during 2 min. After deposition, the organisation of large assemblies is seen, located close to silicon step edges. The molecules in domains form bright parallel lines. Three directions of molecular growth are found in the Figure **4.4(b)**, rotated by 120° relative to each other, due to the symmetry of Si-B surface. The changes in growth directions are often caused by the defects which are breaking the periodicity of the molecular network.

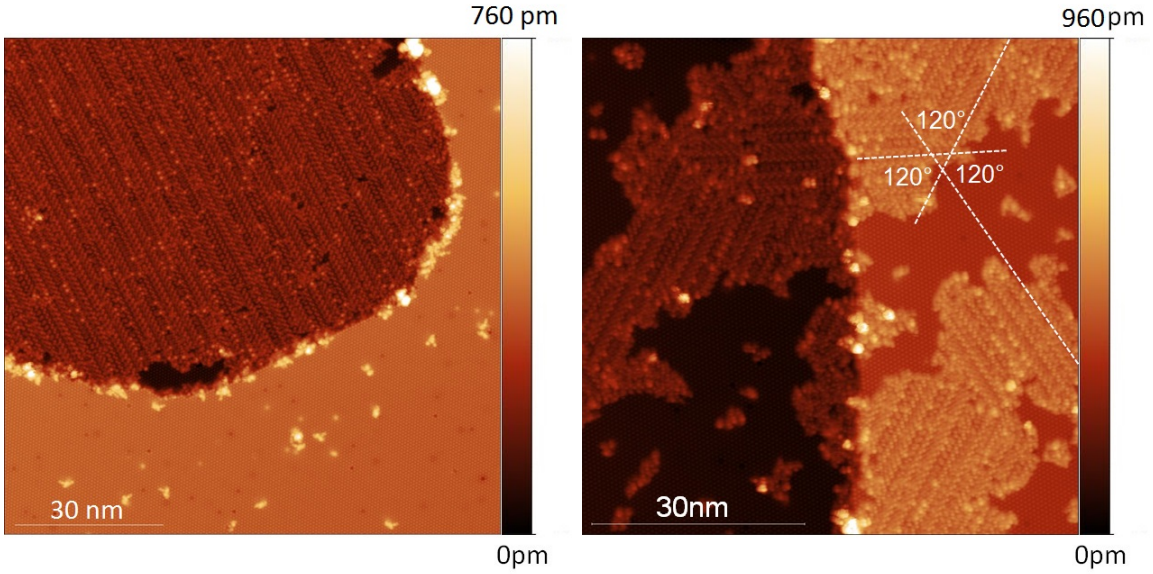

(a) (b)

Figure 4.4: STM images of the CDB-I molecule deposition effectuated on the sample kept at room temperature in UHV. In b), three directions of network growth are indicated with white intermittent lines, rotated by 120° to each other. Imaging parameters for both images : V_{bias}=2 V, I_t=5 pA.

4.3.1 Small domains of CDB-I

STM and AFM images showing the organisation of molecules in a small domain is presented in the Figure **4.5**. In the constant height AFM image the structure of each molecule is recognized. First of all, the aromatic cores with three phenyls are identified, where the central phenyl is oriented flat on the surface and two side phenyls are tilted. This corresponds to the contrast in the form of brighter parallel lines seen in the STM image. Besides, the inderdigitation of aliphatic chains is observed, between the molecules

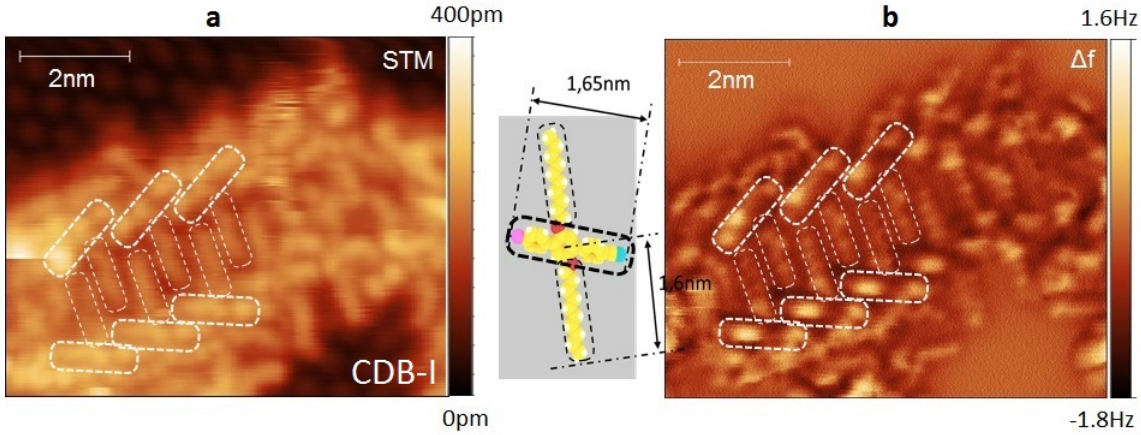

Figure 4.5: Comparison of a) STM (V_{bias}=-1.9 V, I_t=5 pA) and b) AFM contrast obtained on a small molecular domain of CDB-I. The structure of each molecule is identified and indicated with intermittent line.

in the adjacent lines. Interestingly, the part of aliphatic chains on the border of the domain is in disorder, as they do not have a neighbouring molecule to interact with. The orientation of molecules in the given row is in like manner, that is, the angle between the direction of the molecular line and the molecule core axis is constant.

4.3.2 Large assemblies of CDB-I

In order to find the organisation of molecules in the assemblies on a bigger scale, the edge of a large network was imaged (Figure **4.6**). On the first site, in the AFM image the alternance of aliphatic chains organisation is noticed. Part of chains are straight and well aligned, while the others are bent. In the STM image the presence of many bright spots is observed, located always only on one side of a given molecular row. These features correspond to small defects of the network, where the side phenyls appear slightly elongated and moved out of a surface plane. [1] In order to find the position of molecules with respect to the silicon substrate, a small bias was applied on the sample while AFM imaging. It permits the detection of the tunnelling current above the molecules but more importantly also on the silicon substrate, as shown in the Figure **4.7**. The contrast obtained on the silicon atoms can be then used to position molecules with respect to the substrate lattice. The silicon substrate lattice superimposed on the AFM image is shown in the Figure **4.7(c)**. From this analysis firstly we measure two different separations between the molecular lines of 2 nm and 2.35 nm (corresponding to the situation where

[1] Additionally, the high resolution in AFM is accompanied by the excitation signal measured on the well aligned chains. This can indicate that these molecules interact less with the silicon surface and therefore it is easier to dissipate the energy from them while scanning in the close proximity during constant height AFM.

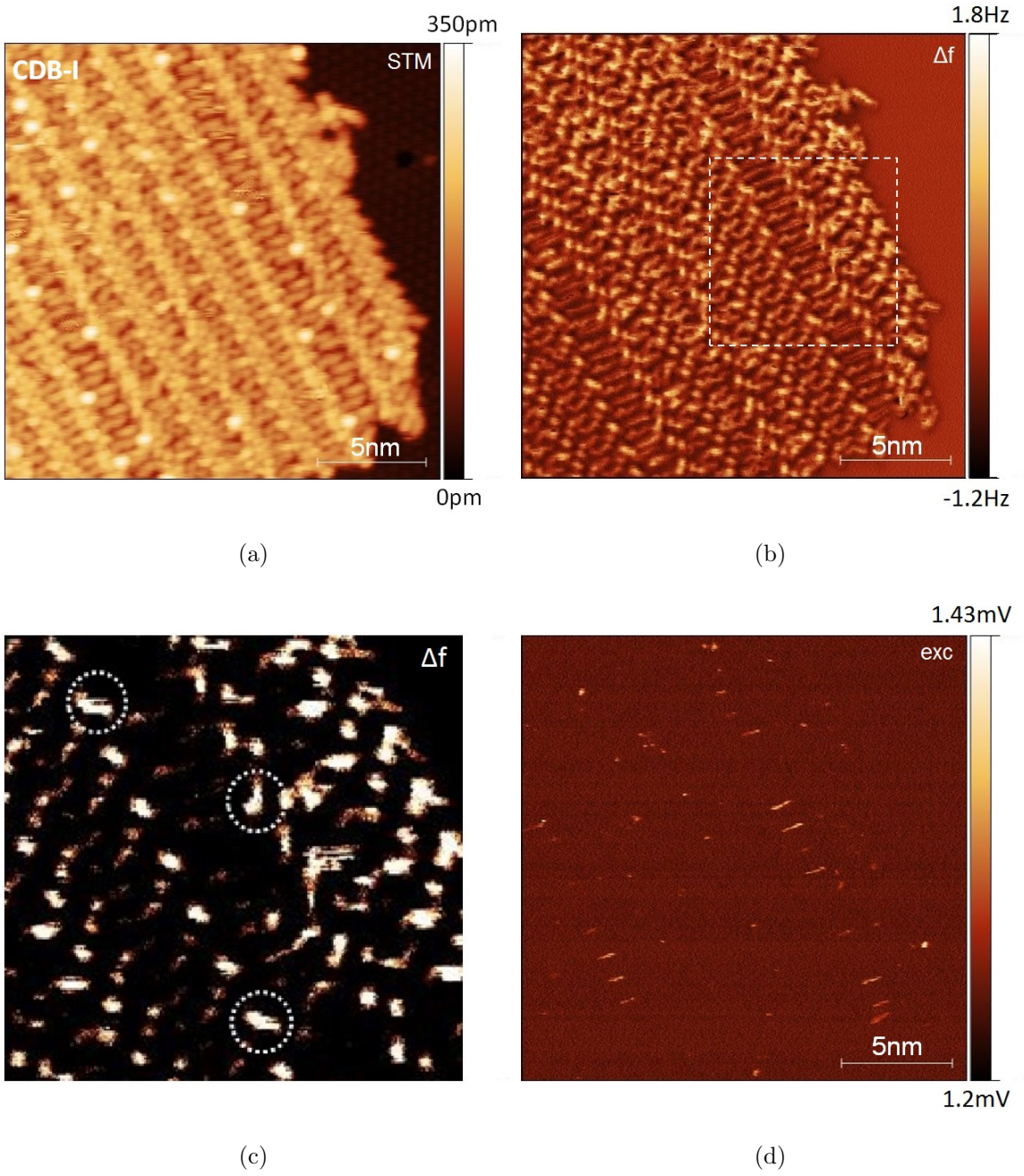

Figure 4.6: a) STM (V_{bias}=-1.8 V, I_t=5 pA) and b) AFM images of a large molecular assembly of CDB-I. c) Zoom of the AFM with sharpened contrast is presented in order to emphasize the defects of the network corresponding to bright spots observed in the STM image. The zone of the zoom is indicated in b) with white intermittent line. The excitation signal measured on the aliphatic chains is shown in d). AFM measurement was done with V_{bias}=0 V.

the aliphatic chains are bent or well aligned) which correspond to d_1 and d_2 respectively, as indicated in the Figure **4.7(c)**. Considering the orientation of molecules we observe that the central phenyl of each molecule is placed in the bridge position between two adjacent silicon atoms and the aliphatic chains are always located between silicon rows.

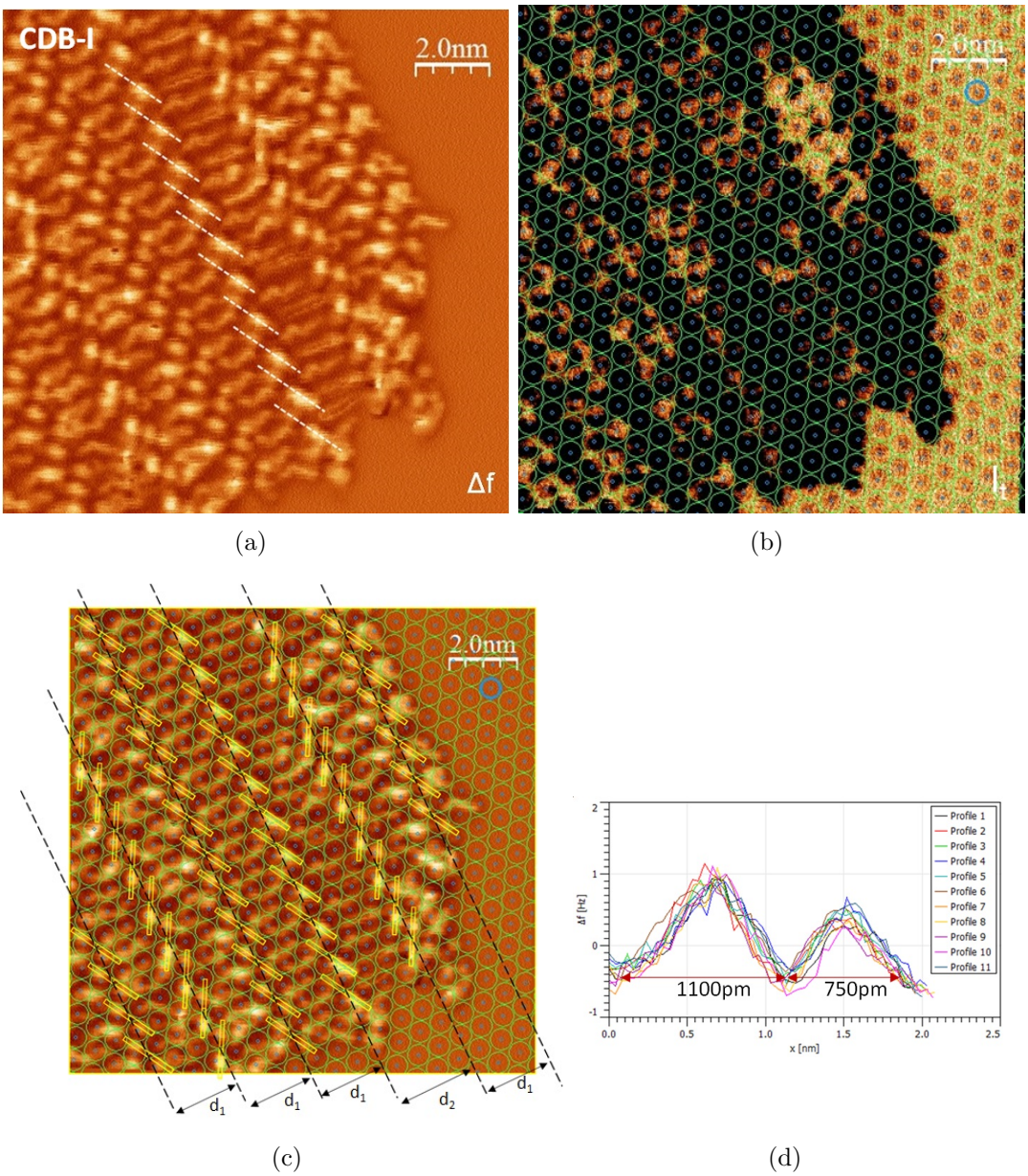

Figure 4.7: Zoom of the CDB-I network presented in the Figure **4.6**. a) Δf and b) I_t channel extracted from the measurement. The superposition of silicon lattice on the AFM image is shown in c), d) cross section profiles for each molecule showing an asymmetry between the length of two side phenyl groups of $\approx$ 350 pm. Two different separations between the assembly lines are indicated with d_1 and d_2, corresponding to 2 nm and 2.35 nm respectively.

This in turn indicates the important interaction between the molecules and the substrate. Moreover, it can be seen that the Δf contrast on the molecule is not only related to its position with respect to the surface but also to the topology of the molecule itself (as seen in the Figure **4.7(c)**). The cross section done through the molecules along a given line is presented in the Figure **4.7(d)**. Again, for CDB-I the asymmetry of length between two side-phenyl groups is found, similarly to the single molecule presented in the previous

chapter. The mean value of length difference measured for CDB-I is 350 pm ± 20 pm. What is important, all molecules in a given row show the same asymmetry that is, the longer terminations are all located on the one side of a molecular row.

4.4 Assemblies of CDB

To verify if the dipolar character of molecule has an effect on the assembly process, in this section the study of non-polar CDB molecule has also been investigated. The deposition was done in the same conditions of 175°C during 2 min on the sample held at room temperature. Figure **4.8** shows the STM and AFM images obtained for a CDB molecule assembly. Similarly to CDB-I molecule the difference in chain organisation is observed in the AFM image. The same analysis of positioning the molecules with respect to substrate atoms was done as presented in the Figure **4.8(c)**. The distances between the molecular lines are 2 nm and 2.35 nm, which are the same distances measured for CDB-I molecules. Moreover, the same positions of molecules with respect to the substrate were found, that is aliphatic chains are located always between silicon atoms rows and the central phenyl of molecules is placed between the atoms of silicon. From the cross section shown in **4.8(d)** no apparent asymmetry is observed but a small difference of 20 pm between two side phenyl groups, which falls within experimental accuracy.

From the comparison of cross sections through the cores of the molecules in Δf images for both CDB and CDB-I, the apparent asymmetry is observed only for CDB-I molecule. The discrimination between the different terminations cannot be yet carried out. The terminations length from the cross sections of CDB-I and CDB cannot be compared, as the absolute values depend on the tip convolution and imaging conditions, mostly the tip-sample distance, which were surely not the same in both measurements. Consequently, Δf imaging permits the observation of the molecule asymmetry but additional KPFM measurements must be performed in order to designate the different terminations of the molecule as in the case of single molecules.

4.5 KPFM on CDB-I and CDB assemblies

KPFM measurements on assemblies presented in this section have been done using the same experimental procedure as for Si:B surface defects, described in the section **2.3**. The grid experiment of small part of the CDB-I network is presented in the Figure **4.9**. For both grids the tip was retracted by 200 pm before the experiment and the oscillation amplitude was increased to 100 pm. Due to the fact, that grid points number was optimized to avoid a significant lateral drift, the resolution obtained on assemblies is much inferior

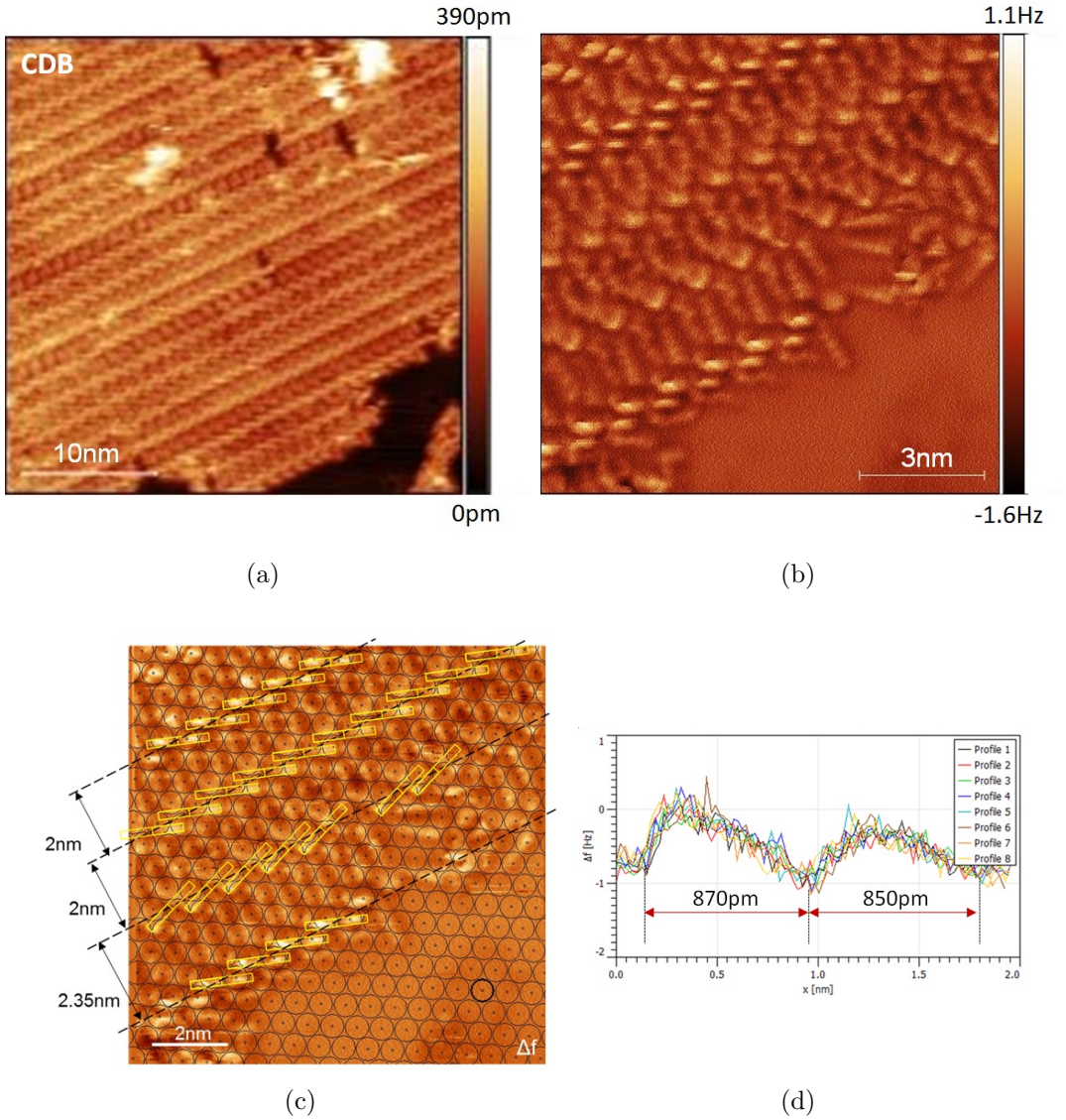

Figure 4.8: a) STM (V_{bias}=-1.8 V, I_t=3 pA) and b) Δf image of CDB molecular assembly. The superposition of silicon lattice on the AFM image is shown in c). Cross section profiles for each molecule indicated with intermittent line in the Δf image is presented in d).

than for single molecules presented in the section **3.4**. The lateral drift for both grids was ≈ 250 pm. In the $\Delta f(V_s)$ map of the first grid (shown in **4.9(b)**), a (dark) van der Waals signal is detected on molecules, especially on three-phenyl cores. In the surface potential map a higher signal is detected on molecule core than on aliphatic chains. Using $\Delta f(V_s)$ map it is possible to roughly position the terminations of each molecule of the molecular line. Therefore, the terminations located on the right side (indicated with yellow arrows) have higher V_s than the terminations on the left side of the row (blue arrows), as shown in **4.9(c)**. The second grid shown in **4.9(d)**) was done for the same molecular row but for two different molecules, in order to check the reproducibility of measurement. Again, the

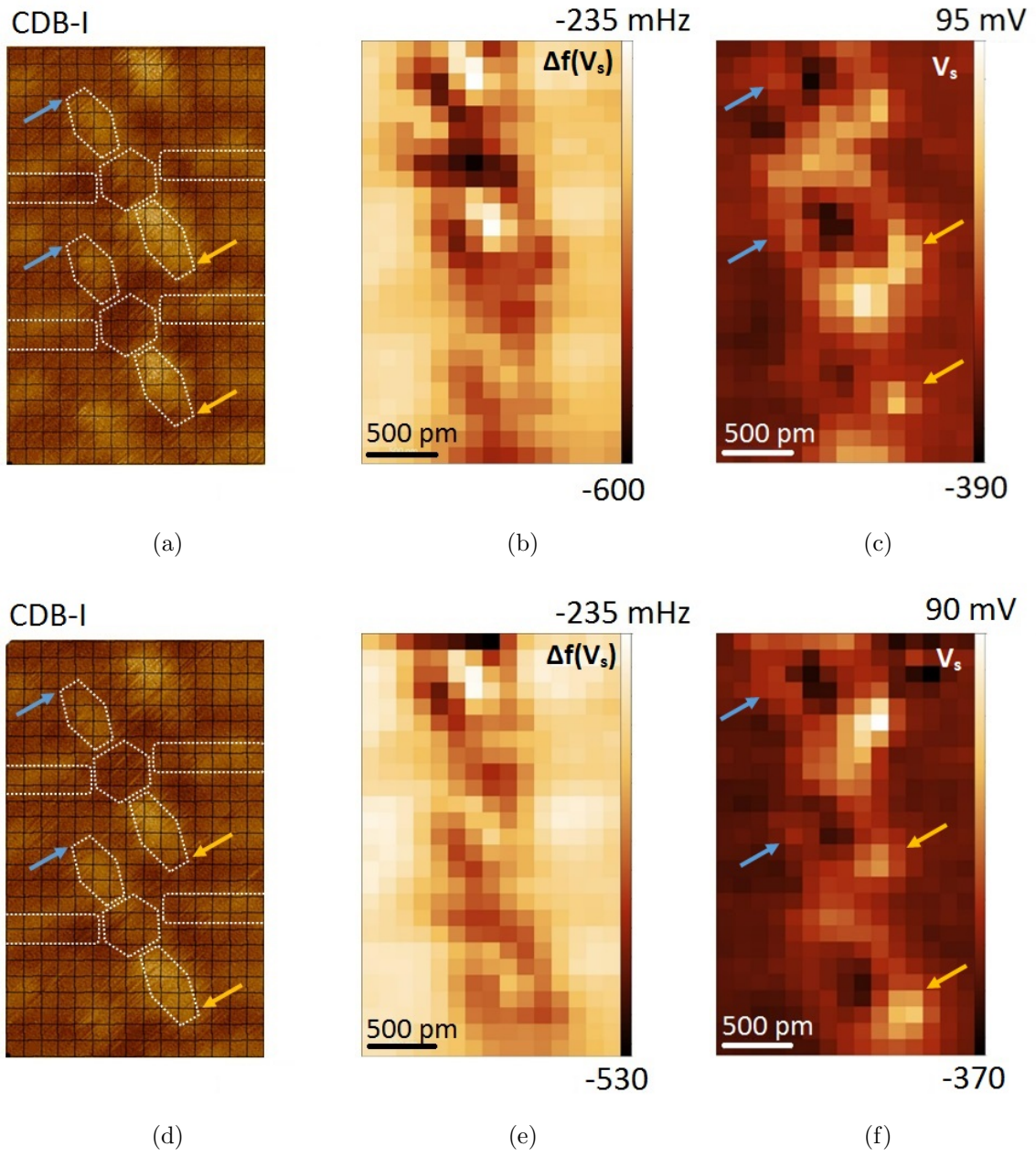

Figure 4.9: KPFM measurements for two grids done on the small part of the CDB-I molecular assembly. In b), c) $\Delta f(V_s)$ and surface potential maps are shown, corresponding to the grid in a), in e), f) $\Delta f(V_s)$ and surface potential maps of the second grid in d). Yellow and blue arrows indicate the terminations with high and small V_s of molecules, the duration of each grid was 3,5 h.

similar contrast is observed for both $\Delta f(V_s)$ and V_s maps. The surface potential maps were further analysed for both grids, as presented in the Figure **4.10**. From the V_s cross sections in **4.10(b)** and **4.10(b)** we measured a difference between both terminations in the 60-120 mV range and in the 70-150 mV range, respectively. The mean value of distances between the molecule extremities in both experiments was 1.6 nm. Similarly to the single CDB-I molecule (section **3.4**), the same type of same asymmetry in both Δf and

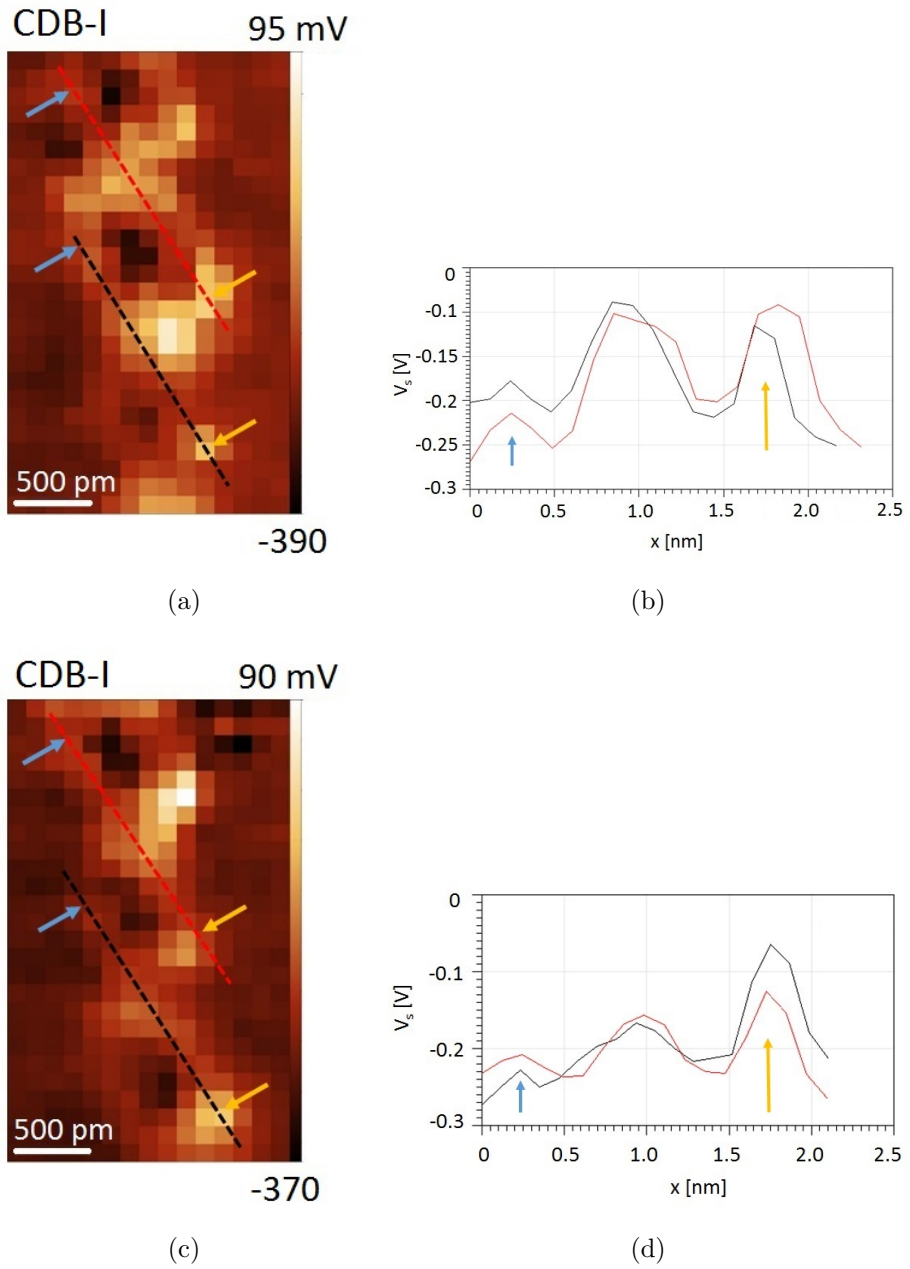

Figure 4.10: Surface potential maps of CDB-I molecules from the grids presented in the Figure **4.9**. In b), d) V_s maps with superimposed negative contrast from $\Delta f(V_s)$ for the grids in a), d) respectively. Cross section of V_s indicated with black and red intermittent lines in a), d) are shown in c), f).

V_s is observed. The longer terminations associated with cyano groups have more positive V_s signal, while the shorter terminations corresponding to iodine, have smaller V_s. The same asymmetry is observed for each molecule along a given molecular row which permits proposing a model where all the molecules organise themselves with parallel dipoles along a given row. That means that cyano groups of each molecule are located on the one side of the row and iodine terminations on the opposite side of the row.

A KPFM grid measurement of an assembly of CDB molecules is presented in the

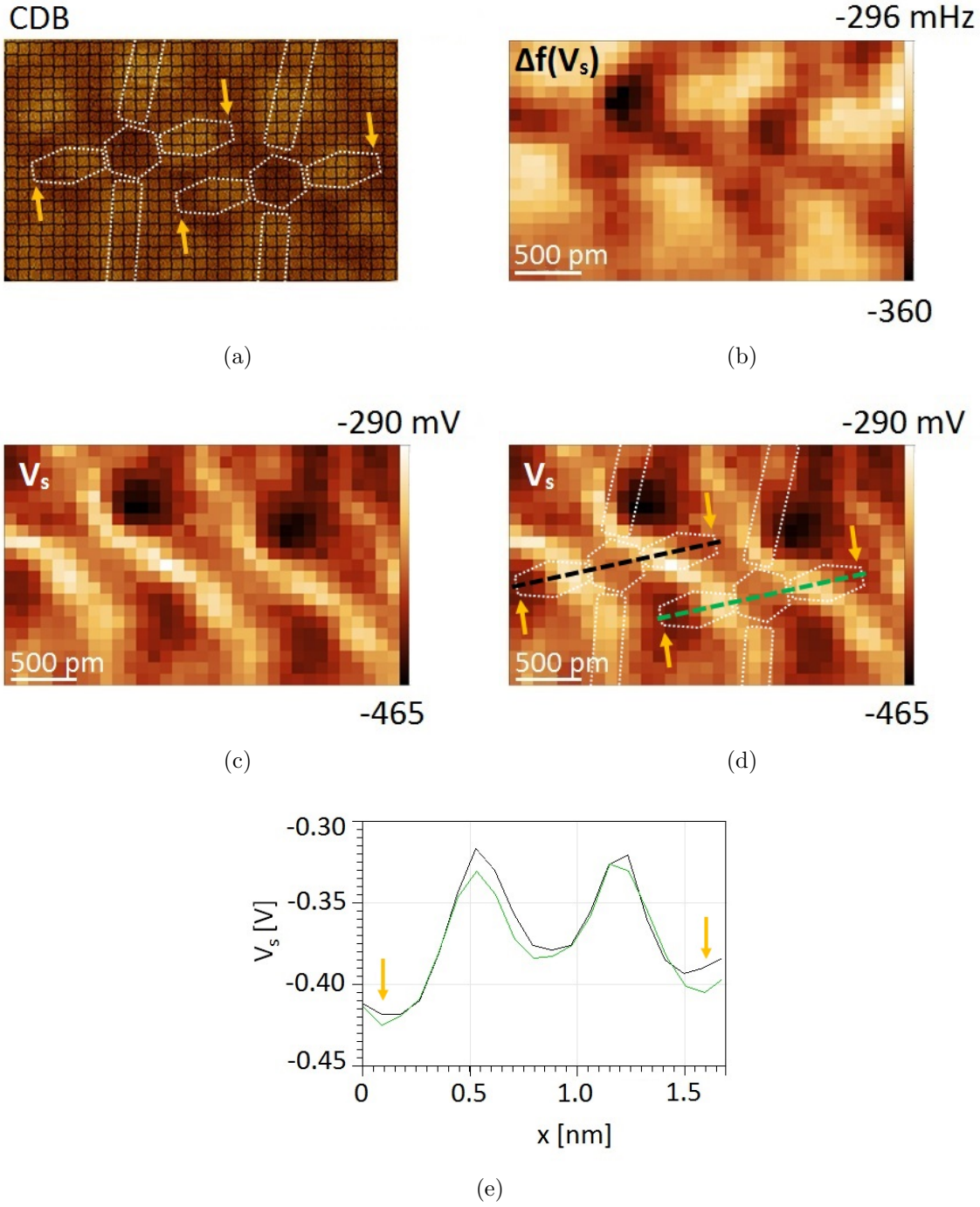

Figure 4.11: KPFM measurements for CDB molecular assembly, a) Δf image with grid before the measurement, b) $\Delta f(V_s)$, c) V_s and d) V_s with $\Delta f(V_s)$ dark contrast superimposed. Intermittent black and red lines in d) indicate the cross sections of V_s for both molecules presented in e). The duration of grid was 6h.

Figure **4.11**. The lateral drift of 400 pm was measured after the experiment. Similarly to the CDB-I molecule, the higher V_s contrast is measured above three-phenyl core but also on part of aliphatic chains. Superimposition of $\Delta f(V_s)$ contrast on surface potential

image is shown in **4.11(d)**. From the image, on the first sight it is seen that a high negative V_s signal is measured on the aliphatic chains of both molecules in the assembly and side phenyls are charged more negatively then the central phenyls. The cross sections realised through core of each molecule shown in **4.11(e)** are rather symmetric and present no significant difference in surface potential. The distance used to point out the two terminations is 1.5 nm.

4.6 Conclusions

A comparison of CDB and CDB-I molecule was done in this chapter using nc-AFM imaging and KPFM grid measurements. Starting from small domains, the identification of molecule structure was done with interdigitation of aliphatic chains between the molecules in adjacent lines. In large assemblies, the alternance of chain organisation observed for CDB-I does not come from the molecule dipole as the same behaviour is seen for non-polar CDB molecule. Regarding the molecule positions, for both CDB and CDB-I the central phenyls are located between two silicon atoms and aliphatic chains are placed between rows of silicon atoms. Therefore, it indicates that dominating interaction in the assembly process is van der Waals between the molecule and silicon substrate, as suggested previously in [78]. The only difference observed in Δf images is the asymmetry in the length of two side phenyl groups for polar CDB-I molecule. In the KPFM measurements, an additional asymmetry is seen between the molecules terminations in the surface potential map, only for CDB-I. For the longer terminations, associated previously in **3.4**, a higher V_s is measured, while for the shorter terminations, refereeing to iodine atoms, have smaller V_s. Due to the same character of the asymmetry for each molecule in the given line we propose an organisation model where the dipoles of molecules are parallel to each other in the each assembly row.

General conclusion and prospects

In this thesis, combined STM/nc-AFM with KPFM measurements have been performed on molecular assemblies deposited on the passivated surface of Si:B. All presented measurements have been carried out using a JT ST/AFM SPECS system with Kolibri sensor at the temperature of 4 K. In the subsequent part, the main objectives and obtained results are discussed.

First of all, the sensitivity in charge detection of the Kolibri sensor was verified via Δf(V) spectroscopy on the different defects of Si:B. In the KPFM measurements, different charge states were observed for the defects: neutral for silicon vacancy, negative for buried dopant and positive for silicon dangling bond. The charge states fall in accordance with previous STM studies [59, 60]. For the buried boron dopant the absolute value of the surface potential $\approx$ 35 mV is significantly smaller then for the dangling bond $\approx$ 85 mV due to the location of the dopant further under the surface plane. Moreover, the lateral extent of V_s of the dopant is greater than for a DB. For the dangling bond defect, non-parabolic behaviour of Δf(V) is observed due to the significant tunnelling current value at E$\approx$ 0.5 V, corresponding to the DB state located in the bandgap. In order to explain this phenomena, two mechanisms have been proposed: charge transfer of the electron from the tip to the DB and phantom force effect which results in additional Δf signal. The analysis spectroscopy curves leads to conclusion that both mechanisms can cause relatively similar behaviour of Δf and it is not possible to assign which of them dominates in the case of the dangling bond. Despite this, the negative surface potential indicates that for small sample bias DB is found in the positive charge state. The measured value V_s=-85 mV constitutes the reference of surface potential for a single charge located on the surface.

The second objective of this work was to study the molecular systems with submolecular resolution with nc-AFM and KPFM, without intentional tip functionalization. The results obtained for a single molecule have been presented in the Chapter **3**. The constant height frequency shift images presenting the structure of a single molecule correspond well to the model of the molecule in the vacuum (after minimization of the energy). The central phenyl is always orientated flat on the surface and two side phenyls are tilted and therefore much higher Δf signal is measured above them in the AFM images. The details

of aliphatic chains are observed as well, in the form of bright protrusions which correspond to five topmost carbon atoms of the chain, separated by 250 pm. Moreover, it was observed that the aliphatic chain position is not random but they are always located between the rows of silicon atoms. For CDB-I molecule, the asymmetry in length of two side phenyl groups was measured, stemming likely from the different molecule termination. Regarding KPFM measurements, the submolecular resolution has been also achieved in surface potential images of single molecules. Based on the images, two different types of molecule adsorption were distinguish for both CDB and CDB-I molecule. In the first type, the molecule with both positively and negatively charged submolecular features is observed, as in the situation without significant net charge transfer between the molecule and the substrate. More positive V_s is detected on the molecule core and lower on the aliphatic chains. The oxygen atoms are revealed in the surface potential maps as well, with very bright contrast corresponding to a negative charge. Furthermore, for CDB-I molecule the difference in contrast is seen between both terminations, with higher a V_s signal measured above the termination with greater length, possibly corresponding to cyano group. In the second type of adsorption, the KPFM contrast on the molecule is entirely negative. This type of contrast is proposed to stem from a molecule adsorbed on a dangling bond defect, and would correspond to a transfer of charge from the molecule to DB and positive charging of the molecule.

In the Chapter **4**, the organisation and orientation of CDB-I and CDB molecules was investigated in Δf images and KPFM measurements. For both molecules the structure is identified and the interdigitation of the aliphatic chains is observed between the molecules in the adjacent lines. Similarly to the single molecule, the aliphatic chains are always located between the silicon atoms, therefore the van der Waals interaction with the substrate is assumed to be the most important one in the assembly process. For both CDB-I and CDB the orientation of molecules in the assemblies and the distances between molecular lines are the same. In the KPFM measurements, the difference in the surface potential is measured between both terminations of CDB-I molecule, which is not seen in the case of polar CDB molecule. The asymmetry of the nc-AFM topography and KPFM map of CDB-I molecules indicates the dipolar organization along a given assembly row.

The measurements presented in the Chapters **3** and **4** showed promising results and the high resolution obtained in nc-AFM and KPFM images obtained without intentional tip functionalization on molecular assemblies. In the frequency shift images the structure of molecules were identified but could be still improved by functionalizing the tip apex with single molecule. There are no studies published so far concerning the procedure of collecting CO (or any other molecule) from the semiconductor surface. Moreover, the adsorption and the STM contrast of CO deposited on the silicon surface is not known. The

alternative method would be collection CO from the metal surface and then approaching the tip on the target silicon sample with already functionalized tip. It has been shown by Giessibl (conference talk, 19th International Conference on NC-AFM, 2017) that this method brought the satisfactory results if the microscope temperature does not increase significantly (above 30 K) during changing the samples. The tip functionalization is not only advantageous in enhanced resolution in nc-AFM and KPFM images but would also permit the quantitative analysis of obtained results in link with simulations where the tip apex can be a priori known.

Annexes

Publications:

- **"Doped Colloidal InAs Nanocrystals in the Single Ionized Dopant Limit"** Moussa Biaye, Yorai Amit, Kamil Gradkowski, Natalia Turek, Sylvie Godey, Younes Makoudi, Dominique Deresmes, Athmane Tadjine, Christophe Delerue, Uri Banin, Thierry Mélin, *J. Phys. Chem. C*, 123(23), 2019
- **"Charge detection of Si(111)-($\sqrt{3} \times \sqrt{3}$)R°30-B defects"** Natalia Turek et al. *in preparation*
- **"High resolution imaging of molecular assemblies on a semiconductor surface by nc-AFM and KPFM"** Natalia Turek et al. *in preparation*

Conferences and workshops:

- 2nd German-French summer school on non-contact atomic force microscopy, Osnabruck, GERMANY, *September 2016*
- Le Forum des Microscopies à Sonde Locale, Montpellier, FRANCE, *April 2017*, poster **"Charge Transfers Induced By Doped InAs Colloidal Nanocrystals on Highly Oriented Pyrolytic Graphite"** Moussa Biaye, **Natalia Turek**, Sylvie Godey, Kamil Gradkowski, Yorai Amit, Younes Makoudi, Domonique Deresmes, Heinrich Diesinger, Uri Banin and Thierry Mélin
- Le Forum des Microscopies à Sonde Locale, La Rochelle, FRANCE, *April 2018*, oral presentation **"High resolution imaging of molecular assemblies on a semiconductor surface by non-contact AFM at low temperature" Natalia Turek**, Sylvie Godey, Dominique Deresmes, Thierry Mélin, Judicael Jeannoutot , Younes Makoudi, Frank Palmino , Frédéric Cherioux
- The 21st International Conference on Non-contact Atomic Force Microscopy, Porvoo, FINLAND, *October 2018*, oral presentation **"High resolution imaging of**

molecular assemblies on a semiconductor surface by non-contact AFM at low temperature" Natalia Turek, Judicaël Jeannoutot, Younes Makoudi, Frank Palmino, Frédéric Cherioux, Dominique Deresmes, Sylvie Godey, Thierry Mélin

- Troisième congrès national Sciences et Technologies des systèmes pi-conjugués (SPIC), Arras, FRANCE, *October 2019*, oral presentation **"High resolution imaging of molecular assemblies on Si(111):B by non-contact AFM and Kelvin probe spectroscopy at low temperature"** Natalia Turek, Dominique Deresmes, Judicaël Janneoutot, Younes Makoudi, Frank Palmino, Frédéric Chérioux, Sylvie Godey, **Thierry Mélin**

Bibliography

[1] Donald M Eigler and Erhard K Schweizer. "Positioning single atoms with a scanning tunnelling microscope". In: *Nature* 344.6266 (1990), p. 524.

[2] Noriaki Oyabu et al. "Mechanical vertical manipulation of selected single atoms by soft nanoindentation using near contact atomic force microscopy". In: *Physical Review Letters* 90.17 (2003), p. 176102.

[3] HQ Shi, MW Radny, and PV Smith. "Electronic structure of the Si (111) ($\sqrt{3} \times \sqrt{3}$)$R°$30- B surface". In: *Physical Review B* 66.8 (2002), p. 085329.

[4] Dimas G de Oteyza et al. "Direct imaging of covalent bond structure in single-molecule chemical reactions". In: *Science* 340.6139 (2013), pp. 1434–1437.

[5] Alexander Riss et al. "Imaging single-molecule reaction intermediates stabilized by surface dissipation and entropy". In: *Nature chemistry* 8.7 (2016), p. 678.

[6] Gerd Binnig et al. "Surface studies by scanning tunneling microscopy". In: *Physical review letters* 49.1 (1982), p. 57.

[7] Gerd Binnig, Calvin F Quate, and Ch Gerber. "Atomic force microscope". In: *Physical review letters* 56.9 (1986), p. 930.

[8] Franz J Giessibl. "Atomic resolution of the silicon (111)-(7x7) surface by atomic force microscopy". In: *Science* 267.5194 (1995), pp. 68–71.

[9] Leo Gross et al. "The chemical structure of a molecule resolved by atomic force microscopy". In: *Science* 325.5944 (2009), pp. 1110–1114.

[10] Jun Zhang et al. "Real-space identification of intermolecular bonding with atomic force microscopy". In: *Science* 342.6158 (2013), pp. 611–614.

[11] Prokop Hapala et al. "Mechanism of high-resolution STM/AFM imaging with functionalized tips". In: *Physical Review B* 90.8 (2014), p. 085421.

[12] Harry Mönig et al. "Quantitative assessment of intermolecular interactions by atomic force microscopy imaging using copper oxide tips". In: *Nature nanotechnology* 13.5 (2018), p. 371.

[13] Leo Gross et al. “Measuring the charge state of an adatom with noncontact atomic force microscopy”. In: *Science* 324.5933 (2009), pp. 1428–1431.

[14] Prokop Hapala et al. “Mapping the electrostatic force field of single molecules from high-resolution scanning probe images”. In: *Nature communications* 7 (2016), p. 11560.

[15] Fabian Mohn et al. “Different tips for high-resolution atomic force microscopy and scanning tunneling microscopy of single molecules”. In: *Applied Physics Letters* 102.7 (2013), p. 073109.

[16] Georgy Kichin et al. “Single molecule and single atom sensors for atomic resolution imaging of chemically complex surfaces”. In: *Journal of the American Chemical Society* 133.42 (2011), pp. 16847–16851. ISSN: 00027863. DOI: 10.1021/ja204624g.

[17] Harry Mönig et al. “Submolecular imaging by noncontact atomic force microscopy with an oxygen atom rigidly connected to a metallic probe”. In: *ACS nano* 10.1 (2015), pp. 1201–1209.

[18] Taras Chutora et al. “Nitrous oxide as an effective AFM tip functionalization: a comparative study”. In: *Beilstein journal of nanotechnology* 10.1 (2019), pp. 315–321.

[19] Adam Sweetman et al. “Intramolecular bonds resolved on a semiconductor surface”. In: *Physical Review B* 90.16 (2014), p. 165425.

[20] Jan Berger et al. “Force-Driven Single-Atom Manipulation on a Low-Reactive Si Surface for Tip Sharpening”. In: *Small* 11.30 (2015), pp. 3686–3693.

[21] W Steurer et al. “Manipulation of the charge state of single Au atoms on insulating multilayer films”. In: *Physical review letters* 114.3 (2015), p. 036801.

[22] Fabian Mohn et al. “Imaging the charge distribution within a single molecule”. In: *Nature nanotechnology* 7.4 (2012), p. 227.

[23] TR Albrecht et al. “Frequency modulation detection using high-Q cantilevers for enhanced force microscope sensitivity”. In: *Journal of Applied Physics* 69.2 (1991), pp. 668–673.

[24] Seizo Morita et al. *Noncontact atomic force microscopy*. Vol. 3. Springer, 2015.

[25] Ricardo Garcıa and Ruben Perez. “Dynamic atomic force microscopy methods”. In: *Surface science reports* 47.6-8 (2002), pp. 197–301.

[26] U Dürig. “Extracting interaction forces and complementary observables in dynamic probe microscopy”. In: *Applied Physics Letters* 76.9 (2000), pp. 1203–1205.

[27] Franz J Giessibl. "Forces and frequency shifts in atomic-resolution dynamic-force microscopy". In: *Physical Review B* 56.24 (1997), p. 16010.

[28] B Gotsmann et al. "Conservative and dissipative tip-sample interaction forces probed with dynamic AFM". In: *Physical Review B* 60.15 (1999), p. 11051.

[29] Franz J Giessibl. "Advances in atomic force microscopy". In: *Reviews of modern physics* 75.3 (2003), p. 949.

[30] Jeffrey L Hutter and John Bechhoefer. "Calibration of atomic-force microscope tips". In: *Review of Scientific Instruments* 64.7 (1993), pp. 1868–1873.

[31] Stefan Torbrügge, Oliver Schaff, and Jörg Rychen. "Application of the KolibriSensor® to combined atomic-resolution scanning tunneling microscopy and noncontact atomic-force microscopy imaging". In: *Journal of Vacuum Science & Technology B, Nanotechnology and Microelectronics: Materials, Processing, Measurement, and Phenomena* 28.3 (2010), C4E12–C4E20.

[32] Sonia Matencio Lloberas. "An STM/FM-AFM investigation of selected organic and inorganic 2D systems on metallic surfaces". In: (2015).

[33] Clemens Barth et al. "Recent trends in surface characterization and chemistry with high-resolution scanning force methods". In: *Advanced materials* 23.4 (2011), pp. 477–501.

[34] Shinichi Kitamura and Masashi Iwatsuki. "High-resolution imaging of contact potential difference with ultrahigh vacuum noncontact atomic force microscope". In: *Applied Physics Letters* 72.24 (1998), pp. 3154–3156.

[35] Shinichi Kitamura, Katsuyuki Suzuki, and Masashi Iwatsuki. "High resolution imaging of contact potential difference using a novel ultrahigh vacuum non-contact atomic force microscope technique". In: *Applied surface science* 140.3-4 (1999), pp. 265–270.

[36] Sascha Sadewasser and Thilo Glatzel. *Kelvin probe force microscopy*. Vol. 48. Springer, 2012.

[37] Kenji Okamoto et al. "KPFM imaging of Si(111) 53× 53-Sb surface for atom distinction using NC-AFM". In: *Applied surface science* 210.1-2 (2003), pp. 128–133.

[38] Shinichi Kitamura et al. "Atomic-scale variations in contact potential difference on Au/Si (111) 7× 7 surface in ultrahigh vacuum". In: *Applied surface science* 157.4 (2000), pp. 222–227.

[39] K Wandelt. "The local work function: Concept and implications". In: *Applied Surface Science* 111 (1997), pp. 1–10.

[40] Franck Bocquet et al. "Analytical approach to the local contact potential difference on (001) ionic surfaces: implications for Kelvin probe force microscopy". In: *Physical Review B* 78.3 (2008), p. 035410.

[41] Laurent Nony et al. "Understanding the atomic-scale contrast in Kelvin probe force microscopy". In: *Physical review letters* 103.3 (2009), p. 036802.

[42] Franck Bocquet, Laurent Nony, and Christian Loppacher. "Polarization effects in noncontact atomic force microscopy: A key to model the tip-sample interaction above charged adatoms". In: *Physical Review B* 83.3 (2011), p. 035411.

[43] V Adrian Parsegian. *Van der Waals forces: a handbook for biologists, chemists, engineers, and physicists*. Cambridge University Press, 2005.

[44] Jacob N Israelachvili. *Intermolecular and surface forces*. Academic press, 2011.

[45] Ernst Meyer, Hans Josef Hug, and Roland Bennewitz. *Scanning probe microscopy: the lab on a tip*. Springer Science & Business Media, 2013.

[46] Jun Zhang et al. "Real-space identification of intermolecular bonding with atomic force microscopy". In: *Science* 342.6158 (2013), pp. 611–614.

[47] Yoshiaki Sugimoto et al. "Atom inlays performed at room temperature using atomic force microscopy". In: *Nature materials* 4.2 (2005), p. 156.

[48] Nadine Hauptmann et al. "Force and conductance during contact formation to a C60 molecule". In: *New Journal of Physics* 14.7 (2012), p. 073032.

[49] Sarah A Burke. *Building foundations for molecular electronics: growth of organic molecules on alkali halides as prototypical insulating substrates*. 2009.

[50] Seizo Morita, Roland Wiesendanger, and Ernst Meyer. *Noncontact Atomic Force Microscopy*. Vol. 1. Springer, 2002.

[51] Franz J Giessibl et al. "Comparison of force sensors for atomic force microscopy based on quartz tuning forks and length-extensional resonators". In: *Physical Review B* 84.12 (2011), p. 125409.

[52] Florian Pielmeier et al. "Impact of thermal frequency drift on highest precision force microscopy using quartz-based force sensors at low temperatures". In: *Beilstein journal of nanotechnology* 5.1 (2014), pp. 407–412.

[53] Ben G Streetman, Sanjay Banerjee, et al. *Solid state electronic devices*. Vol. 4. Prentice hall Englewood Cliffs, NJ, 1995.

[54] Daejin Eom, Chang-Youn Moon, and Ja-Yong Koo. "Switching the charge state of individual surface atoms at Si (111)-$\sqrt{3}$ x $\sqrt{3}$:B surfaces". In: *Nano letters* 15.1 (2015), pp. 398–402.

[55] T Mélin et al. "Probing nanoscale dipole-dipole interactions by electric force microscopy". In: *Physical review letters* 92.16 (2004), p. 166101.

[56] Laurent Nony et al. "On the relevance of the atomic-scale contact potential difference by amplitude-modulation and frequency-modulation Kelvin probe force microscopy". In: *Nanotechnology* 20.26 (2009), p. 264014.

[57] Ali Sadeghi et al. "Multiscale approach for simulations of Kelvin probe force microscopy with atomic resolution". In: *Physical Review B* 86.7 (2012), p. 075407.

[58] Hans-Joachim Güntherodt and Roland Wiesendanger. *Scanning tunneling microscopy I: general principles and applications to clean and adsorbate-covered surfaces*. Springer, 1992.

[59] M Berthe et al. "Electron transport via local polarons at interface atoms". In: *Physical review letters* 97.20 (2006), p. 206801.

[60] M Berthe et al. "Probing the carrier capture rate of a single quantum level". In: *Science* 319.5862 (2008), pp. 436–438.

[61] TH Nguyen et al. "Coulomb energy determination of a single Si dangling bond". In: *Physical review letters* 105.22 (2010), p. 226404.

[62] EJ Spadafora et al. "Identification of Surface Defects and Subsurface Dopants in a Delta-Doped System Using Simultaneous nc-AFM/STM and DFT". In: *The Journal of Physical Chemistry C* 118.29 (2014), pp. 15744–15753.

[63] Alfred J Weymouth et al. "Phantom force induced by tunneling current: a characterization on Si (111)". In: *Physical review letters* 106.22 (2011), p. 226801.

[64] Thorsten Wutscher, Alfred J Weymouth, and Franz J Giessibl. "Localization of the phantom force induced by the tunneling current". In: *Physical Review B* 85.19 (2012), p. 195426.

[65] Bulent Baris et al. "Noncovalent bicomponent self-assemblies on a silicon surface". In: *ACS nano* 6.8 (2012), pp. 6905–6911.

[66] Guillaume Copie et al. "Surface-induced optimal packing of two-dimensional molecular networks". In: *Physical review letters* 114.6 (2015), p. 066101.

[67] Younes Makoudi et al. "Complete supramolecular self-assembled adlayer on a silicon surface at room temperature". In: *Journal of the American Chemical Society* 130.21 (2008), pp. 6670–6671.

[68] Younes Makoudi et al. "Supramolecular self-assembly on the B-Si (111)-($\sqrt{3}$ x $\sqrt{3}$) R30° surface: From single molecules to multicomponent networks". In: *Surface Science Reports* 72.4 (2017), pp. 316–349.

[69] Maxime Berthe. "Electronic transport in quantum confined systems". PhD thesis. Université des Sciences et Technologie de Lille-Lille I, 2007.

[70] Saleem Ayaz Khan et al. "Local geometry around B atoms in B/Si(111) from polarized x-ray absorption spectroscopy". In: 111 (2019), pp. 7–11. eprint: 1902.06244. URL: http://arxiv.org/abs/1902.06244.

[71] Fabian Mohn. "Probing electronic and structural properties of single molecules on the atomic scale". PhD thesis. 2012.

[72] Thibault Ardhuin et al. "Measurement and Control of the Charge Occupation of Single Adsorbed Molecules Levels by STM and Nc-AFM". In: *The Journal of Physical Chemistry C* (2019).

[73] Laurent Nony et al. "Frequency shift, damping, and tunneling current coupling with quartz tuning forks in noncontact atomic force microscopy". In: *Physical Review B* 94.11 (2016), p. 115421.

[74] Leo Gross et al. "Organic structure determination using atomic-resolution scanning probe microscopy". In: *Nature chemistry* 2.10 (2010), p. 821.

[75] Niko Pavliček et al. "On-surface generation and imaging of arynes by atomic force microscopy". In: *Nature chemistry* 7.8 (2015), p. 623.

[76] Bruno Schuler et al. "Unraveling the molecular structures of asphaltenes by atomic force microscopy". In: *Journal of the American Chemical Society* 137.31 (2015), pp. 9870–9876.

[77] Bruno Schuler et al. "Adsorption geometry determination of single molecules by atomic force microscopy". In: *Physical review letters* 111.10 (2013), p. 106103.

[78] Younes Makoudi et al. "Towards 1D nanolines on a monolayered supramolecular network adsorbed on a silicon surface". In: *Nanoscale* 8.24 (2016), pp. 12347–12351.

[79] Matthieu Beyer. "Elaborations et caractérisations d'auto-assemblages dipolaires par microscopie à effet tunnel". PhD thesis. 2015.

[80] Ania Amrous et al. "Molecular Design and Control Over the Morphology of Self-Assembled Films on Ionic Substrates". In: *Advanced Materials Interfaces* 1.9 (2014), p. 1400414.

[81] Julian Gaberle et al. "Morphology and Growth Mechanisms of Self-Assembled Films on Insulating Substrates: Role of Molecular Flexibility and Entropy". In: *The Journal of Physical Chemistry C* 121.8 (2017), pp. 4393–4403.

[82] Christian Weiss et al. "Direct imaging of intermolecular bonds in scanning tunneling microscopy". In: *Journal of the American Chemical Society* 132.34 (2010), pp. 11864–11865.

[83] AM Sweetman et al. "Mapping the force field of a hydrogen-bonded assembly". In: *Nature communications* 5 (2014), p. 3931.

[84] Shigeki Kawai et al. "Obtaining detailed structural information about supramolecular systems on surfaces by combining high-resolution force microscopy with ab initio calculations". In: *ACS nano* 7.10 (2013), pp. 9098–9105.

[85] Younes Makoudi et al. "Tailored molecular design for supramolecular network engineering on a silicon surface". In: *ChemPhysChem* 14.5 (2013), pp. 900–904.